

# **Thermomechanical processing optimization of Rene 65 turbine engine components via heat treatment experimental design**

Christina-Maria Katsari

Department of Mining and Materials Engineering

McGill University, Montreal

May 2021



A thesis submitted to McGill University in partial fulfillment of the requirements of the degree  
of Doctor of Philosophy

©Christina – Maria Katsari, 2021

## ABSTRACT

Cast and wrought Ni-based superalloy Rene 65 has been developed for turbine engine components applications, such as disks and blades. The microstructure in the as-forged condition of the superalloy consists of ~40% volume fraction of gamma prime ( $\gamma'$ ) precipitates, which give such a high strength that thermomechanical processing of these components can be challenging. The microstructure consists of a bimodal/trimodal  $\gamma'$  precipitate distribution on the grain boundaries and intergranularly, ranging from  $\mu\text{m}$  (primary  $\gamma'$ ) to nm (secondary and tertiary  $\gamma'$ ). To control grain size, relatively coarse primary  $\gamma'$  should be present on the grain boundaries since they have a pinning effect and, to reduce hardness, the secondary and tertiary precipitate volume fraction should be as small as possible and their size should be relatively coarse. Therefore, to improve the processability of this alloy, a softening heat treatment schedule for manufacturing must be developed based on these precipitate characteristics.

The first step in understanding the precipitate characteristics in this alloy, which has not been extensively characterized in the literature due to its recent development, is a detailed microstructural and chemical characterization of the precipitates. Scanning and Transmission Electron Microscopy (SEM and TEM) as well as Atom Probe Tomography (APT) are employed to identify the differences in morphology and chemical compositions, respectively. The samples are characterized before and after a softening sub-solvus heat treatment. In the as received condition, differences in Cr, Ti and Al content are found between the three precipitate sizes. After the softening heat treatment, the intensity of the chemical composition differences (mainly in Ti and Al) at the interface between secondary  $\gamma'$  with the matrix has decreased. The lattice mismatch of secondary and tertiary  $\gamma'$  is empirically calculated based on the APT compositions. After this thorough analysis of the precipitate characteristics, a heat treatment schedule where hold time is

varied at a fixed temperature is applied on extruded samples. The microstructural analysis shows differences in the volume fraction and morphology of each precipitate type. Their hardness is also measured and reported.

“Experimental Design” is then used as a tool to optimize the proposed schedule, by varying not only hold time but also other three factors: cooling rate, hold temperature and cooling method to room temperature. The first design is based on Taguchi’s L8 matrix. There are two levels of the factors (high and low level) with replication. Microstructures are characterized by SEM and Vickers microhardness testing is applied to evaluate the effect of each heat treatment. Regression analysis showed that hold temperature was the most significant factor affecting hardness. The softest sample and the hardest sample have different microstructures, and the difference in strength is attributed to the trimodal distribution of precipitates in the latter.

The second experimental design that is chosen is based on the Central Composite Design, which is a Response Surface Method. Two sample conditions are examined, one deformed and one deformed and annealed, to verify if the softening heat treatment can be applied at different thermomechanical processing steps. The results confirm that the thermomechanical history is important, as the hardness of each condition is reduced by a different heat treatment. Precipitate splitting, and coralloid microstructures are observed for the first time in this alloy. Two mechanisms are proposed for hardness reduction based on the initial microstructure.

## RÉSUMÉ

Le superalliage à base de Ni coulé et corroyé Rene 65 a été développé pour les applications de composants de turbomoteurs, tels que les disques et les aubes. La microstructure à l'état forgé du superalliage consiste en une fraction volumique d'environ 40% de précipités gamma prime ( $\gamma'$ ), qui donnent une résistance si élevée que le traitement thermomécanique de ces composants peut être difficile. La microstructure consiste en une distribution bimodale / trimodale des précipités  $\gamma'$  aux joints de grains et intergranulaires, allant de  $\mu\text{m}$  ( $\gamma'$  primaire) au nm ( $\gamma'$  secondaire et tertiaire). Afin de contrôler la taille des grains, des  $\gamma'$  primaires relativement grossiers doivent être présents sur les joints de grains et, pour réduire la dureté, les précipités secondaires et tertiaires doivent être aussi petits que possible et leur taille relativement grossière. Par conséquent, afin d'améliorer l'aptitude au traitement de cet alliage, un programme de traitement thermique d'adoucissement pour la fabrication doit être développé en visant ces caractéristiques de précipité.

La première étape pour comprendre les caractéristiques des précipité, est une caractérisation microstructurale et chimique détaillée des précipités. La microscopie électronique à balayage et à transmission (MEB et MET) ainsi que la tomographie par sonde atomique (SAT) sont utilisées pour identifier les différences de morphologie et de compositions chimiques, respectivement. Les échantillons sont caractérisés avant et après un traitement thermique sous - solvus adoucissant. Dans l'état tel que reçu, des différences de teneur en Cr, Ti et Al sont trouvées entre les trois tailles de précipité. Après la traitement thermique, l'intensité des différences de composition chimique (principalement en Ti et Al) à l'interface entre  $\gamma'$  secondaire avec la matrice a diminué. La cohérence de réseau de  $\gamma'$  secondaire et tertiaire est calculée empiriquement sur la base des compositions SAT. Après cette analyse approfondie des caractéristiques du précipité, un programme de traitement thermique dans lequel le temps de maintien varie une température fixe

est appliqué sur les échantillons extrudés. L'analyse microstructurale montre des différences dans la fraction volumique et la morphologie de chaque type de précipité. Leur dureté est également mesurée et rapportée.

Le «design expérimental » est ensuite utilisée comme un outil pour optimiser le programme proposé, en faisant varier non seulement le temps de maintien, mais également trois autres facteurs: la vitesse de refroidissement, la température de maintien et la méthode de refroidissement à la température ambiante. La première conception est basée sur la matrice L8 de Taguchi. Il existe deux niveaux de facteurs (haut et bas) avec des répétitions. Les microstructures sont caractérisées par MEB et des tests de microdureté Vickers sont appliqués pour évaluer l'effet de chaque traitement thermique. L'analyse de régression des résultats a révélé que le facteur le plus important pour cette conception est la température de maintien. L'échantillon le plus mou et l'échantillon le plus dur ont une différence microstructurale significative, ce dernier ayant une distribution trimodale de précipités qui explique la différence de résistance.

La deuxième conception expérimentale est basée sur la conception composite centrale. Deux catégories d'échantillons sont examinées, l'une déformée et l'autre déformée et recuite, afin de vérifier si le traitement thermique ultime peut être appliqué à différentes étapes de traitement. Les résultats confirment qu'il y a un effet non négligeable de la microstructure initial, car il existe différents traitements thermiques qui se sont avérés les plus efficaces pour réduire la dureté pour les deux conditions. La division des précipités et des microstructures coralloïdes sont observées pour la première fois dans cet alliage. Deux mécanismes sont proposés pour réduire la dureté en fonction de la microstructure initiale.

# Contents

<b>ABSTRACT</b> .....	ii
<b>RÉSUMÉ</b> .....	iv
<b>Acknowledgements</b> .....	xiii
<b>Contributions of authors</b> .....	xiv
<b>Chapter 1 : Introduction</b> .....	1
<b>Chapter 2 : Literature review</b> .....	4
2.1 Introduction .....	4
2.2 Processing of cast and wrought superalloys.....	6
2.3 The microstructure of Ni-based superalloys .....	9
2.3.1 Introduction .....	9
2.3.2 Gamma prime ( $\gamma'$ ) phase.....	10
2.3.3 $\gamma'$ morphology and coherency.....	11
2.3.4 Trimodal distribution of $\gamma'$ in Ni-based superalloys .....	14
2.3.5 Microstructure of Rene 65 .....	19
2.4 Precipitation strengthening.....	20
2.5 Heat Treatments .....	22
2.6 Summary and scope of thesis .....	24
<b>Chapter 3 : Materials and Experimental Methodology</b> .....	26
3.1 Materials.....	26
3.2 Experimental Methods .....	26
3.2.1 Microscopy .....	27
3.2.2 Image analysis .....	28
3.2.3 Atom Probe Tomography (APT).....	29
3.2.4 Lattice parameter calculation.....	32
3.2.5 Heat Treatments.....	33
3.2.6 Experimental design .....	34
3.2.7 Microhardness tests .....	38
<b>Chapter 4 : Microstructural characterization of three different size of gamma prime precipitates in Rene 65</b> .....	40
Abstract .....	41
4.1 Introduction .....	41

4.2 Experimental procedure .....	43
4.3 Results and Discussion.....	45
4.4 Conclusions .....	58
4.5 Acknowledgements .....	59
4.6 Bibliography.....	60
<b>Chapter 5 : Microstructural characterization and mechanical properties of Rene 65 precipitates</b> .....	66
Abstract .....	67
5.1 Introduction .....	67
5.2 Experimental procedure .....	68
5.3 Results and discussion.....	70
5.4 Conclusions & Future Work .....	80
5.5 Acknowledgements .....	81
5.6 References .....	81
<b>Chapter 6 : Taguchi Design for heat treatment of Rene 65 components</b> .....	83
Abstract .....	84
6.1 Introduction .....	84
6.2 Experimental methods.....	86
6.3 Results and Discussion.....	89
Statistical analysis.....	89
Microstructural analysis .....	97
6.4 Conclusions .....	104
6.5 Acknowledgments.....	104
6.6 References .....	104
<b>Chapter 7 : Heat treatment optimization of a <math>\gamma'</math> strengthened nickel-based superalloy based on Central Composite Design</b> .....	107
Abstract .....	108
7.1 Introduction .....	108
7.2 Experimental methods.....	111
7.3 Results .....	116
Statistical analysis.....	116
Microstructural analysis .....	124
7.4 Discussion .....	129

7.5 Conclusions .....	132
7.6 Acknowledgements .....	133
7.7 References .....	134
<b>Chapter 8</b> : General Discussion .....	138
<b>Chapter 9</b> : Summary and Conclusions .....	142
<b>Chapter 10</b> : Future work.....	145
<b>Chapter 11</b> : Contribution to original knowledge.....	147
<b>Chapter 12</b> : Bibliography .....	148

## List of Figures

<b>Figure 2-1:</b> Evolution of high temperature capability of superalloys as a function of year <sup>[5]</sup> . The evolution of manufacturing is also presented. License to reuse the image granted from Cambridge University Press. ....	4
<b>Figure 2-2:</b> General process flow for manufacture of nickel-based superalloy product forms (processes in orange, products in blue). Redrawn from <sup>[32]</sup> . ....	6
<b>Figure 2-3:</b> L <sub>12</sub> crystal structure. Al (and substitute elements) positions are identified with pink color and Ni (and substitute elements) positions are identified with blue color.....	11
<b>Figure 2-4:</b> Schematic of the shape changes of a freely growing precipitate <sup>[73]</sup> . License to reprint granted from Elsevier.....	13
<b>Figure 2-5:</b> $\gamma'$ morphologies which can be developed in U720LI through heat treatment processes. All morphologies are a result of heat treatment precipitation, except primary $\gamma'$ , which remains throughout sub-solvus solution heat treatments <sup>[107]</sup> . License to reuse granted from Elsevier. ....	17
<b>Figure 2-6:</b> Effect of dislocation pairs on coherent precipitates (a) “weak” precipitates and (b) “strong” precipitates.” The APB effect on the precipitates is shown in black. <sup>[117]</sup> License to reuse granted by Elsevier. ....	21
<b>Figure 3-1:</b> Flowchart of Research Methodology.....	27
<b>Figure 3-2:</b> APT technique schematic. ....	29
<b>Figure 3-3:</b> Area of interest was selected to include all three precipitate sizes. ....	30
<b>Figure 3-4:</b> Tilted sample at 22° in preparation to create the wedge. ....	30
<b>Figure 3-5:</b> Creating the wedge with the ion beam in three steps.....	31
<b>Figure 3-6:</b> Micromanipulator before (left) and after (right) platinum welding.....	31
<b>Figure 3-7:</b> Welding of sample on Si pole top view (left) side view (right).....	31
<b>Figure 3-8:</b> Final tip for APT experiment.....	32
<b>Figure 3-9:</b> Fixture to hold samples, thermocouple attached to it (sample and thermocouple indicated with red arrows). ....	33
<b>Figure 3-10:</b> Sentro Box furnace interior view, thermocouple and sample positions indicated with red arrows. ....	34

<b>Figure 3-11:</b> Linear graph for L8 matrix: column numbers (left) interactions A*B, B*C and A*C (right), redrawn from <sup>[151]</sup> .....	36
<b>Figure 3-12:</b> Linear graph for L8 matrix: column numbers (left) interactions A*B, A*C, A*D (right), redrawn from <sup>[151]</sup> .....	36
<b>Figure 3-13:</b> Central Composite Design cube and star points schematic <sup>[4]</sup> .....	38
<b>Figure 4-1:</b> As received sample (a)low magnification as received condition, primary $\gamma'$ circled in yellow (b)high magnification of the as received condition, secondary $\gamma'$ examples indicated with red arrows and tertiary $\gamma'$ examples are circled in red. ....	46
<b>Figure 4-2:</b> EDS mapping of the as received sample highlighting differences in composition between secondary $\gamma'$ precipitates and the matrix (a)Ni (b)Cr (c)Ti (d) Al.....	47
<b>Figure 4-3:</b> SEM micrograph of the heat-treated sample. Red arrows indicate positions of tertiary $\gamma'$ .....	48
<b>Figure 4-4:</b> TEM bright field image indicating secondary $\gamma'$ morphology of the as received sample. ....	48
<b>Figure 4-5:</b> a) Tertiary $\gamma'$ clusters in $\gamma$ matrix b) Diffraction pattern of site 5a, arrows highlighting superlattice reflections c) simulated diffraction pattern by PDF-4 database.....	49
<b>Figure 4-6:</b> a) tertiary $\gamma'$ homogeneous distribution within the matrix b) HRTEM of 6a marked area highlighting tertiary $\gamma'$ c) IFFT on marked precipitate d) high magnification of marked 6c area highlighting dislocations on the interface. ....	50
<b>Figure 4-7:</b> (a) 3D reconstructed volume of the as received tertiary $\gamma'$ precipitates, highlighted by 13 at.% Cr iso-composition surfaces, in the $\gamma$ matrix. The two distinct sizes of tertiary large and small (quaternary) precipitates are indicated by the purple arrows. (b) A 1D compositional profile along the tertiary $\gamma'$ in $\gamma$ matrix. ....	51
<b>Figure 4-8:</b> Comparison of the compositions of major(top) and minor (bottom) alloying elements between the as received and heat-treated state. ....	56
<b>Figure 4-9 :</b> (a) APT 3D reconstruction of as received sample showing secondary and tertiary precipitates highlighted by 13 at.% Cr iso-composition surface. (b) & (c) show 1D concentration profiles along the two interfaces between the matrix and secondary precipitate. ....	57
<b>Figure 4-10:</b> (a) APT 3D reconstructed volume of the heat treated sample showing only secondary precipitates highlighted by 13 at.% Cr iso-composition surface. (b) 1D concentration profile along the interface between the matrix and the secondary precipitate.....	58
<b>Figure 5-1:</b> As extruded microstructure at x200 (left) and x500 (right).....	70
<b>Figure 5-2:</b> SEM images of multimodal $\gamma'$ precipitate size distribution in as-extruded Rene 65.71	
<b>Figure 5-3:</b> Representative SEM microstructures of 0 minute hold at 954°C heat-treated samples taken at: (a) and (c) low magnification of A <sup>1095</sup> <sub>30</sub> H <sup>954</sup> <sub>0</sub> WQ and A <sup>1095</sup> <sub>30</sub> H <sup>954</sup> <sub>0</sub> AC respectively and (b) and (d) high magnification A <sup>1095</sup> <sub>30</sub> H <sup>954</sup> <sub>0</sub> WQ and A <sup>1095</sup> <sub>30</sub> H <sup>954</sup> <sub>0</sub> AC.....	73
<b>Figure 5-4:</b> Representative SEM microstructures of 10 minute hold time at 954°C heat-treated samples taken at: (a) and (c) low magnification of A <sup>1095</sup> <sub>30</sub> H <sup>954</sup> <sub>10</sub> WQ and A <sup>1095</sup> <sub>30</sub> H <sup>954</sup> <sub>10</sub> AC respectively and (b) and (d) high magnification A <sup>1095</sup> <sub>30</sub> H <sup>954</sup> <sub>10</sub> WQ and A <sup>1095</sup> <sub>30</sub> H <sup>954</sup> <sub>10</sub> AC.....	74
<b>Figure 5-5:</b> Representative SEM microstructures of 30 minute hold time at 954°C heat-treated samples taken at: (a) and (c) low magnification of A <sup>1095</sup> <sub>30</sub> H <sup>954</sup> <sub>30</sub> WQ and A <sup>1095</sup> <sub>30</sub> H <sup>954</sup> <sub>30</sub> AC respectively and (b) and (d) high magnification A <sup>1095</sup> <sub>30</sub> H <sup>954</sup> <sub>30</sub> WQ and A <sup>1095</sup> <sub>30</sub> H <sup>954</sup> <sub>30</sub> AC.....	75

<b>Figure 5-6:</b> Representative SEM microstructures of 60 minute hold time at 954°C heat-treated samples taken at: (a) and (c) low magnification of A <sup>1095</sup> <sub>30</sub> H <sup>954</sup> <sub>60</sub> WQ and A <sup>1095</sup> <sub>30</sub> H <sup>954</sup> <sub>60</sub> AC respectively and (b) and (d) high magnification A <sup>1095</sup> <sub>30</sub> H <sup>954</sup> <sub>60</sub> WQ and A <sup>1095</sup> <sub>30</sub> H <sup>954</sup> <sub>60</sub> AC.....	76
<b>Figure 5-7:</b> SEM Image of A <sup>1095</sup> <sub>30</sub> H <sup>954</sup> <sub>60</sub> AC sample highlighting tertiary $\gamma'$ .....	76
<b>Figure 5-8:</b> Representative SEM microstructures of 120 minute hold time at 954°C heat-treated samples taken at: (a) and (c) low magnification of A <sup>1095</sup> <sub>30</sub> H <sup>954</sup> <sub>120</sub> WQ and A <sup>1095</sup> <sub>30</sub> H <sup>954</sup> <sub>120</sub> AC respectively and (b) and (d) high magnification A <sup>1095</sup> <sub>30</sub> H <sup>954</sup> <sub>120</sub> WQ and A <sup>1095</sup> <sub>30</sub> H <sup>954</sup> <sub>120</sub> AC.....	77
<b>Figure 5-9:</b> SEM image highlighting the details of larger secondary $\gamma'$ precipitates in A <sup>1095</sup> <sub>30</sub> H <sup>954</sup> <sub>120</sub> AC sample.....	77
<b>Figure 5-10:</b> Hardness Profile, blue bars for WQ and orange bars for AC. ....	78
<b>Figure 5-11:</b> Change in the average size of secondary $\gamma'$ precipitates as a function of hold time at 954°C differentiated by final cooling method. ....	79
<b>Figure 5-12:</b> Relationship between hardness and secondary gamma prime precipitate size.....	80
<b>Figure 6-1:</b> Interaction Lines. ....	88
<b>Figure 6-2:</b> Flow chart of Taguchi design analysis using Minitab software. ....	88
<b>Figure 6-3:</b> Hardness variation between replicates.....	91
<b>Figure 6-4:</b> Main effects plot for S/N ratios. ....	92
<b>Figure 6-5:</b> Main Effects plot for Means. ....	93
<b>Figure 6-6:</b> As received sample at low magnification. Red arrows indicate example positions of primary $\gamma'$ . ....	98
<b>Figure 6-7:</b> As received sample at higher magnification, highlighting secondary $\gamma'$ in cuboidal and spheroidal morphologies. ....	98
<b>Figure 6-8:</b> Hardest sample at low magnification. This was achieved by 25°C/min cooling rate from 1095°C to 800°C, hold for 30 minutes and then air cooling. Primary $\gamma'$ is highlighted at the grain boundaries.....	99
<b>Figure 6-9:</b> Hardest sample at high magnification. This was achieved by 25°C/min cooling rate from 1095°C to 800°C, hold for 30 minutes and then air cooling. Primary $\gamma'$ (red arrow) is surrounded by tertiary $\gamma'$ . Secondary(squares) and tertiary $\gamma'$ (circles) are present intergranular..	99
<b>Figure 6-10:</b> Softest sample at low magnification. This was achieved by 5°C/min cooling rate from 1095°C to 900°C, no hold and then gas quenching. Primary $\gamma'$ is highlighted along the grain boundaries. ....	100
<b>Figure 6-11:</b> Softest sample at high magnification. This was achieved by 5°C/min cooling rate from 1095°C to 900°C, no hold and then gas quenching. Secondary $\gamma'$ agglomerations are present intergranular. Tertiary $\gamma'$ was observed close to primary $\gamma'$ (red arrow) in a very small volume fraction. ....	100
<b>Figure 6-12:</b> Comparison with other samples that were held at 900°C. This was achieved by 5°C/min cooling rate from 1095°C to 900°C, 30-minute hold and then air cooling. Secondary $\gamma'$ agglomerations are present in this sample as well. ....	102
<b>Figure 6-13:</b> Comparison with other samples that were held at 900°C. This was achieved by 25°C/min cooling rate from 1095°C to 900°C, no hold and then air cooling. Smaller secondary $\gamma'$ as well as tertiary $\gamma'$ (circles) around primary $\gamma'$ (red arrows) are present in this sample.....	103

<b>Figure 7-1:</b> Trimodal distribution of $\gamma'$ precipitates in Rene 65. Primary $\gamma'$ is present on the grain boundaries (arrow), secondary and tertiary $\gamma'$ can be found intragranularly (circle) and tertiary $\gamma'$ is also present around primary $\gamma'$ (square) .....	110
<b>Figure 7-2:</b> Central Composite Design points schematic: circle (cube) and star(axial) positions indicate the different factor levels in the design. For this experiment a sum of 16 cube points, 12 center points in the cube and 12 axial points created a total of 40 run design.....	112
<b>Figure 7-3:</b> Heat treatment schematic.....	113
<b>Figure 7-4:</b> Solvus curve of $\gamma'$ in Rene 65 (adapted in $^{\circ}\text{C}$ from <sup>[14]</sup> ).....	114
<b>Figure 7-5:</b> Residuals versus order plot for deformed sample. No particular trend is observed. ....	120
<b>Figure 7-6:</b> Residuals versus order plot for deformed and annealed sample. No particular trend is observed. ....	120
<b>Figure 7-7:</b> Contour plots for deformed (D) samples that were gas quenched to room temperature. Legends on top of plots are in the form Y axis *X axis i.e. Hold Temperature (Y axis) * Cooling rate (X axis). Hardness units in HV, cooling rate in $^{\circ}\text{C}/\text{min}$ , hold temperature in $^{\circ}\text{C}$ , hold time in min and GQ indicates gas quench. ....	122
<b>Figure 7-8:</b> Contour plots for deformed (D) samples that were water quenched to room temperature. Legends on top of plots are in the form Y axis *X axis i.e. Hold Temperature (Y axis) * Cooling rate (X axis). Hardness units in HV, cooling rate in $^{\circ}\text{C}/\text{min}$ , hold temperature in $^{\circ}\text{C}$ , hold time in min and WQ indicates water quench. ....	122
<b>Figure 7-9:</b> Contour plots for deformed and annealed samples (DA) that were gas quenched to room temperature. Legends on top of plots are in the form Y axis *X axis i.e. Hold Temperature (Y axis) * Cooling rate (X axis). Hardness units in HV, cooling rate in $^{\circ}\text{C}/\text{min}$ , hold temperature in $^{\circ}\text{C}$ , hold time in min and GQ indicates gas quench. ....	123
<b>Figure 7-10:</b> Contour plots for deformed and annealed samples (DA) that were water quenched to room temperature. Legends on top of plots are in the form Y axis *X axis i.e. Hold Temperature (Y axis) * Cooling rate (X axis). Hardness units in HV, cooling rate in $^{\circ}\text{C}/\text{min}$ , hold temperature in $^{\circ}\text{C}$ , hold time in min and WQ indicates water quench.....	123
<b>Figure 7-11:</b> As received condition of the deformed sample. Primary $\gamma'$ is present on the grain boundaries and secondary $\gamma'$ is observed in cuboidal and spheroidal morphologies.....	124
<b>Figure 7-12:</b> Softest sample after heat treatment. Secondary $\gamma'$ could be observed at a uniform spheroidal morphology. ....	125
<b>Figure 7-13:</b> As received condition of the deformed and annealed sample. Primary $\gamma'$ is present on the grain boundaries and secondary $\gamma'$ is observed in cuboidal and spheroidal morphologies. ....	125
<b>Figure 7-14:</b> Secondary $\gamma'$ splitting. ....	126
<b>Figure 7-15:</b> Primary $\gamma'$ decomposing called “medusa” morphology. ....	127
<b>Figure 7-16:</b> Primary $\gamma'$ “coral” morphology. ....	127
<b>Figure 7-17:</b> Primary $\gamma'$ “coral” morphology. ....	128
<b>Figure 7-18:</b> Secondary $\gamma'$ precipitates after heat treatment are observed in various stages of splitting. ....	129

## List of Tables

<b>Table 2-1:</b> Nominal Compositions of Rene 88DT and Rene 65 in wt%.....	8
<b>Table 2-2 :</b> Examples of different size fractions of $\gamma'$ according to literature.....	15
<b>Table 2-3:</b> Elemental concentration (at%) of gamma prime in RR1000 alloy. License to reuse from <sup>[93]</sup> .....	19
<b>Table 3-1:</b> Nominal chemical composition of Rene 65 <sup>[28]</sup> .....	26
<b>Table 4-1:</b> Nominal chemical composition of Rene 65 <sup>[1]</sup> .....	43
<b>Table 4-2:</b> Point & ID analysis of the as received sample (in at. %). .....	46
<b>Table 4-3:</b> APT compositions of the matrix, the secondary and the tertiary $\gamma'$ precipitates in the as received sample. ....	52
<b>Table 4-4:</b> APT compositions of the matrix and the secondary $\gamma'$ precipitates after heat treatment. ....	52
<b>Table 4-5:</b> Lattice parameters of matrix and precipitates for as received and heat treated conditions.....	53
<b>Table 5-1:</b> Chemical composition of Rene 65 (wt%). .....	68
<b>Table 5-2:</b> Heat treatment terminology. ....	72
<b>Table 6-1:</b> Factors' levels.....	87
<b>Table 6-2:</b> Experimental design. ....	90
<b>Table 6-3:</b> Estimated Model Coefficients for S/N ratios. ....	93
<b>Table 6-4:</b> Estimated model coefficients for means.....	94
<b>Table 6-5:</b> Regression analysis on Taguchi results.....	95
<b>Table 6-6:</b> Summary of factor levels.....	97
<b>Table 7-1:</b> Nominal chemical composition of Rene 65 (wt%) <sup>[10]</sup> .....	111
<b>Table 7-2:</b> Factors' levels.....	114
<b>Table 7-3:</b> Central Composite Design and responses in HV for deformed “D” sample condition and deformed and annealed “DA” sample condition.....	116

## Acknowledgements

As this journey that we call a PhD degree comes to an end, there are many people that I would like to express my gratitude for making this an unforgettable experience.

First and foremost, to my supervisor Professor Stephen Yue for giving me the opportunity to start such an interesting project, his constant support and guidance throughout the years. Thank you, Professor for all the lessons and opportunities you have given me!

To Mr. Martin Therer and Dr. Andrew Wessman from GE Aviation, I am eternally thankful for giving me samples, the industrial point of view and feedback on my papers. It was a pleasure working on the Rene 65 project!

To all technicians and researchers that helped me through the years with experiments, thank you for all your help.

To Barbara, Leslie and June, thank you for always being there to help with administrative questions. Your help and laughter will stay with me forever!

To NSERC, CRITM, GE Aviation, MEDA, GREAT award and Graduate Mobility Award. I am grateful for funding my studies and giving me the opportunity to focus on my research without worrying for finances.

To all my colleagues and friends that made this experience in Montreal unforgettable.

To Konstantinos, who understands this process better than anyone. Thank you for listening to me and for all your help with everything.

To my mom Vicky, my dad Michalis and my brother Andreas for always listening to me and supporting me throughout this journey. This is dedicated to you.

## Contributions of authors

This thesis is comprised of a manuscript-based format, following the thesis preparation guidelines of McGill University. The following research articles are included as Chapters 4, 5, 6 and 7 in this thesis, respectively. Apart from the Atom Probe Tomography experiments of Chapter 4 that were performed at Max Planck Institute for Iron Research in Germany, all the other experiments were conducted at McGill University and each author's contribution is described in each chapter respectively:

### 1. Chapter 4

Published in *Materials Characterisation* journal as “*Microstructural characterization of three different size of gamma prime precipitates in Rene 65*” by Christina Maria Katsari, Shyam Katnagallu and Stephen Yue <sup>[1]</sup>

The candidate designed the outline, analyzed the SEM and TEM results, prepared and edited the manuscript. The candidate also conducted SEM on the samples, but the published version includes the micrographs taken by Mr. Nicolas Brodusch who is acknowledged in the manuscript. Dr. Shyam Katnagallu collected and analyzed the Atom Probe Tomography (APT) data and contributed to the writing of the results from APT section of the manuscript. Prof. Stephen Yue supervised the candidate, discussed the results and edited the manuscript.

### 2. Chapter 5

Published in *Proceedings of the 9th International Symposium on Superalloy 718 & Derivatives: Energy, Aerospace, and Industrial Applications* as “*Microstructural Characterization and Mechanical Properties of Rene 65 Precipitates*” by Christina Maria Katsari, Hanqing Che, Denzel Guye, Andrew Wessman and Stephen Yue <sup>[2]</sup>

The candidate prepared the manuscript and with Mr. Denzel Guye (co-op student in Hot Deformation laboratory under the supervision of herself and of Dr. Hanqing Che) they conducted the experimental work – heat treatments and SEM data acquisition and analysis. Dr. Hanqing Che provided feedback on the manuscript and discussions of the results. Dr. Andrew Wessman provided useful insights from the industrial point of view on the results and the manuscript. Prof. Stephen Yue supervised the students, discussed the results and edited the manuscript.

### **3. Chapter 6**

Published in *Journal of Materials Engineering and Performance* as “Taguchi Design for Heat Treatment of Rene 65 Components” by Christina Maria Katsari, Andrew Wessman, and Stephen Yue <sup>[3]</sup>

The candidate designed and conducted all the experiments. She prepared and edited the manuscript. Dr. Andrew Wessman provided useful insights from the industrial point of view on the results and the manuscript. Prof. Stephen Yue supervised the candidate, discussed the results and edited the manuscript.

### **4. Chapter 7**

Published in *Metallurgical and Materials Transactions A* journal as "Heat treatment optimization of a  $\gamma'$ -strengthened nickel-based superalloy based on Central Composite Design" by Christina Maria Katsari, Andrew Wessman, and Stephen Yue <sup>[4]</sup>.

The candidate designed and conducted all the experiments. She prepared and edited the manuscript. Dr. Andrew Wessman provided useful insights from the industrial point of view on the results and the manuscript. Prof. Stephen Yue supervised the candidate, discussed the results and edited the manuscript.

## Chapter 1 : Introduction

Superalloys are extraordinary materials that have been used since the 1940's<sup>[5]</sup> due to their high temperature and high strength capabilities in aerospace applications and, more specifically, in turbine engines. General Electric (GE) Aviation is one of the biggest engine manufacturers<sup>[6]</sup> and, in collaboration with Allegheny Technologies Incorporated (ATI) Specialty Materials, they developed an alloy that exceeded the temperature capabilities of Inconel 718, the alloy that has been largely used for decades<sup>[7]</sup>. This new alloy is called Rene 65 and is a derivative of the powder metallurgy superalloy Rene 88 DT. With the chemistry modifications, the new alloy could be cast and then worked, giving a cheaper processing route of ingots compared to Rene 88DT<sup>[8]</sup>. The higher temperature capability of Rene 65 comes from its microstructural characteristics and, more specifically, from the fact that it is strengthened only by gamma prime ( $\gamma'$ ) precipitates that remain stable for temperatures more than 700°C<sup>[9]</sup>. The total percentage of these precipitates is 40% in the as-forged condition<sup>[10]</sup>, which is a high amount for a strengthening phase. Therefore, Rene 65 is cheaper to manufacture and has better performance than the most used alloy. In fact, this alloy is so strong that it is challenging to manufacture a part without changing the final precipitate characteristics, since those precipitates offer the in-service advantage.

The research question could therefore be structured as: How can GE Aviation manipulate the microstructure of this promising alloy to easily manufacture parts without compromising their final performance? In order to tackle this engineering problem, there is a need to better understand the nature of the  $\gamma'$  strengthening precipitates, since those are the microstructural features that affect manufacturability the most. Rene 65 is relatively new compared to other alloys used in similar turbine engine parts, where there is an abundance in precipitate characterisation literature, so the first objective is to assess their differences in morphology and composition – if any.

“Superalloys are process-history sensitive”<sup>[11]</sup>, therefore different heat treatments will lead to various microstructures and corresponding hardness values. The goal would be therefore to create the optimum microstructure for manufacturing without jeopardizing the final properties that the precipitates offer (in other words, dissolve all precipitates). This optimum microstructure should correspond to hardness values that are comparable to the hardness values of alloys that have been previously manufactured with the same process. If that is successful, a thorough optimization of the thermomechanical processing will have been achieved. It is worth mentioning that this optimized heat treatment would be applied in a multi-step thermomechanical processing schedule, so its effectiveness on various initial microstructures needs to be evaluated.

Based on the above concepts, the research objectives of this PhD thesis can therefore be stated below:

1. Strengthening precipitate characterisation and identification of compositional differences between the three different sizes of  $\gamma'$  precipitates in the alloy Rene 65.
2. Heat treatment optimization via Experimental Design tools. The quantification of the effectiveness of the heat treatment will be measured by reduction in hardness values to be comparable to targeted hardness values that were used previously in the industrial environment.
3. Evaluation of the applicability of the optimized heat treatment to various steps of production by testing and analyzing samples from various thermomechanical processing histories.

Initially in Chapter 2, a literature review regarding Ni-based superalloys, their microstructure, processing, and heat treatment is conducted. It is important to understand the nature of trimodal precipitate distribution which appears in this alloy, as well as any other possible microstructural

feature, before designing a heat treatment that affects their size and distribution. In Chapter 3, a summary of all materials and experimental techniques is presented, apart from “Experimental Design” where more details are provided. The first objective is reached in Chapter 4, where two sample conditions – as- extruded and heat treated – are examined with microscopy techniques and atom probe tomography. In Chapter 5, a first approach of softening the samples is achieved, by introducing a non-traditional heat treatment and by varying one factor, time. The samples of this chapter are also in the as-extruded condition. In Chapter 6 and Chapter 7, the second objective of this thesis is met since the heat treatment schedule that is introduced in Chapter 5 is optimized by Taguchi design and Central Composite Design, respectively. In Chapters 6 and 7, the samples are subjected to different types of deformation than in Chapters 4 and 5. Therefore, from Chapters 5-7, the third objective is achieved, since various initial microstructures occur and the effectiveness of the proposed heat treatment on various steps of thermomechanical processing can be assessed. General discussion, conclusions resulting from this study, future work as well as the contributions to original knowledge, are presented in Chapters 8, 9, 10 and 11 respectively. The bibliography of Chapters 4-7 is included at the end of each chapter, since they were published as scholarly papers. Chapter 12 includes the bibliography of the remaining chapters.

## Chapter 2 : Literature review

### 2.1 Introduction

Superalloys are materials with extraordinary properties – as the name implies – which makes them a perfect candidate for various industrial applications from toaster wires<sup>[11]</sup> to gas turbine blades<sup>[5]</sup>. There are three categories that can be divided based on the majority element composition: nickel (Ni), nickel- iron (Ni-Fe), and cobalt (Co) -base alloys and they are generally used at temperatures above 540°C<sup>[11–14]</sup>. The Ni-Fe based alloys derive from stainless steels and are usually used in the wrought condition<sup>[11]</sup>. For cobalt and Ni-based superalloys the as-cast structures are used as well<sup>[12,15,16]</sup>. For more than 20 years (Figure 2-1), superalloys have also been produced by powder metallurgy routes<sup>[17–19]</sup>, which are now being used in additive manufacturing<sup>[20–22]</sup>.

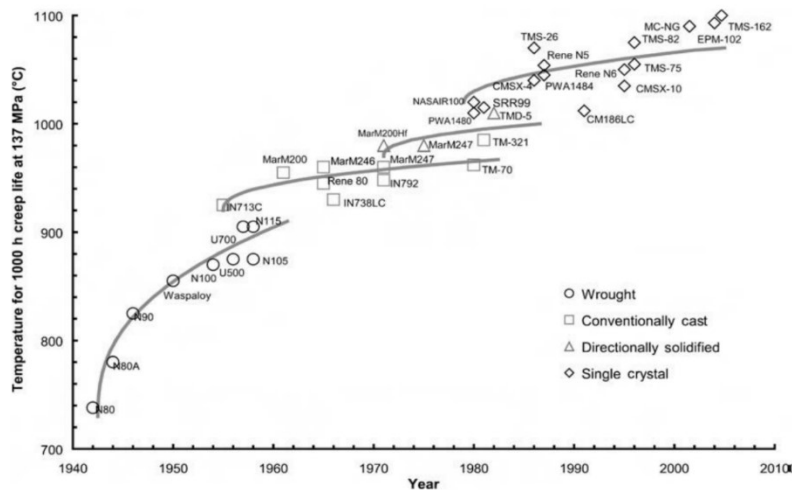


**Figure 2-1:** Evolution of high temperature capability of superalloys as a function of year<sup>[5]</sup>. The evolution of manufacturing is also presented. License to reuse the image granted from Cambridge University Press.

For turbine engines, there are two ways of increasing their high temperature performance: changing the design or changing the materials. Safran Aircraft Engines and GE Aviation have

collaborated and used both techniques to develop the Leading Edge Aviation Propulsion (LEAP®) engines<sup>[23,24]</sup>. More specifically, LEAP® has a 4th generation 3D aero design for the high pressure compressor, 3D woven carbon fiber composites which are made using the resin transfer molding process for the first stages of the compressor, ceramic matrix composites in the turbine, titanium aluminides and 3D printed fuel nozzle tips<sup>[25]</sup>. Furthermore, the disks of the low pressure turbine and high pressure compressor are made of Ni-based superalloy Rene 65<sup>[26,27]</sup>, the alloy that is studied in this thesis. All these improvements result in significant performance compared to an already successful model (CFM56) with a decrease of fuel consumption (15% improvement)<sup>[24]</sup>, reduced NO<sub>x</sub> emissions by half and 75% less noise<sup>[23]</sup>- a critical factor for airport regulations. The reduction in weight makes the airplanes that are powered by the LEAP ® engine fly for longer times (10 hours per day on average) while consuming less fuel<sup>[23]</sup>, which is a superior advantage for aircraft carriers.

Rene 65 is used in the LEAP® engines, mainly in the high and low pressure turbine part for forged disks and rings<sup>[10]</sup>. It can also be used in the high pressure compressor part<sup>[27]</sup>. It was developed by GE Aviation and ATI Specialty Materials in 2007, as a derivative of the powder metallurgy processed alloy Rene 88DT<sup>[28]</sup>. Rene 65 as a cast and wrought processed alloy, is less costly<sup>[29]</sup> to use for parts manufacturing than its predecessor (Rene 88DT), which is a powder metallurgy processed alloy<sup>[30]</sup>. Another advantage of Rene 65 is the higher temperature capability of more than 50°C operating temperature compared Inconel 718<sup>[9]</sup>. The latter was the most used Ni-Fe based superalloy in aerospace for 35 years in 2001<sup>[7]</sup> and it continues to be used in many applications till this day. Rene 65 is strengthened only by gamma prime ( $\gamma'$ ) precipitation<sup>[10,26,31]</sup> whereas Inconel 718 is mainly strengthened by gamma double prime ( $\gamma''$ ) which is unstable above 650°C and therefore, that is the maximum temperature that the alloy can operate<sup>[7,28]</sup>.

## 2.2 Processing of cast and wrought superalloys

The processing steps of cast and wrought superalloys are featured in the flowchart of Figure 2-2.

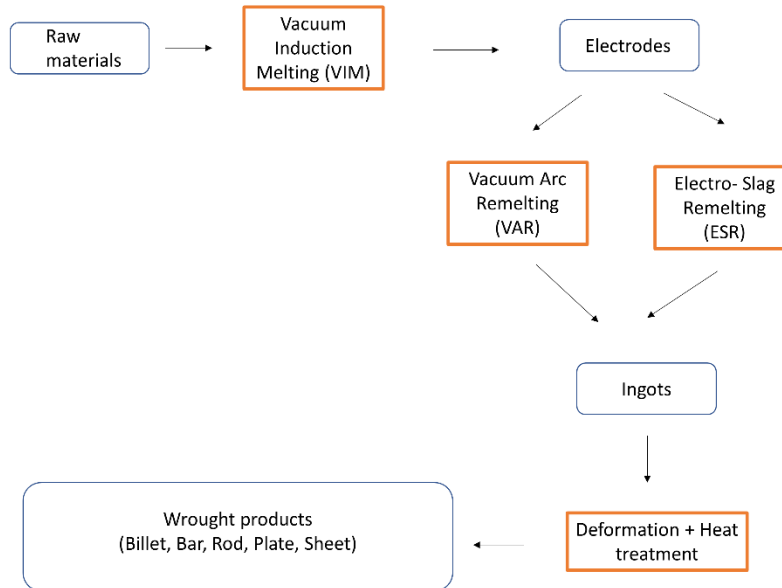


**Figure 2-2:** General process flow for manufacture of nickel-based superalloy product forms (processes in orange, products in blue). Redrawn from [32].

As superalloys were based on stainless steel, the melting technology that was developed in the 1960's for high-chromium ferrous alloys can be used for ingot production in this class of materials too<sup>[33]</sup>. Electric Arc Furnace (EAF)/Argon Oxygen Decarburization (AOD) is the cheapest way of melting<sup>[11]</sup> but it is not sufficient for the aerospace required cleanliness. Therefore, casting in vacuum was introduced with Vacuum Induction Melting (VIM) process, which reduces the oxygen and nitrogen percent<sup>[34,35]</sup>. In order to further improve the material cleanliness and/or the structure, the VIM products are used as electrodes for subsequent remelting processes such as Electro Slag Remelting (ESR) or Vacuum Arc Remelting (VAR) <sup>[11,34]</sup>. For complex shapes such as turbine blades with internal cooling system, a very popular casting technique is investment

casting<sup>[36,37]</sup>. Rene 65 is cast in a triple step melt-VIM//ESR/VAR <sup>[10]</sup> and can also be used in quadruple melt sequence<sup>[38]</sup>, which offers the high cleanliness needed for the applications.

Once all the elements are added, the molten metal is poured into molds and it solidifies into various microstructures. The castings that have equiaxed polycrystalline (PC) microstructures are solidified without a specific crystal growth orientation. In turbine blades, there are special solidification techniques which can be used to enhance mechanical properties in specific orientations (i.e. parallel to the grains)<sup>[14]</sup>. Directional solidified parts (DS)<sup>[39]</sup> are comprised of grains grown in specific orientation whereas in single crystals (SC)<sup>[40,41]</sup> there are no grain boundaries. On the contrary, in the PC cases, mechanical properties are isotropic<sup>[42]</sup>. Rene 65 is a polycrystalline superalloy in its current applications<sup>[43,44]</sup>.

While the high temperature capability is very important for turbine engine components, the ability to be formed in various shapes – sometimes quite complex- is also equally important. Formability (or workability) can be quantified by taking into consideration from the flow stress curve, the maximum stress/strain before fracture which is determined by tensile, torsion or compression tests<sup>[45]</sup>. To produce a wrought part from a casting, the ingot is plastically deformed (increase of dislocation density) until it reaches the desired shape and properties. To achieve this, mechanical forces that surpasses the yield stress are applied. The deformation can occur in high temperatures (above recrystallization temperatures called hot working) or room temperature (below recrystallization temperatures called cold working). By introducing heat to the process, either already existing in hot working or by adding a heat treatment step after cold working, the dislocations are removed<sup>[42,46]</sup>, which enables more deformation to be applied. Superalloys are sensitive to thermo-mechanical processing steps, and their sequence has an important effect on the final properties of the components<sup>[11,47]</sup>.

A common wrought process for turbine disks is forging<sup>[36]</sup>. Forging is not used solely for the purpose of forming the shape but also, through microstructural control, helps in improving tensile properties, stress-rupture behavior, creep strength and low-cycle fatigue life <sup>[11]</sup>. The two large categories that forgings can be separated are open and closed die forgings<sup>[11,46]</sup>. Compression tests simulate the upsetting which is the simplest operation of the open die category<sup>[46]</sup>. Other forging methods include swaging, ring rolling or a combination of two of the above methods <sup>[11]</sup>.

Not all alloys can be cast and forged, it depends on their composition<sup>[5]</sup>. In the cases where casting is not possible, powder metallurgy routes are followed<sup>[29]</sup> and the products can then be forged<sup>[46]</sup>. Rene 65 is a derivative of a powder metallurgy processed alloy (Rene 88DT)<sup>[9,10,31]</sup> and with a slight change in composition of some elements (Table 2-1), casting and either conventional hot – open die forging<sup>[10,48]</sup>, ring rolling<sup>[10]</sup> and hot rolling with a two high mill <sup>[49]</sup> methods are applicable for Rene 65. The 1% iron allowed the use of scrap in castings without forming the deleterious sigma phase <sup>[28,50]</sup>. Lower carbon levels decrease the carbide formation, which is not needed as strength or grain pinning mechanisms<sup>[5]</sup>, since secondary and tertiary  $\gamma'$  precipitates are the strengthening precipitates and primary  $\gamma'$  serves as a grain pinning mechanism, as discussed in detail later in this review.

**Table 2-1:** Nominal Compositions of Rene 88DT and Rene 65 in wt%.

Alloys	Ni	Cr	Mo	W	Co	Fe	Nb	Ti	Al	Zr	B	C
R88DT <sup>[30]</sup>	Bal.	16	4	4	13	-	0.7	3.7	2.1	0.03	0.015	0.03
R65 <sup>[28]</sup>	Bal.	16	4	4	13	1	0.7	3.7	2.1	0.05	0.016	0.01

## 2.3 The microstructure of Ni-based superalloys

### 2.3.1 Introduction

Superalloys are the perfect candidates for aerospace applications such as gas turbine components, since they can work under typical engine temperatures, which can reach up to 1600°C [51–53]. The high temperature capability of the Ni-based category reaches sometimes 90% of their melting temperature<sup>[52]</sup>, which derives from the face centered cubic (FCC) structure of the matrix<sup>[42]</sup>. Nickel does not present phase transformations at higher temperatures, as opposed to, for instance, titanium alloys, where  $\alpha$  phase transforms to  $\beta$  phase at elevated temperatures<sup>[54]</sup>. Additionally, the FCC structure provides 12 slip systems, which leads to high ductility<sup>[42]</sup>. The diffusion rate of elements in FCC, as it is a closed packed structure, is low, leading to reduced thermally activated creep in addition to the high microstructural stability<sup>[5]</sup>. The Ni matrix is enriched with solid solution elements such as Cr, Co, Mo, Fe and W<sup>[52]</sup>, which offer substitutional solid solution strengthening. Chromium and aluminum offer hot corrosion protection by forming oxide layers on the surface<sup>[55]</sup>.

Aluminum, along with other elements, such as Ti and Nb, partition to second phases and mainly in precipitates<sup>[56]</sup>. Precipitation hardening through the formation of  $\gamma'/\gamma''$  [ $\text{Ni}_3\text{Al}/\text{Ni}_3\text{Nb}$ ] phases a common strengthening mechanism in Ni-based superalloys<sup>[57–59]</sup>.

Other phases that could form in Ni-based superalloys are carbides and borides, which precipitate mainly on the grain boundaries but can also be found intragranular [14,52,60]. Their role is to hinder the grain boundary movement and therefore improve high-temperature creep<sup>[5,14,56]</sup>. The formation of carbides is promoted by the addition of Cr, Mo, W, Hf, Ta and Ti which form the  $\text{M}_{23}\text{C}$ ,  $\text{M}_6\text{C}$ ,  $\text{MC}$  types, where M stands for each element<sup>[5,11,52,56]</sup>. Carbides can have a negative effect too as they may participate in the fatigue cracking propagation or create a notch effect by

oxidation<sup>[14,61]</sup>. Also, MC carbides degenerate which reduces stress – rupture properties<sup>[62]</sup>. The carbide size as well as location (within the grain or on the grain boundaries) is important to determine the beneficial or deteriorating character of the particles<sup>[14]</sup>. Under certain thermomechanical conditions Topologically Closed Packed (TCP) phases may form, deteriorating the mechanical properties<sup>[52,63]</sup>. The TCP phases P,  $\mu$ , R,  $\sigma$  and Laves are deleterious brittle intermetallics that precipitate on the grain boundaries and are promoted by W, Re and Mo additions above a certain level<sup>[64]</sup>. Since there are specific element additions and their appearance is usually after thermal exposure for long times<sup>[26]</sup>, the suppression of their formation can be controlled by alloy design and optimized heat treatments.

### 2.3.2 Gamma prime ( $\gamma'$ ) phase

The  $\gamma'$  phase in superalloys follows the formula of  $A_3B$ . The A position is occupied by less electropositive elements such as Ni, Co and Fe whereas more electropositive elements, such as Al, Ti, Ta and Nb, occupy the B position. Nickel can be substituted by Co and Al by Ti, Nb and Ta; both Al and Ni can be substituted by Mo, Fe or Cr<sup>[52]</sup>. In the binary system (Ni-Al),  $\gamma'$  has the formula of  $Ni_3Al$  and the interatomic bonding is covalent<sup>[65]</sup>. As the difference in electropositivity among two elements increases, it is more likely for them to form an intermetallic compound and not a substitutional solid solution which is the case for elements that are close in the periodic table<sup>[42]</sup>. Mihalisin and Pasquine<sup>[66]</sup> found Cr in both A and B sites. Booth-Morrison et al. calculated that Ta and Cr substitute preferentially the B site<sup>[67]</sup>.

Atoms are organized in cubic  $L1_2$  crystal structure to form the  $\gamma'$  precipitate<sup>[68]</sup>. The corresponding Bravais lattice is simple cubic but the  $L1_2$  structure is an ordered face-centered cubic (FCC)<sup>[69]</sup>. This means that specific elements occupy the A(Ni) positions and the B(Al) positions<sup>[70]</sup>, as indicated with blue and pink colors in **Figure 2-3** respectively.

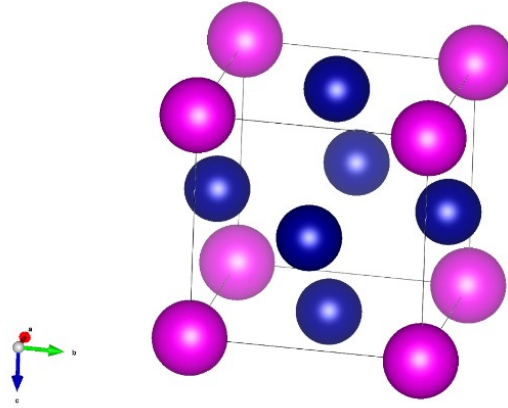


**Figure 2-3:** L<sub>12</sub> crystal structure. Al (and substitute elements) positions are identified with pink color and Ni (and substitute elements) positions are identified with blue color.

### 2.3.3 $\gamma'$ morphology and coherency

Microstructurally,  $\gamma'$  can be found in many morphologies. The first shape observed was spheres, followed by cubes<sup>[52]</sup>. It was later discovered that the shape of the precipitate was related to the lattice mismatch<sup>[11,52]</sup>. The lattice mismatch is calculated with the formula  $\delta = [(\alpha_{\gamma'} - \alpha_{\gamma}) / 0.5(\alpha_{\gamma'} + \alpha_{\gamma})]$  where  $\alpha_{\gamma'}$  and  $\alpha_{\gamma}$  are the lattice parameters for the precipitates and the matrix respectively <sup>[71]</sup>. At 0-0.2% lattice mismatch Hagel and Beattie <sup>[72]</sup> observed  $\gamma'$  as spherical, then from 0.5% to 1% cuboidal and above 1.25% mismatch,  $\gamma'$  was observed in plates. Grosdidier mentions that there is a correlation of the  $\gamma'$  shape with : (i) size, (ii) volume fraction and (iii) number of precipitates<sup>[73]</sup>. According to Donachie, the levels of Mo and the ratio of Al/Ti also affect the morphology<sup>[11]</sup>.

Gamma prime precipitates form from a supersaturated matrix through the nucleation and growth mechanism<sup>[73]</sup>, although there are some references that mention the spinodal decomposition mechanism, which was not proven or applied in “real superalloys” <sup>[12,74]</sup>. When a phase nucleates heterogeneously, it begins from a surface already created (i.e a grain boundary) <sup>[42,70]</sup>, and therefore since the interfacial energy is reduced, it is easier to form. On the contrary,

homogeneous nucleation of a new phase occurs in the internal part of another phase (i.e. intragranular) and it is more difficult to form as Gibbs free energy ( $\Delta G^*$ ) needs to drop below a critical value<sup>[42,70]</sup>. However, as mentioned above,  $\gamma'$  is an ordered FCC crystal structure, and the Ni matrix is also FCC, which leads to  $\sim 0.1\%$  mismatch between them, with the  $\gamma$  matrix, is very compatible and therefore with low interfacial energy and facilitates homogeneous nucleation as well as leads to long-time stability<sup>[73,75]</sup>.

It seems that all  $\gamma'$  begins to nucleate as spheres and then, depending on the coherency with the matrix they change their morphology<sup>[73]</sup>. There is a critical size which the coherent precipitates can reach until this shape it is not energetically favorable anymore, since the elastic energy density is higher for phases that are coherent compared to incoherent. As growth continues after the critical size has been reached, dislocations form on the interfaces of the precipitate with the matrix in order to relax the stresses that have developed from the misfit and this leads to the precipitate losing its initial coherency<sup>[76]</sup>.

Ricks et al<sup>[77]</sup> mentions that the morphology of  $\gamma'$  particles transitions in the following sequence: “spheres – cuboids – cuboidal arrays – dendrites” which is similar to Grosdidier’s<sup>[73]</sup> sequence “sphere – cube – octocube – octodendrite – dendrite”. A schematic is presented in **Figure 2-4**. Grosdidier<sup>[73]</sup> supports that the growth characteristics are diffusion controlled in the later stages, whereas the first two transitions are related to atomic jumps at the interface whereas Ricks mentions that it is “partially diffusion controlled”<sup>[77]</sup>.

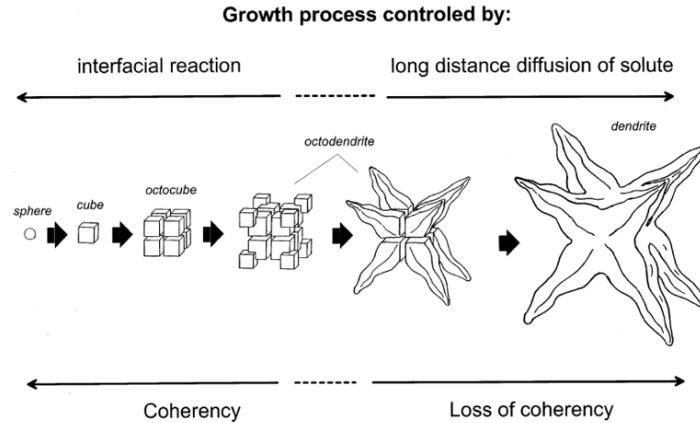


**Figure 2-4:** Schematic of the shape changes of a freely growing precipitate<sup>[73]</sup>. License to reprint granted from Elsevier.

Ricks et al in <sup>[77]</sup> reinforce the idea that the morphology depends on coherency strain since they conclude that the transition from spheres to cuboids and then to cuboidal arrays depends on the lattice misfit in the alloy. If there are many precipitate nucleation sites that could cause overlap of the diffusion fields, the spheres will not completely grow to dendrites according to their observations. The dendritic morphology can lead to coherency loss. This was observed only in alloys with negative and near zero misfits, whereas, in alloys with positive misfit it was not completely lost. Grosdidier et al <sup>[73]</sup> analyzed alloys with negative misfit and their observation on coherency loss moving from spheres to dendrites (**Figure 2-4**) agrees with Ricks et al's. According to Hazotte et al <sup>[78]</sup> the growth sequence depends on alloy chemical composition and the heat treatment parameters.

Grosdidier et al <sup>[73,78]</sup> and other groups<sup>[79-83]</sup> observed the so-called “split”  $\gamma'$  morphologies. These morphologies occur during coarsening in “elastically and strongly constrained systems”<sup>[81]</sup> during aging and the mechanism is mainly related to the elastic interaction energy, which is the energy from the interaction between each precipitate with its neighbours. Apart from the elastic interaction energy, the total energy state of a coherent precipitate is also controlled by elastic strain

energy caused due to lattice misfit and the interfacial energy between the precipitate with the matrix<sup>[82,84]</sup>. When splitting occurs, the interfacial energy is obviously increasing since more interfaces are created. Therefore, to minimize the total energy state, the elastic interaction energy needs to be reduced after the split. The energies can be calculated before and after the split by using the microelasticity <sup>[81,82,84,85]</sup> theory to explain this counter-intuitive phenomenon. The split morphology is considered the equilibrium shape since it occurs after the total energy is reduced and it has been observed in alloys with large misfit between  $\gamma$  and  $\gamma'$  <sup>[86]</sup>.

Cooling rate is a possible factor for splitting. In Fan et al's work<sup>[87]</sup>, with a slow cooling rate ( $<6$  °C/min), the precipitates grew from "spheres to cuboids with concave, dendritic shape  $\gamma'$  and final split-off dendritic branches" as a cause of the coherent strain that occurred. Doi et al<sup>[88]</sup> mention slow cooling rate favors splitting into an octet, whereas isothermal aging favors a split into a doublet.

Qiu and Andrews <sup>[89]</sup> on the other hand suggest that the irregular-shape  $\gamma'$  is not caused due to splitting, rather due to coarsening and 'coalescing' of small  $\gamma'$  precipitates. In this work RR1000 alloy was slowly continuously cooled from supersolvus annealing temperature and was not aged. This work is supporting the theory of Doherty<sup>[90]</sup> who hypothesizes that the driving force for the coalescing of two particles may be due to the reduction in strain of the matrix that is among them.

#### **2.3.4 Trimodal distribution of $\gamma'$ in Ni-based superalloys**

Apart from uniform morphologies (e.g., spheres), in some Ni-based superalloys  $\gamma'$  has been observed in three distinct sizes called primary, secondary, and tertiary  $\gamma'$  that have various morphologies. It seems that there is no specific precipitate size range corresponding to each of them and the terminology is being used to describe a descending size of precipitates, which nucleate at different temperature ranges. The only distinction that researchers seem to agree upon

is that primary  $\gamma'$  is in the scale on a few microns, secondary  $\gamma'$  is hundreds of nm and tertiary  $\gamma'$  tens of nm [5]. For example, Unocic et al [91] observed secondary  $\gamma'$  of 350 nm and tertiary  $\gamma'$  of 30 nm. Nevertheless, Fahrman et al [92] observed 40 nm secondary  $\gamma'$ .

**Table 2-2** :Examples of different size fractions of  $\gamma'$  according to literature.

Superalloy	Primary ( $\mu\text{m}$ )	Secondary (nm)	Tertiary (nm)	Reference
<b>RR1000</b>	1-10	100	50	[5]
<b>RR1000</b>	0.5-3	90-300	5-90	[93]
<b>N18</b>	4.3 $\pm$ 1.8	210 $\pm$ 80	20	[94]

A few examples of the nickel-based superalloys that are composed of multimodal  $\gamma'$  precipitate distribution are Udimet 720, Udimet 720 Li, LSHR, IN100, NR3, TMW-4M3, RR1000, N18, Rene 104, Rene 88 DT (R88DT) and Rene 65 [30,31,59,93,95–101]. It is worth mentioning that all these alloys except Udimet 720, TMW-4M3 and Rene 65, are processed by powder metallurgy.

In superalloys with microstructures that consist of multimodal  $\gamma'$  precipitates, the size of smaller precipitates (tertiary  $\gamma'$ ) as well as the total precipitate volume fraction are the main features that affect the strength [102]. According to Reed [5], when the temperature of the solution heat-treatment is below the solvus,  $\gamma'$  which has not dissolved (alternatively called primary  $\gamma'$ ) pins the grain boundaries and hinders the matrix grain growth. This promotes fatigue resistance and is similar to the effect of carbides/borides on solid solution strengthened superalloys. When the solution temperature is above solvus, primary  $\gamma'$  is dissolved which leads to coarser grains and therefore promotes creep resistance. Indeed, Jiang et al [103] observed differences in grain size in alloy LSHR when heat treating super- and sub- solvus. The pinning effect of intergranular primary  $\gamma'$ , was only observed in the sub-solvus samples that resulted in the finer grain size.

Second and third population precipitates within the grains are called secondary and tertiary  $\gamma'$ , and their sizes are typically  $\sim 100$  nm and  $\sim 50$  nm, respectively according to Reed<sup>[5]</sup>. This is due to nucleation, growth, and coarsening kinetics, that take place when the samples are isothermally solutionized and aged<sup>[5]</sup>.

Further precipitation can occur during cooling, since the equilibrium volume fraction  $\gamma'$  does not fully precipitate during the isothermal solution treatment and aging steps<sup>[5]</sup>. Papadaki et al <sup>[104]</sup> found that during cooling from the super-solvus solution temperature, the growth characteristics of secondary  $\gamma'$  is a combination of both diffusion and interface mechanisms, while the growth of tertiary  $\gamma'$  is primarily controlled by an interface mechanism. Also, there was a definite effect of cooling rate to the precipitate size distribution. Jiang <sup>[103]</sup> found fine spherical morphology of secondary  $\gamma'$  when the samples were cooled from subsolvus compared to supersolvus, due to the faster cooling. According to Sarosi et al <sup>[98]</sup> tertiary  $\gamma'$  can precipitate either during quenching at high interrupt-temperatures (950°C) or during cooling with 5 °C/ min cooling rate. According to Semiatin et al.<sup>[105]</sup> secondary  $\gamma'$  precipitates (supersolvus solution treated and cooled at 139 °C/min -fast rate or 11 °C/min-slow rate) nucleation sites are affected by cooling rate since faster cooling rates lead to many sites that do not grow much whereas slower cooling rates have the opposite effect; coarse precipitates and not that many in volume fraction. As far as the morphologies are concerned, faster cooling rates led to spherical morphologies and slower rates to irregular morphologies<sup>[105]</sup>. Similarly, Fan et al <sup>[87]</sup> observed that, with increasing cooling rate, there was a meaningful drop in the average precipitate size, while, simultaneously, there was an increase in the nucleation sites. In Masoumi et al's work <sup>[106]</sup> on AD730, a slower cooling rate (10°C/min) from the solution temperature led to butterfly shape  $\gamma'$  morphologies, whereas higher (120°C/min) rates led to spherical shapes. Similarly,<sup>[107]</sup> in Udimet720Li the size and morphology

of secondary  $\gamma'$  were influenced by the cooling rate, although the range was higher in this case. In the highest cooling rates,  $\gamma'$  was observed within the matrix as fine spheres (12.7 °C/sec), whereas irregular-shaped precipitates were formed with slower cooling rate (1.3°C/sec). When the cooling rate was even slower (0.12 °C/sec), the shape changed to dendritic and fan-type. Therefore, according to many researchers<sup>[77,92,97,108,109]</sup> in addition to the previous observations reported above, the size distribution and morphology of secondary and tertiary precipitates depends on the cooling rate. Thus, it should be a necessary parameter to be included in the design of a softening heat treatment. It seems that the literature trend shows slower cooling rates leading to coarse and irregular particles that are less effective in hindering dislocation motion (compared to small spherical particles) and would therefore effectively make the alloy softer.

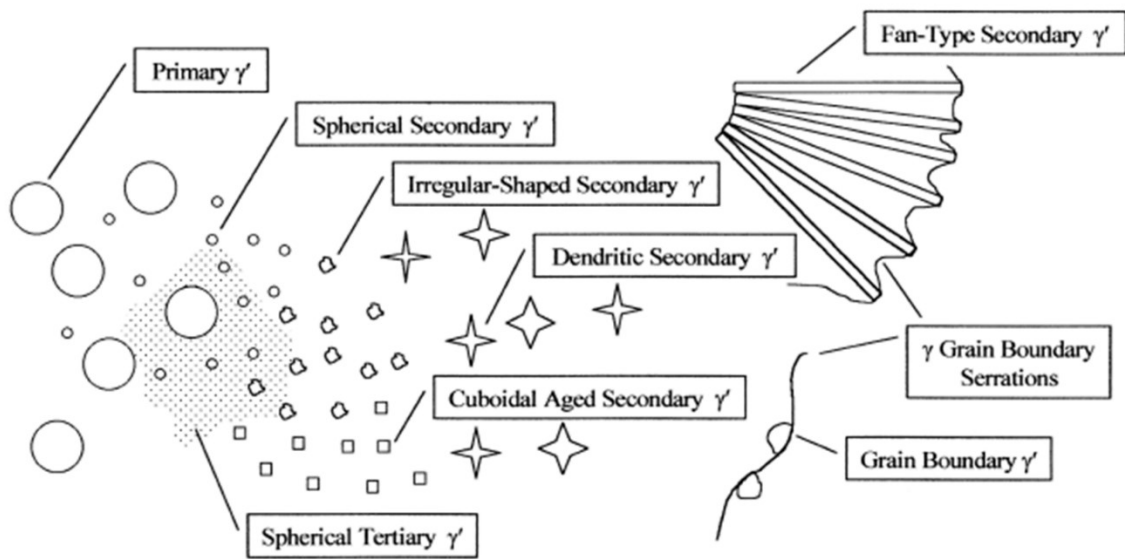


**Figure 2-5:**  $\gamma'$  morphologies which can be developed in U720LI through heat treatment processes. All morphologies are a result of heat treatment precipitation, except primary  $\gamma'$ , which remains throughout sub-solvus solution heat treatments<sup>[107]</sup>. License to reuse granted from Elsevier.

Singh et al<sup>[108]</sup> established a theory that explains the multiple precipitate nucleation that they observed in R88DT, the predecessor of Rene 65. As the samples are continuously cooled from

solution temperature, the driving force for precipitate nucleation is increasing. When the first population (primary  $\gamma'$ ) starts nucleating, a portion of this energy is used for the precipitation. At this stage, Al and Ti are consumed to form the  $\text{Ni}_3(\text{Al,Ti})$  and the area around primary  $\gamma'$  has a local surplus of the matrix stabilizing elements such as Co and Cr, which move through diffusion to equilibrate the composition. As the temperature continues to decrease, the diffusion of elements is not as fast and therefore, in the regions far away from the first population that has already formed, these elements are depleted and not replenished as fast, which leads to a local surplus of  $\gamma'$  stabilizing elements (i.e. Al,Ti). This is the driving force for the second population (secondary  $\gamma'$ ). Similarly, at much lower temperatures, diffusion is very slow but there is high undercooling, which acts as a driving force for the nucleation of a third precipitate population, tertiary  $\gamma'$ . As far as growth characteristics are concerned, primary precipitates grow fast (high temperature-high diffusion of elements) so they are observed in an irregular/ cuboidal shape. The secondary  $\gamma'$  precipitates are spherical in this alloy and smaller in size than the primary  $\gamma'$  precipitates, since the elements do not diffuse as fast and R88DT is a low  $\gamma/\gamma'$  misfit alloy. Since their volume fraction is larger than the primary precipitates, the diffusion field of each precipitate's growth overlaps with their neighbours, which is another factor that affects their growth. It is worth noting at this point that this is not the case for all secondary precipitates observed in this alloy or other alloys. Different morphologies can occur as described previously based on composition and lattice misfit of the precipitates. Tertiary  $\gamma'$  has the slowest growth kinetics (lowest formation temperature, slow diffusion) and most of  $\gamma'$  formed have been already used in precipitating primary and secondary  $\gamma'$ , so it is usually observed as small spheres.

While a terminology based on precipitate size / time of formation has been established, there are few studies regarding compositional differences between the three sizes in cast and

wrought alloys <sup>[110,111]</sup>. In contrast, there is a larger volume of work performed on powder metallurgy processed alloys <sup>[93,109,112,113]</sup>. Chen <sup>[93]</sup> observed a compositional difference in some elements, mainly between primary and either secondary or tertiary  $\gamma'$  in powder metallurgy alloy RR1000 (Table 2-3).

**Table 2-3:** Elemental concentration (at%) of gamma prime in RR1000 alloy. License to reuse from <sup>[93]</sup>

<b>Precipitate</b>	<b>Cr</b>	<b>Co</b>	<b>Al</b>	<b>Mo</b>	<b>Ti</b>	<b>Ta</b>	<b>Hf</b>	<b>Ni</b>
<b>Primary</b>	3.3±0.1	11.0±0.2	12.4±0.2	0.7±0.1	10.0±0.1	2.0±0.1	0.7±0.1	Bal.
<b>Secondary</b>	2.1±0.1	8.6±0.1	14.8±0.3	0.7±0.1	9.8±0.1	1.6±0.1	0	Bal.
<b>Tertiary</b>	2.1±0.2	7.5±0.3	16.5±0.4	1.0±0.2	9.4±0.4	1.7±0.2	0	Bal.

### 2.3.5 Microstructure of Rene 65

Rene 65 has a trimodal precipitate distribution<sup>[9,114]</sup>. The primary  $\gamma'$  precipitates form during the transition from ingot to billet (hot deformation)<sup>[43]</sup> and pin the grain boundaries<sup>[28]</sup>, suppressing grain growth during the following deformation steps (e.g. forging). Their size is a few microns<sup>[114]</sup>. Secondary and tertiary  $\gamma'$  are dissolved at these high temperatures and form during continuous cooling<sup>[43]</sup> as described above for Rene 88 DT, or during aging<sup>[9,31]</sup>. The secondary  $\gamma'$  sizes are a few hundred nanometers<sup>[114]</sup> or less<sup>[9]</sup>, while tertiary  $\gamma'$  precipitates a few tens of nanometers<sup>[9]</sup>, which both depend on the heat treatment parameters (i.e. cooling rate). Those smaller populations are coherent precipitates and offer the strength<sup>[43]</sup>, which is beneficial for the final application, and simultaneously a challenge during processing. Other phases observed in the microstructure of Rene 65 include carbides, nitrides and borides, which are small in number and

their size does not affect mechanical properties<sup>[28,114]</sup>. TCP phases can also form after overaging, which have a negative effect on creep properties<sup>[26]</sup>.

## 2.4 Precipitation strengthening

Ni-based superalloys employ the usual strengthening mechanisms; solid solution and grain boundary, precipitation and work hardening. When there is a trimodal precipitate distribution, precipitation strengthening contributes the most to alloy strength<sup>[74,115]</sup> and mainly when the precipitates are coherent with the matrix<sup>[76]</sup>.

The strength occurs from the resistance to dislocation motion. Depending on the precipitate size, volume fraction as well as their ability to be cut or by-passed, there are different mechanisms activated<sup>[57]</sup>.

Dislocations tend to cut (shear) the precipitates that are small<sup>[116]</sup>. For monomodal  $\gamma'$  distribution<sup>[102]</sup>, if the dislocation bending angle is between  $120^\circ$  and  $180^\circ$ , a particle is indicated as “weak and shearable”, whereas if the angle is between  $0^\circ$  and  $120^\circ$ , the particle is indicated as “strong and shearable”<sup>[117]</sup>. The angle is related to the precipitate size and the type of dislocation (i.e. edge/screw)<sup>[117]</sup>. Since  $\gamma'$  is an ordered precipitate<sup>[118]</sup>, which means that the elements occupy specific positions in the unit cell<sup>[70]</sup>, when this ordering is disturbed by a line defect, an anti-phase boundary (APB) is created. This increases the resistance (called anti-phase boundary energy-APBE) and causes chemical strengthening. To remove this effect, dislocations travel in pairs so the order that is lost when the first dislocation (leading dislocation, Figure 2-6-I) passes can be restored when the second one (trailing dislocation, Figure 2-6-II) moves behind it<sup>[5,58,117]</sup>.

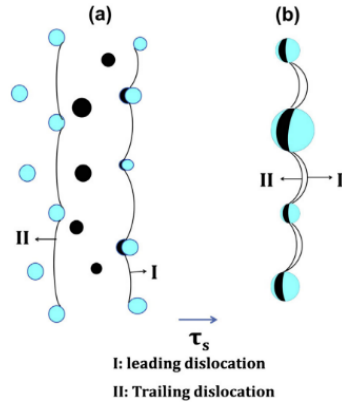


**Figure 2-6:** Effect of dislocation pairs on coherent precipitates (a) “weak” precipitates and (b) “strong” precipitates.” The APB effect on the precipitates is shown in black.<sup>[117]</sup> License to reuse granted by Elsevier.

In the “weak pairing” case, the leading dislocation is located in different particle than the trailing dislocation<sup>[58,102]</sup>. The disordered precipitates, which were cut by the leading dislocation, cause the trailing dislocations to move towards the leading dislocation. This counterbalances in a portion the leading dislocation’s APBE as the further inside it moves the higher the resistance force of the precipitate. When the precipitates are small, this mechanism can lower the energy and as a result the dislocation is able to go across the particle<sup>[117]</sup>.

When the precipitates are large, (“strong pairing”<sup>[58,102]</sup>), they produce a high APBE and the line tension force cannot counterbalance the high energy APB force of the precipitate and the dislocation remains within the particle<sup>[117]</sup>. Galindo-Nava et al<sup>[102]</sup> created a model that took into account monomodal and multimodal precipitate distributions and proved that, for the latter, the most significant effect on strength derived from the size and volume fraction of the tertiary  $\gamma'$  population.

As the size increases, after a critical radius has been established, the dislocations bow around the precipitates (Orowan looping)<sup>[119]</sup>. This is the case when the precipitates are also scarcely located within the matrix<sup>[57]</sup>. Galindo-Nava et al found that the contribution of the Orowan stress to the overall yield strength is very small <sup>[102]</sup>.

To quantitatively measure the change in strength through various thermomechanical processing steps, where the material might not be enough to machine tensile coupons, hardness tests can be performed. These tests are fast, easy, inexpensive and they are able to show the resistance of the material to plastic deformation <sup>[42,120,121]</sup>. The results can later be used to correlate with other mechanical properties such as tensile strength<sup>[42]</sup>. Nevertheless, since the test is non-destructive, ductility cannot be calculated from this test.

## **2.5 Heat Treatments**

Heat treating is a processing step given to parts made of superalloys to develop their final product properties. The most common heat treatment categories are<sup>[11,122]</sup>:

- Stress relieving
- Solution annealing
- Precipitation (age) hardening

Stress relieving has the goal to remove or minimize stresses in work-hardened pieces without triggering the recrystallization mechanism. They are used in non-age hardenable nickel alloys at intermediate temperatures that range from 425 to 870 °C, depending on the composition of the alloy and the degree of work hardening <sup>[123]</sup>.

Solution anneal is performed at 1150 to 1315 °C and its purpose is to dissolve secondary phases such as carbides and precipitates in the matrix , increasing the grain size which leads to better stress-rupture properties<sup>[123,124]</sup>. This step is usually followed by water quenching to room

temperature to keep the solutes in the solid solution<sup>[122,125]</sup> or air cooling<sup>[126]</sup>. For example, in Nimonic 115, a solution anneal at 1190°C was followed by air cooling<sup>[127]</sup>.

As mentioned before, the effect of cooling rate from solution annealing temperature is important for the final size and morphology of  $\gamma'$  precipitates, which affect the overall strength. On the contrary, when solid-solution nickel-based alloys are annealed, cooling rate has minimal effect in the degree of hardness according to ASM's Handbook guidelines for heat treatments of Ni-based superalloys<sup>[128]</sup>. To save time and limit the probability of secondary phase formation (i.e. sigma), fast cooling rates are preferred.

Age hardening is performed at intermediate temperatures, similar to stress relieving for the non-age hardenable alloys (425 to 870 °C), but in this case the purpose of the heat treatment is to maximize the strength by precipitating a second phase scattered within the matrix<sup>[122,129]</sup>, which acts as barrier to dislocation motion. According to Garat et al<sup>[130]</sup>, the common aerospace component heat treatment sequence is aging at 720°C for 8h, cooling with 50°C/h until 620°C for 8h and then air cool . The total aging time is usually more than 5 hours<sup>[128]</sup>.

The common practice of those heat treatments includes their application in sequence (i.e. solution anneal and then age hardening<sup>[32,79]</sup> )with the ultimate goal to maximize the strength for the final application. For example, in CMSX-10 after solution anneal, the first aging occurs at 1152°C and then there are two more aging treatments at 871°C and 760°C, which precipitate fine  $\gamma'$ <sup>[131]</sup>. In NR6 the heat treatment steps included annealing for two hours followed by two aging treatments (for 24hours at 700 °C and 4 hours at 800 °C respectively) for creep resistance<sup>[132]</sup>.

As mentioned previously, the heat treatment parameters affect the precipitate shape evolution according to Hazotte<sup>[78]</sup>.

## 2.6 Summary and scope of thesis

In summary, Rene 65 is a cast and wrought Ni-based superalloy which is currently being used in commercial airplane engines. Due to its relatively recent development, previous studies were focused on optimizing the precipitate characteristics for the final application (i.e., disks and blades in compressor part of jet engines). With this work, we aim to focus on optimizing the precipitate characteristics to ease the manufacturing of the parts.

Rene 65 has a trimodal  $\gamma'$  precipitate distribution and, according to literature from other alloys that possess similar microstructures, there can be differences in chemical composition among the three precipitate sizes. Therefore, before designing and optimizing the heat treatment aimed at manufacturing, the first step is to fully characterize the strengthening precipitates (i.e., morphology, chemical composition), since those are the phases that would affect the strength the most. In contrast to most studies in superalloys, our goal is to minimize the effect of the strengthening precipitates, as the softer the material the easier it is to manufacture. More specifically, the goal would be to achieve a similar hardness profile of alloys that are currently manufactured with the same processing steps. Hardness is a fast and easy method to compare mechanical properties before and after a heat treatment and can be later correlated to other mechanical properties.

The parts to be manufactured can be cold deformed to increase strength via work-hardening, improve dimensional accuracy and reduce operational costs related to high temperatures. For these microstructures, a solution annealing heat treatment above the solvus temperature would soften the material by removing all precipitates, which are present in the as cast/as forged condition, but since the primary  $\gamma'$  population serves as a pinning mechanism for grain boundaries, this would affect the final mechanical properties. For multiple steps of cold

deformation, it is important therefore to design a heat treatment that solution anneals without compromising the effect of grain size pinning from the precipitates and be industrially applicable.

The above have been the main motivation for this PhD thesis and the research conducted would compliment the literature regarding superalloy heat treatments, which are specific for manufacturing purposes. Also, a thorough precipitate characterization of the  $\gamma'$  precipitates of Rene 65 will enhance the literature of alloys that possess multimodal precipitate distributions in their microstructures.

## Chapter 3 : Materials and Experimental Methodology

This chapter contains all the materials and experimental methods used in this thesis throughout Chapters 4-7, which have been also published individually in each paper.

### 3.1 Materials

Rene 65 Ni-based superalloy was the only alloy studied in this thesis. Nevertheless, the thermomechanical history of the samples provided by GE Aviation was different to identify the applicability of a proposed heat treatment to various steps of production.

The three as-received conditions were:

1. As- extruded (hot deformed) cylinders of 9 x Ø 6 ( $\pm 0.1$ ) mm dimensions.
2. Cold deformed industrial parts of  $\sim 1$ cm thickness.
3. Hot deformed and super-solvus annealed industrial parts of  $\sim 1$ cm thickness.

Samples of condition 1 were machined to the cylindrical shape and were shipped to McGill, where they were used in the as-received shape. Samples of conditions 2 and 3 originate from industrial parts and they were cut to square samples (0.5mm \* 0.5mm) at McGill. Their nominal composition can be seen in Table 3-1:

**Table 3-1:** Nominal chemical composition of Rene 65 <sup>[28]</sup>.

Element	Ni	Fe	Co	Cr	Mo	W	Al	Ti	Nb	B	C	Zr
wt. %	55.42	1.0	13.0	16.0	4.0	4.0	2.1	3.7	0.7	0.016	0.015	0.05
at. %	54.95	1.04	12.84	17.91	2.43	1.27	4.53	4.5	0.44	0.09	0.073	0.03

### 3.2 Experimental Methods

The samples were used for various heat treatments, starting from varying one factor at a time, which is the traditional approach, and then following the Design of Experiments approach. All conditions, heat treated and as - received, were metallographically prepared for microhardness

tests to evaluate the softening effect of the heat treatment. In Chapters 4, 5 and 6 all samples were investigated with microscopy techniques whereas in Chapter 7, where a larger number of experiments was performed, only the softest conditions and the as-received conditions were analyzed with Scanning Electron Microscopy (SEM). In Chapter 4, where a detailed precipitate characterization was performed, higher resolution techniques such as Transmission Electron Microscopy (TEM) and Atom Probe Tomography (APT) were also applied. The flowchart of the research methodology can be seen in **Figure 3-1** and each step is further analyzed in this Chapter.

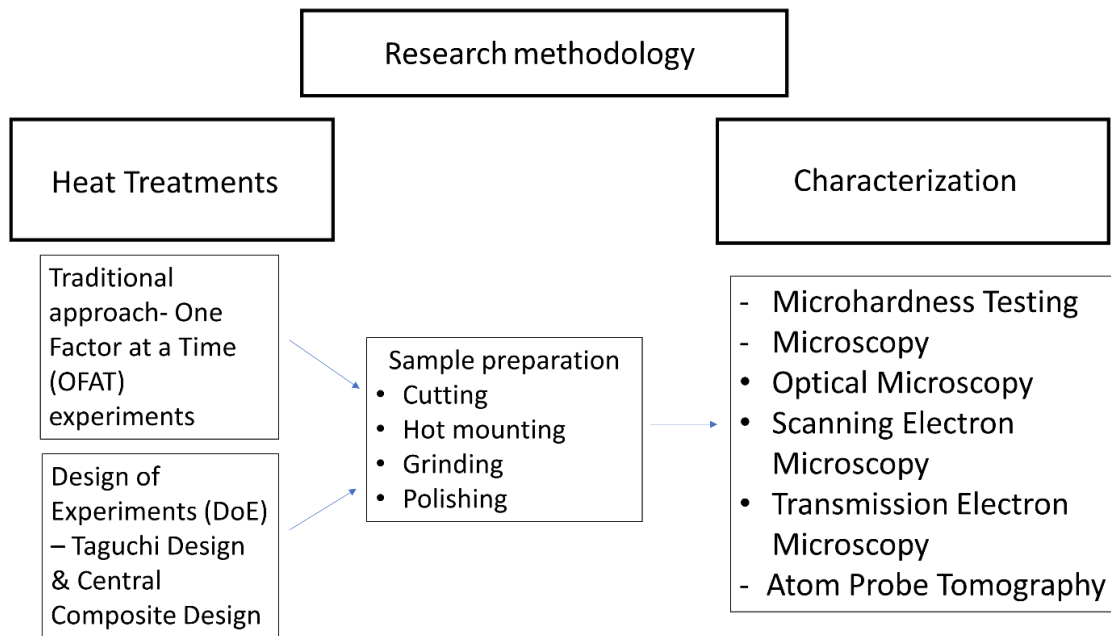


**Figure 3-1:** Flowchart of Research Methodology.

### 3.2.1 Microscopy

#### *Sample preparation*

Where necessary, the samples were cut using either a linear precision saw (Buehler IsoMet 5000) or an abrasive cutter (Buehler Delta™ AbrasiMet), depending on the initial size, using Buehler and Bruker abrasive blades.

The cut samples were then hot mounted and metallographically ground by hand with SiC papers (240 – 1200 grit) followed by hand polishing with diamond solution of 3 μm and 1 μm

particle size. The final step of polishing was either 1  $\mu\text{m}$  diamond solution for the tests where etching followed, or by 0.05  $\mu\text{m}$  colloidal silica for mirror finish.

To reveal the  $\gamma'$  precipitation under SEM conditions, the  $\gamma$  matrix was selectively removed by electropolishing and electroetching at 15V for 10 seconds and 5V for 5 seconds, respectively at room temperature. The  $\gamma$  etchant was methanol-based (64% methanol and 30% ethylene glycol) with additions of perchloric acid (6%).

For TEM samples, mechanical grinding with SiC papers as above was followed by jet polishing of 3mm disks with 10% vol. perchloric acid in methanol solution at  $-30^\circ\text{C}$  (cooled by liquid nitrogen).

### *Equipment*

In this thesis, 3 Hitachi Scanning Electron Microscopes (SEM) were used – SU3500, SU8000, SU8320 - for high resolution imaging at magnifications up to x80K, coupled with Energy Dispersive Spectroscopy (EDS) for qualitative analysis of  $\gamma'$  and matrix. TEM analysis was performed by FEI Tecnai G2 F20 Cryo-scanning transmission electron microscope (STEM).

For imaging, in the SU3500, 20kV accelerating voltage was used, while in the SU8000 it was 3kV. For compositional analysis of primary and secondary  $\gamma'$ , 10kV was used to detect all elements present, but for tertiary  $\gamma'$  since their size is a scale smaller, their composition could not be evaluated by this EDS condition due to the much larger interaction volume. A CASINO<sup>[133]</sup> simulation was performed that showed the interaction volume at 10kV was about 250 nm.

### **3.2.2 Image analysis**

For the quantification of precipitate size, ImageJ image analysis software was used. The measurements were performed manually after calibrating each image with the scale bar from the microscope. The measurement involved drawing two lines in the precipitate feature covering the X (horizontal axis of the image) and Y (vertical axis of the image) axes of the precipitate and

measuring the values. To get an average value, approximately 50 precipitates, where available, from five different regions were measured. The average values of each condition were reported in the form:  $X (\mu\text{m}/\text{nm}) \pm \text{standard deviation} \times Y(\mu\text{m}/\text{nm}) \pm \text{standard deviation}$ .

### 3.2.3 Atom Probe Tomography (APT)

Sample preparation and APT experiments were conducted at Max Planck Institute for Iron Research with the help of Dr. Shyam Katnagallu. APT is a high-resolution microscopy technique where the chemical composition of each phase can be identified. A sharp tip ( $<100\text{nm}$ ) is created, and a voltage is applied on it. The atoms evaporate one at a time and they travel until they hit a position sensitive screen which is connected to a time-of-flight (TOF) detector. Since each element is unique, they have unique TOF values, and this is how the composition is determined. With the position sensitive screen, the tip can be re-constructed to a 3D image, indicating the position of each phase with the different composition<sup>[134,135]</sup>.

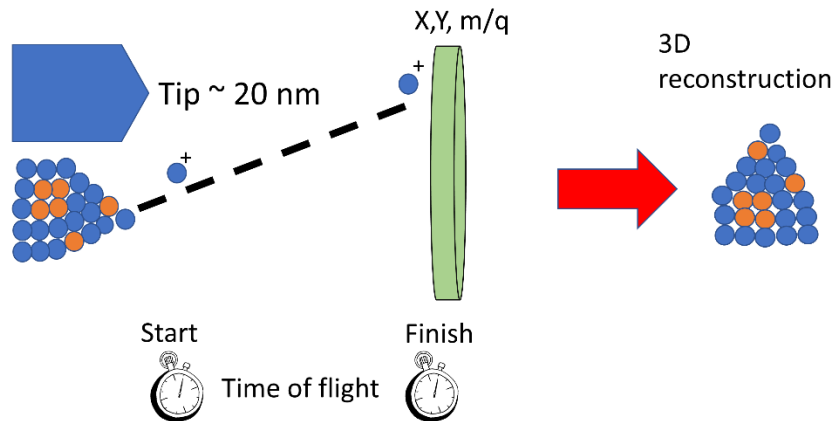


**Figure 3-2:** APT technique schematic.

### Sample preparation

In situ site-specific specimen preparation for APT by Plasma Focused Ion Beam (PFIB) (Thermofisher Helios) was performed according to protocols described in [136]. Representative images of the process are presented below from **Figure 3-3** to **Figure 3-8**.

As a first step, the area of interest is located. In this case, an area where all three precipitate sizes were present was selected.

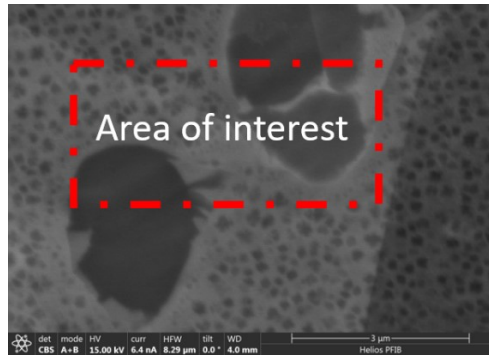


**Figure 3-3:** Area of interest was selected to include all three precipitate sizes.

Then the sample is tilted at 22° in order to create the wedge with the ion beam.

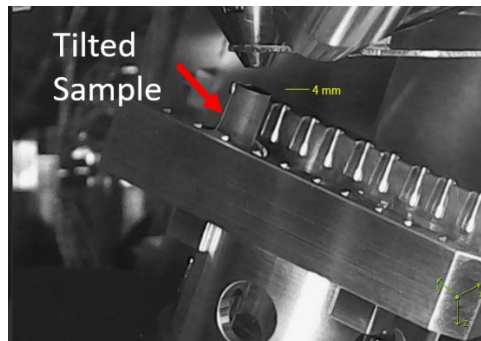


**Figure 3-4:** Tilted sample at 22° in preparation to create the wedge.

The ion beam is milling both sides to create an inverse pyramid for ~ 5 μm of thickness. Then, the ion beam is also milling at the left side of the wedge to begin the process of the lift-off.

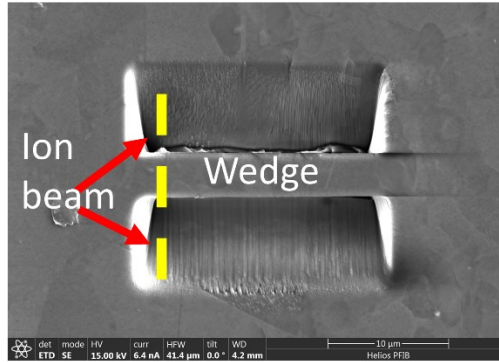


**Figure 3-5:** Creating the wedge with the ion beam in three steps.

To lift the sample out, a micromanipulator is used, which is welded to the wedge by ~500 nm platinum deposition. Once the sample is attached from the left side, the ion beam is milling the right side and the sample can be lifted off (Figure 3-6). Then the lift-off is placed on the top of a Si pole (Figure 3.7) and is welded with platinum on both sides.

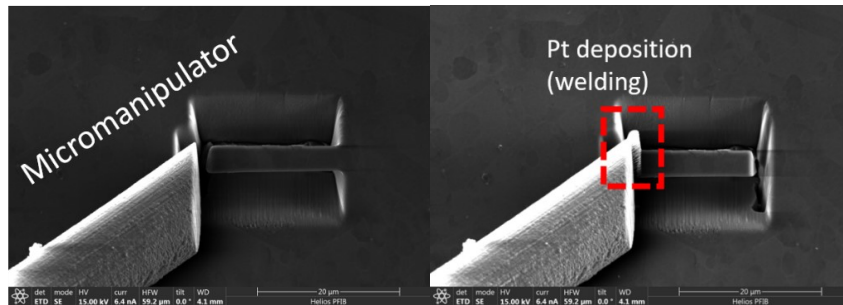


**Figure 3-6:** Micromanipulator before (left) and after (right) platinum welding.

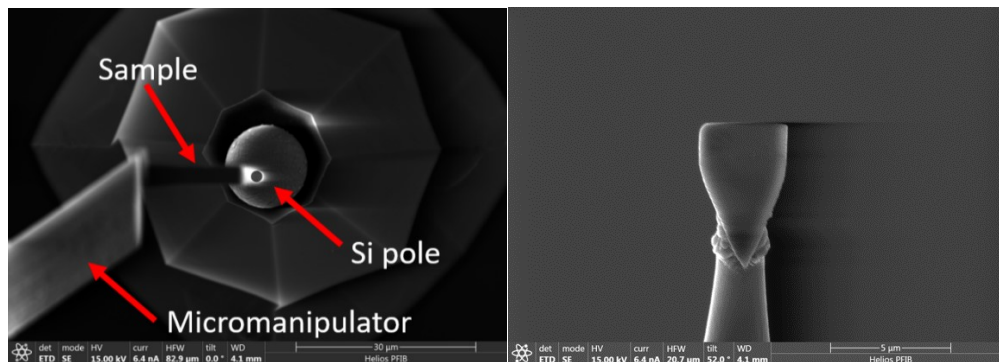


**Figure 3-7:** Welding of sample on Si pole top view (left) side view (right)

Once the sample is welded, the ion beam is milling from above to create a needle with the final tip thickness of ~40nm diameter.

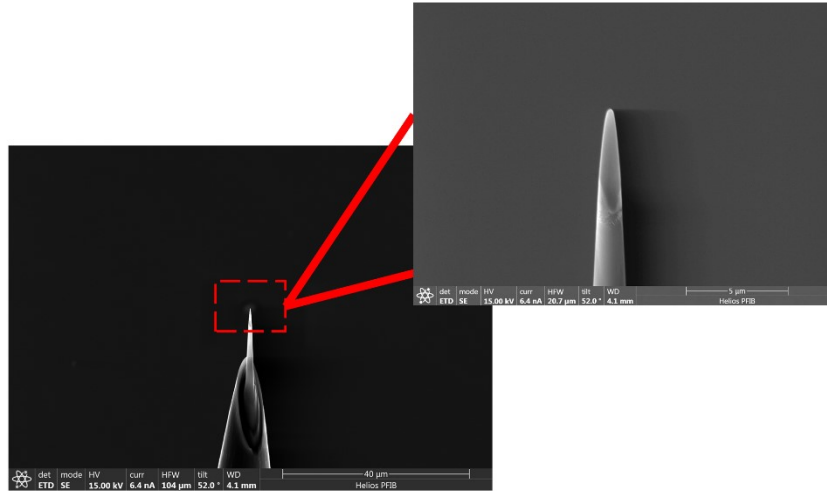


**Figure 3-8:**Final tip for APT experiment

#### *Equipment*

Local electrode atom probe (LEAP) 3000XR and 5000HR were used to evaluate the chemical compositions.

#### **3.2.4 Lattice parameter calculation**

To empirically calculate the lattice parameters of the matrix and the three size precipitates the program “Program MAP\_NICKEL\_LATTICE” was used. The program is based on a neural network and it was developed at Cambridge University<sup>[137–139]</sup>. The inputs are the chemical composition of each element and the temperature. For the chemical composition of the primary  $\gamma'$  precipitates the values from EDS measurements were used, whereas for the matrix, secondary  $\gamma'$  and tertiary  $\gamma'$  the APT compositions were used for higher accuracy. The carbon and boron compositions were not included due to the limitations of the program and the data collected from EDS/APT.

### 3.2.5 Heat Treatments

For the heat treatments in Chapters 3 and 4, an infrared furnace was used with a thermocouple attached to it as can be seen in **Figure 3-9**.

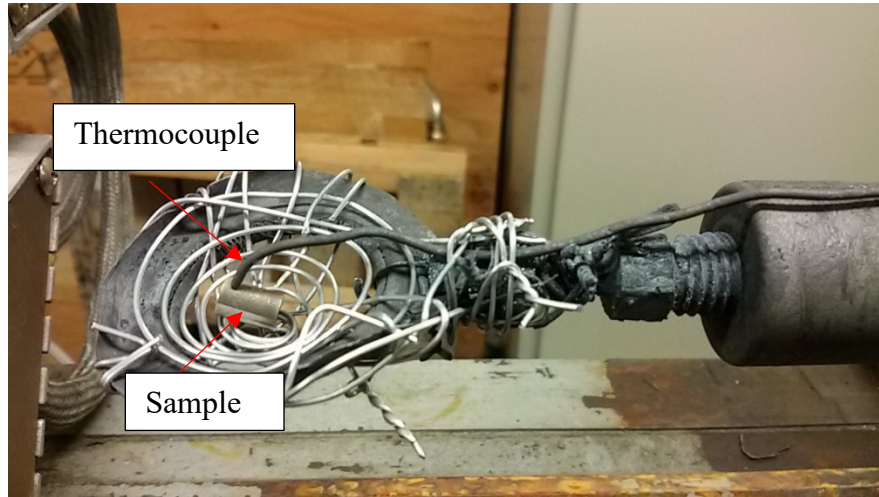


**Figure 3-9:** Fixture to hold samples, thermocouple attached to it (sample and thermocouple indicated with red arrows).

In Chapters 5 and 6, a Sentro Tech box furnace was used (**Figure 3-10**). In this case, the thermocouple was inside the furnace and the reproducibility was validated by inserting two samples located adjacent and then measuring their hardness values. Since the difference was less than 3%, it was considered a viable method. This furnace is equipped with a Eurotherm 2408 process controller which made possible to vary furnace cooling rates which was a parameter in the designs tested in those Chapters.

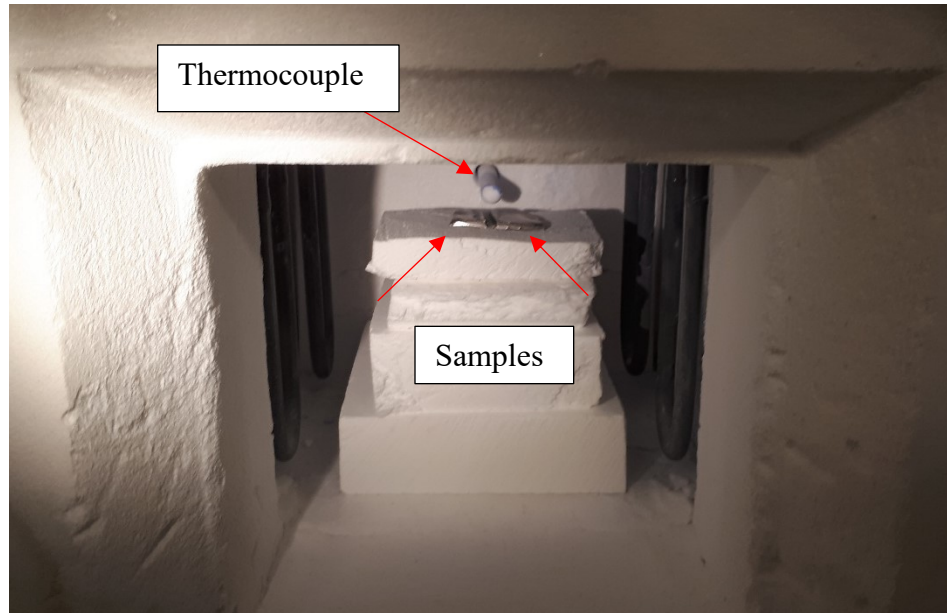


**Figure 3-10:** Sentro Box furnace interior view, thermocouple and sample positions indicated with red arrows.

### 3.2.6 Experimental design

#### *Introduction*

The traditional experimental procedure consists of the variance of one parameter and then measurement of the effect this parameter has on a desired outcome. For example, in many papers studying aging heat treatments, the varying parameter is time measured in hours. Another parameter can be the aging temperature. To examine the effect of both parameters on i. e. hardness values, one would vary first the time and then the temperature, evaluating their effects individually. With this way though – which called One-Factor-At-a-Time (OFAT) approach, the researcher would not have been able to estimate the interaction of the two factors, if there were any. This traditional approach also has the risk of conducting more experiments than necessary, to find the optimum solution, which increases the time and cost in many cases.

Design of experiments (DoE) or Experimental Design is the process of thorough planning and analyzing the experiment with the goal to achieve accurate and unbiased conclusions effectively and efficiently<sup>[140]</sup>. To have “statistically significant” outcomes when performing an

experiment, it is important to include statistical methods when analyzing the data collected<sup>[141]</sup>. An industrial scale experiment is considered successful when it is well planned, i.e., when the selected design is appropriate for the variables that need to be tested. Then, the data collected should be analyzed considering statistical methods from a team that understands the engineering goal of the experiment <sup>[142]</sup>.

DoE has been applied in many fields, from agriculture<sup>[143]</sup> to pharmaceutical industry<sup>[144]</sup>. In manufacturing, there are two categories of variables, which are otherwise called parameters<sup>[145]</sup> or factors<sup>[146]</sup>: qualitative and quantitative<sup>[142]</sup>. For quantitative factors, the range of numerical values (otherwise called factor levels) as well as the means to measure them (i.e equipment, unit etc), and how to control them needs to be identified <sup>[142,147]</sup>. Qualitative factors are given coded values for low and high levels arbitrarily which does not affect the outcome of the design<sup>[148]</sup>. An example could be gas quenching and water quenching as levels for factor “cooling method”. Those “values” are qualitative and therefore each of them could be considered as either the high or low level.

According to J. Antony<sup>[142]</sup>, the most used designs in manufacturing are factorial designs at two and three levels, as they allow the examination of a combination of different factors on a specific outcome. When all possible combinations of factors and their levels are performed i.e., a 3-factor experiment, where each factor has two levels, lead to a “*full factorial design*”, so in the aforementioned example, the full factorial will be  $2^3 = 8$  runs of experiments. When a fraction of that is performed it is called “*fractional factorial design*”, i.e 4 experiments would be half fractional factorial design<sup>[149]</sup>. When a small number of parameters need to be studied (i.e. less than 4), the  $2^k$  full factorial design is used<sup>[142]</sup>. The correlation of factors with the measured outcome is often described by linear equations<sup>[142,147,148,150]</sup>. When designing a new experimental

procedure, it is better to use the most parameters possible to narrow down which factors to study in depth at later stages (screening designs), even though some of the resolution of the outcome might be lost [151,152].

*Taguchi designs*

Taguchi designs in materials science have been extensively used in optimization of machining parameters [153–158] as well as additive manufacturing [159,160] and other tribology applications [161].

Taguchi designs are focused on a small number of experiments (low cost) and high quality [162]. Interactions between factors are not usually calculated, although, if they are important, there are linear graphs that can determine which interactions are possible to be calculated [151].

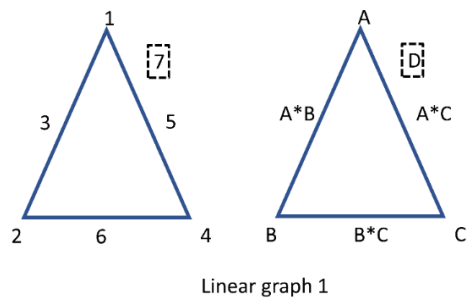


**Figure 3-11:** Linear graph for L8 matrix: column numbers (left) interactions A\*B, B\*C and A\*C (right), redrawn from [151].

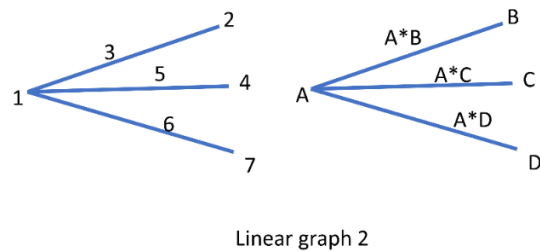


**Figure 3-12:** Linear graph for L8 matrix: column numbers (left) interactions A\*B, A\*C, A\*D (right), redrawn from [151].

When using Taguchi's designs, there are two categories of parameters, the ones that can be controlled (signal) and the uncontrolled (noise). The goal is to reduce the variance of the process at its early stages to increase the quality [163]. To increase the robustness of the design, higher signal-to-noise ratio (S/N) leads to higher quality, as it suggests which control factors (signal) can minimize the effects of the noise factors [162,163]. Another measured outcome in Taguchi designs is the mean, which represents "the average response for each combination of control factor levels" [164].

In this thesis, the Taguchi L8 matrix was used for heat treatment of deformed samples with calculation of interactions as described in **Figure 3-11**.

#### *Response Surface Method designs*

"All models are wrong but some are useful" George Box [165]

Response surface methods is a group of statistical techniques which help the experimenter build empirical models and explore the maximum/minimum outcome occurring from the different levels of the factors in a design [151]. They are used after screening experiments which have identified which factors are significant [166]. The sequential experiments have a goal to increase step by step the knowledge of the system to move towards the optimum (maximum/minimum) outcome [166,167]. The Central Composite Design (CCD) is widely used as a "second-order design" [168].

The level range in CCD is related to the previous design (screening design) performed or they are based on experts in the field that can recommend appropriate values [166]. These define the cube corners, that help estimate the first order effect (main effects and interactions among two factors) [166,167]. The second order (quadratic) effects are estimated by star points [166]. Alpha ( $\alpha$ ) indicates the distance of each star point from the center points [167]. A value greater than unity

indicates that they are positioned outside of the cube as can be seen in **Figure 3-13**. By choosing an  $\alpha > 1$ , the design includes orthogonal blocks and this facilitates in estimating the terms of the model and the blocking separately, which decreases the variance in the regression coefficients as much as possible<sup>[169]</sup>. The error in the CCD is estimated by the center points<sup>[166]</sup>.

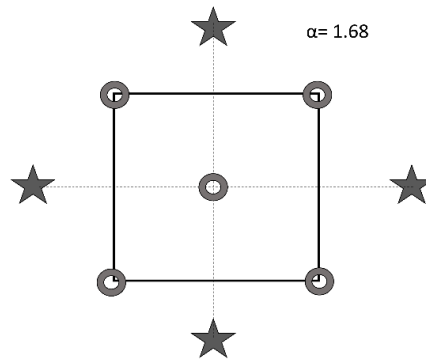


**Figure 3-13:** Central Composite Design cube and star points schematic<sup>[4]</sup>.

In this thesis, a CCD design was selected for four factors with 16 cube points, 12 center points and 12 star points. In total, 40 experiments were performed for two initial microstructure conditions (condition 2 and 3) simultaneously with the same run order. The samples were adjacent next to the thermocouple in the furnace. The alpha value was 1.68, provided from Minitab software default settings. This software was used for both the Taguchi and the Central Composite Design (CCD), analysis of the hardness results and for the CCD to also create the design.

### 3.2.7 Microhardness tests

In Chapters 5-7, a Clark CM-100AT micro-hardness tester (CM10442) equipped with CLEMEX CMT indent measurement software was used. This was a fast way to measure the effect of heat treatment as the response of the experiments and it provided information for future experiments such as compression, torsion or tensile tests for a more comprehensive mechanical

property characterization. Indents were created with a force of 200gf, 15 sec dwell time and measured at a magnification of 500X. The procedure was based on ASTM E384-11<sup>[170]</sup>.

# **Chapter 4 : Microstructural characterization of three different size of gamma prime precipitates in Rene 65**

## **Preface**

The first step in understanding the  $\gamma'$  precipitate characteristics is a thorough microstructural characterisation. In this Chapter the as extruded samples had a trimodal precipitate distribution in the as received condition (no heat treatment), which was ideal to identify compositional differences among them with higher resolution techniques such as Atom Probe Tomography which was the first objective of this thesis. A heat-treated sample was also characterised for comparison.

This chapter is currently published as: C.- M. Katsari, S. Katnagallu and S. Yue, Microstructural characterization of three different size of gamma prime precipitates in Rene 65, Materials Characterization (2020), <https://doi.org/10.1016/j.matchar.2020.110542> <sup>[1]</sup> and according to the Elsevier journal rights as an author, this article can be included in full in this thesis.

## Abstract

Cast and wrought Ni-based superalloy Rene 65 was developed for turbine engine components applications. In the as-extruded condition the alloy presents trimodal distribution of gamma prime ( $\gamma'$ ) precipitates. A detailed microstructural and chemical characterization of the precipitates is presented at a near atomic-scale before and after a softening sub-solvus heat treatment. Scanning and Transmission Electron Microscopy (SEM and TEM) as well as Atom Probe Tomography (APT) were employed to identify the differences in compositions. In the as received condition differences in Cr, Ti and Al content were found between the three precipitate sizes. After a softening sub-solvus heat treatment, the interface between secondary and grown tertiary  $\gamma'$  with the matrix had become chemically homogenized. Lattice mismatch of secondary and tertiary  $\gamma'$  were empirically calculated based on the APT compositions.

**Keywords:** Ni-based superalloys, Rene 65, gamma prime, atom-probe tomography, trimodal precipitation

## 4.1 Introduction

Nickel based superalloys continue to be a part of leading research interests owing to their superior mechanical properties. These alloys are applied in a variety of extreme environments with elevated temperatures and/or high stress. The tailored microstructure of nickel-based superalloys is the key for these applications, as it allows them to operate adequately above 540°C. Rene 65 (R65) is a cast and wrought nickel-based superalloy developed by General Electric and ATI Allvac for turbine engine applications <sup>[1]</sup>. Its microstructure consists of a gamma ( $\gamma$ ) matrix and three sizes of gamma prime ( $\gamma'$ ) precipitates. These precipitates serve as the main strengthening mechanism in this alloy and they are critical for higher creep resistance <sup>[2-3]</sup>. The main advantages of R65 include ease in manufacture of cast ingots (its predecessor is Rene 88DT,

a powder metallurgy alloy) and higher temperature capabilities than the most commonly used Ni-Fe based alloy, Inconel 718. The reason for the latter is that  $\gamma'$  is the only strengthening precipitate present and no phase transformation occurs at operating temperatures. However, the large volume fraction of  $\gamma'$  precipitates (~40%) in the as-forged condition [2] can cause processing difficulties of various parts. Therefore, it is important to understand the effect of this microstructure on the mechanical properties [4].

Traditional terminology for the trimodal precipitate distribution is primary, secondary and tertiary  $\gamma'$  [5-6]. The primary  $\gamma'$  is the largest ( $\mu\text{m}$ ) precipitate, the secondary  $\gamma'$  precipitate is a few hundred nanometers and tertiary  $\gamma'$  precipitate is the smallest, usually a few tens of nanometers. The primary  $\gamma'$  pins the grain boundaries and suppresses the grain growth during the solutionizing treatment, which is beneficial for fatigue resistance [1,6]. Secondary and tertiary  $\gamma'$  nucleate within the grains and typically form at lower temperatures during cooling and aging processes [7-8]. In R65, the size distribution of  $\gamma'$  precipitates evolves during hot processing. Primary  $\gamma'$  forms on the grain boundaries during the early stages (casting and forging) of the industrial process [2]. Primary  $\gamma'$  can also be found at triple junctions in the recrystallized microstructures after forging [9-10]. Secondary and tertiary  $\gamma'$  are in smaller populations usually as intragranular and coherent precipitates, which play a key role in the alloy hardening. Both secondary and tertiary  $\gamma'$  precipitates dissolve partially or fully at the sub-solvus forging temperatures [11] and form again during cooling. The size distribution and morphology of secondary and tertiary precipitates depends on the cooling rate [9,12-18]. According to the literature, it seems that there is no specific size range that could be used as a guide to differentiate the precipitates; the terminology is being used to describe a descending size, nucleating at different temperature ranges [19].

While a morphological description has been established, there are few studies regarding compositional differences between the three sizes of  $\gamma'$  in cast <sup>[20]</sup> and wrought <sup>[21]</sup> nickel-based superalloys compared to powder metallurgy processed superalloys <sup>[16,22-25]</sup>, which also possess a trimodal precipitate distribution. The shear strength of the precipitates depends on their chemical composition <sup>[26]</sup>. Chemistry of these precipitates also relates to various defect energies, such as those for the intrinsic superlattice stacking faults (the most common planar defects in L1<sub>2</sub> phases), for extrinsic superlattice stacking faults and for the anti-phase boundaries <sup>[26]</sup>. The precipitates are usually referred to as Ni<sub>3</sub>Al or Ni<sub>3</sub>(Al,Ti), since these are the equilibrium precipitates of binary (or ternary) alloys. For more complicated systems it is expected that the chemical compositions of the precipitates will be more complex; a complete knowledge of these compositions will help to decipher their formation mechanisms and their effect on mechanical properties. To the best of our knowledge, no compositional differences have been reported between the three- $\gamma'$  precipitates in R65 <sup>[4-5,8,18]</sup>. Here we give a detailed precipitate microstructural characterization of this alloy. The compositional and morphological changes in the precipitates before and after a softening heat treatment is also discussed.

## 4.2 Experimental procedure

All the specimens for characterization were taken from cylindrical as-extruded samples of Rene 65 with dimensions of 9 x Ø 6 (± 0.1) mm. The samples were provided by GE Aviation. The nominal composition of the alloy can be seen in Table 4-1:

**Table 4-1:** Nominal chemical composition of Rene 65 <sup>[1]</sup>

Element	Ni	Fe	Co	Cr	Mo	W	Al	Ti	Nb	B	C	Zr
wt. %	55.42	1.0	13.0	16.0	4.0	4.0	2.1	3.7	0.7	0.016	0.015	0.05
at. %	54.95	1.04	12.84	17.91	2.43	1.27	4.53	4.5	0.44	0.09	0.073	0.03

An SU8230 Field Emission scanning electron microscope (SEM) coupled with energy dispersive spectroscopy (EDS) was used for compositional analysis of primary and secondary  $\gamma'$  with accelerating voltage of 3kV for imaging and 10kV for compositional analysis at magnifications up to x80,000. It is worth mentioning that the imaging of tertiary  $\gamma'$  precipitates was challenging, due to their smaller size, and their chemical composition could not be evaluated by EDS due to the much larger interaction volume ( $\sim 250$  nm) (as predicted from a CASINO <sup>[27]</sup> simulation) compared with the actual precipitate size (tens of nm).

Bruker software was used for the analysis of the EDS spectra. For higher magnifications and to obtain diffraction information, a FEI Tecnai G2 F20 Cryo-scanning transmission electron microscope (STEM) was used.

For the characterization in SEM, the samples were metallographically prepared to a final polishing step of 0.05  $\mu\text{m}$  using colloidal silica. Imaging in back scattered electron (BSE) mode in SEM does not require etching of the samples since differences in atomic number will appear as variations in intensity, with the phases containing the heavier elements appearing brighter <sup>[28]</sup>.

For transmission electron microscope (TEM) samples, mechanical grinding followed by jet polishing of 3mm disks with 10% vol. perchloric acid in methanol solution at  $-30^\circ\text{C}$  (cooled by liquid nitrogen) was used. The image analysis for quantifying microstructural features was done using ImageJ software where  $\sim 50$  precipitates (where available) were manually measured in their X and Y axes and their average values are presented in the form Xnm x Ynm .

In situ site-specific specimen preparation for atom probe tomography (APT) by Plasma Focused Ion Beam (PFIB) (Thermofisher Helios) was performed according to protocols described in <sup>[29]</sup>. Local electrode atom probe (LEAP) 3000XR and 5000HR were used to evaluate the chemical compositions and variations.

For empirical calculation of the  $\gamma$  and  $\gamma'$  lattice parameters, a program called “Program MAP\_NICKEL\_LATTICE” [30] based on a neural network [31-32] developed at Cambridge University was used. The program requires the chemical composition and the temperature in °C as inputs. For the chemical composition of the precipitates and the matrix, compositions measured from EDS and APT were used. The C and B compositions could not be included due to the limitations of the program.

A heat-treated sample was also characterised for a comparison with the as received samples. The heat treatment included a sub-solvus annealing at 1095°C for 30 min followed by furnace cooling to 954°C and then holding at that temperature for 10min and finally air cooling to the room temperature. This softening heat treatment was used in previous work on the same, as extruded, sample and showed a trimodal distribution of the precipitates and a lower hardness than the as received sample [33].

### **4.3 Results and Discussion**

The SEM micrographs of the as received sample show primary  $\gamma'$  at a low magnification in Fig.4-1a (example precipitates circled in yellow) on the grain boundaries. At higher magnifications (x 80,000) examples of secondary (red arrows) and tertiary  $\gamma'$  (circled in red) can be observed inside the grains (Fig.4-1b).

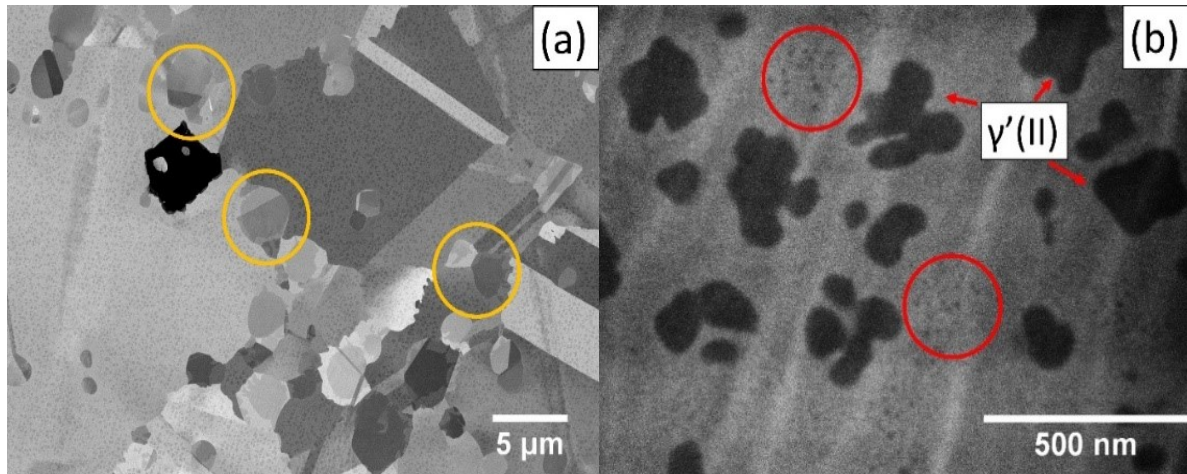


**Figure 4-1:**As received sample (a) low magnification as received condition, primary  $\gamma'$  circled in yellow (b) high magnification of the as received condition, secondary  $\gamma'$  examples indicated with red arrows and tertiary  $\gamma'$  examples are circled in red.

Point analysis and EDS mapping (Fig.4-2) were acquired to determine the preliminary chemical compositions of the different precipitates. The point analyses on the matrix, primary and secondary  $\gamma'$  are tabulated in Table 4-2:

**Table 4-2:** Point & ID analysis of the as received sample (in at. %).

(in at. %)	Ni	Cr	Co	Mo	W	Fe	Nb	C	Ti	Al
<b>matrix</b>	44.61	24.94	11.84	5.14	5.12	2.19	0.84	0.68	2.82	1.8
<b>Primary</b>	64.06	3.57	7.64	0.49	2.25	0.99	1.56	0.39	13.58	5.47
$\gamma'$										
<b>Secondary</b>	55.32	11.81	8.91	3.55	4.32	0.93	1.25	1.01	8.79	4.09
$\gamma'$										

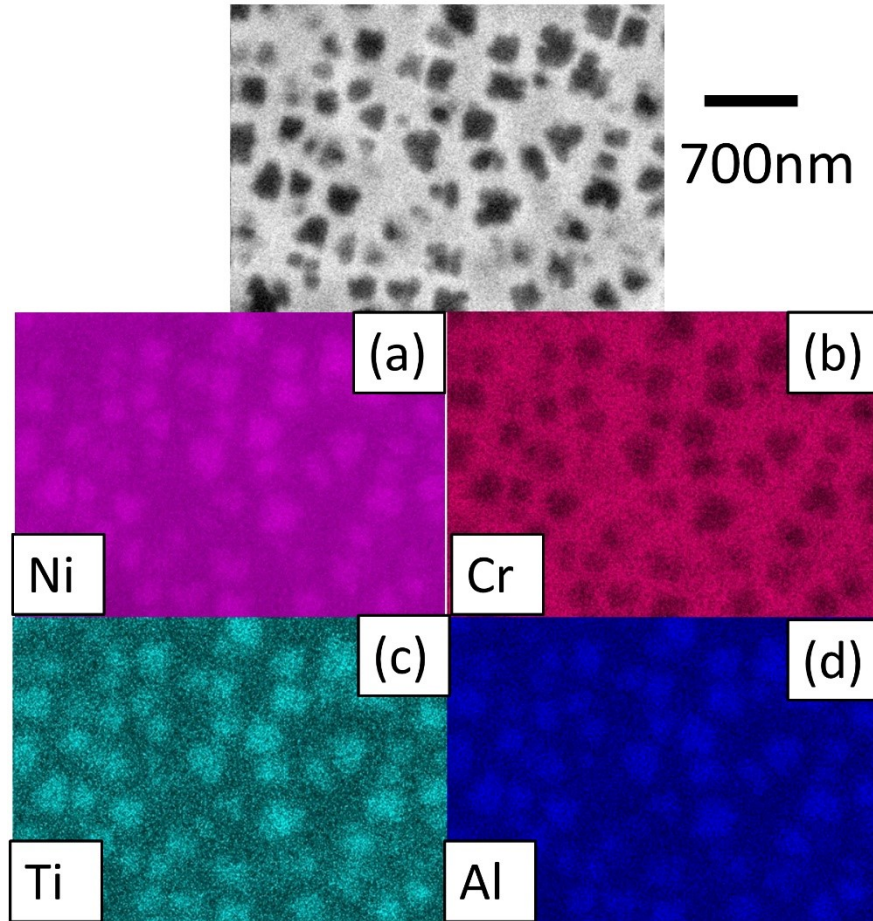


**Figure 4-2:** EDS mapping of the as received sample highlighting differences in composition between secondary  $\gamma'$  precipitates and the matrix (a)Ni (b)Cr (c)Ti (d) Al.

A clear difference in the  $\gamma'$  forming elements (Ni,Al,Ti) between the matrix and the precipitates, and also amongst the precipitates (primary and secondary  $\gamma'$ ) themselves is evident. Both Ti and Al are in the primary  $\gamma'$  at higher atomic fractions in contrast to the secondary  $\gamma'$  and the matrix. Furthermore, Cr and Mo tend to partition more in the matrix, whereas in the precipitates they prefer the secondary  $\gamma'$  to the primary  $\gamma'$ . From EDS, the tertiary  $\gamma'$  composition could not be measured due to the interaction volume of the electrons being larger than the precipitates.

The microstructure of the heat-treated sample revealed fewer tertiary  $\gamma'$  precipitates close to primary  $\gamma'$  (Fig.4-3), with a size ranging from 40-90 nm. The secondary  $\gamma'$  average size was  $172 \pm 27.1$  nm with a round edge cuboidal morphology.

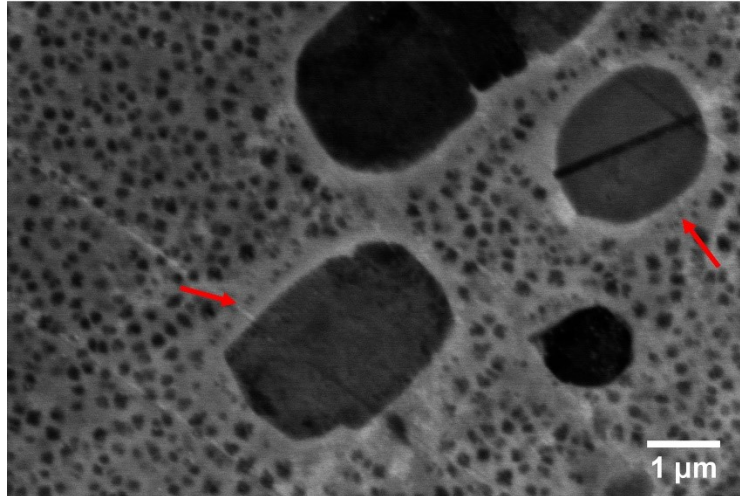


**Figure 4-3:** SEM micrograph of the heat-treated sample. Red arrows indicate positions of tertiary  $\gamma'$ .

The as-received sample was further analysed in TEM. Imaging the secondary and clusters of tertiary  $\gamma'$  was feasible under bright-field conditions in the TEM. Using point analysis by EDS, it was confirmed from the intensities of the peaks that the phases present were indeed  $\gamma'$  precipitates (higher Al, Ti than the matrix). The secondary  $\gamma'$  morphology is irregular (Fig. 4-4) with an average size of  $210.24 \pm 48 \text{ nm} \times 189.55 \pm 38 \text{ nm}$  and average aspect ratio of  $0.8 \pm 0.1$ .

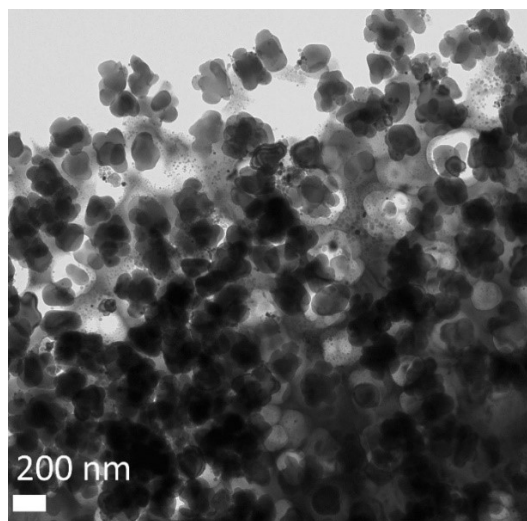


**Figure 4-4:** TEM bright field image indicating secondary  $\gamma'$  morphology of the as received sample.

The tertiary  $\gamma'$  precipitates were observed both in clusters (Fig.4-5a) and randomly distributed within the matrix (Fig.4-6) with average size of  $10.91 \pm 5$  nm by  $10.62 \pm 4.1$  nm and aspect ratio of  $0.9 \pm 0.1$ , indicating a spherical morphology.

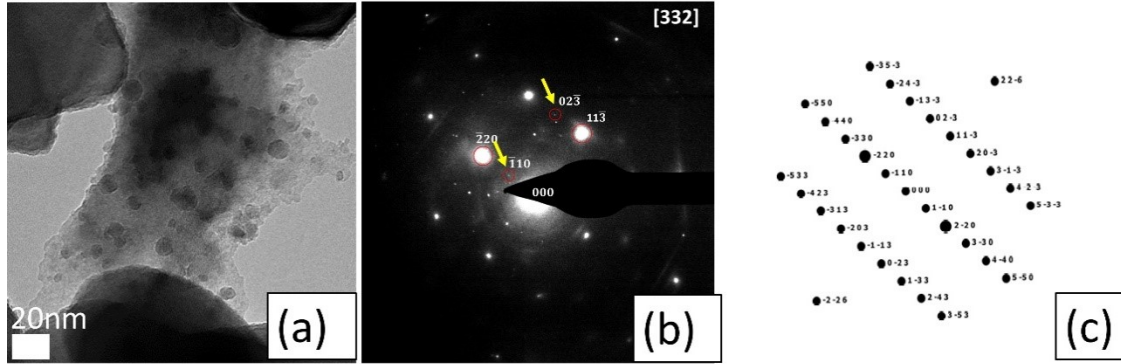


**Figure 4-5:** a) Tertiary  $\gamma'$  clusters in  $\gamma$  matrix b) Diffraction pattern of site 5a, arrows highlighting superlattice reflections c) simulated diffraction pattern by PDF-4 database.

Diffraction revealed  $L1_2$  superlattice reflections of  $\gamma'$  precipitates with  $[332]$  zone axis (Fig.4-5 b, c). Using Inverse Fast Fourier Transformation (IFFT) on the high resolution TEM images (Fig.4-6 b, c), the interplanar distance was measured on average as  $d_m = 2.127 \text{ \AA}$  and  $d_p = 2.127 \text{ \AA}$ , where  $d_m$  and  $d_p$  are the interplanar distances of the matrix and precipitate respectively; therefore the mismatch is 0. The mismatch was calculated based on the formula  $\delta = (d_m - d_p) / d_m$ . It is worth mentioning that  $d_m$  and  $d_p$  were measured in various regions within the matrix and the precipitates, respectively, and do not take into account some dislocations that were observed in some cases (Fig.4-6 d). In the area around the dislocations (Fig. 4-6 c, d) the mismatch was found to be in the range of 0.6%-0.8%, indicating a cuboidal morphology.

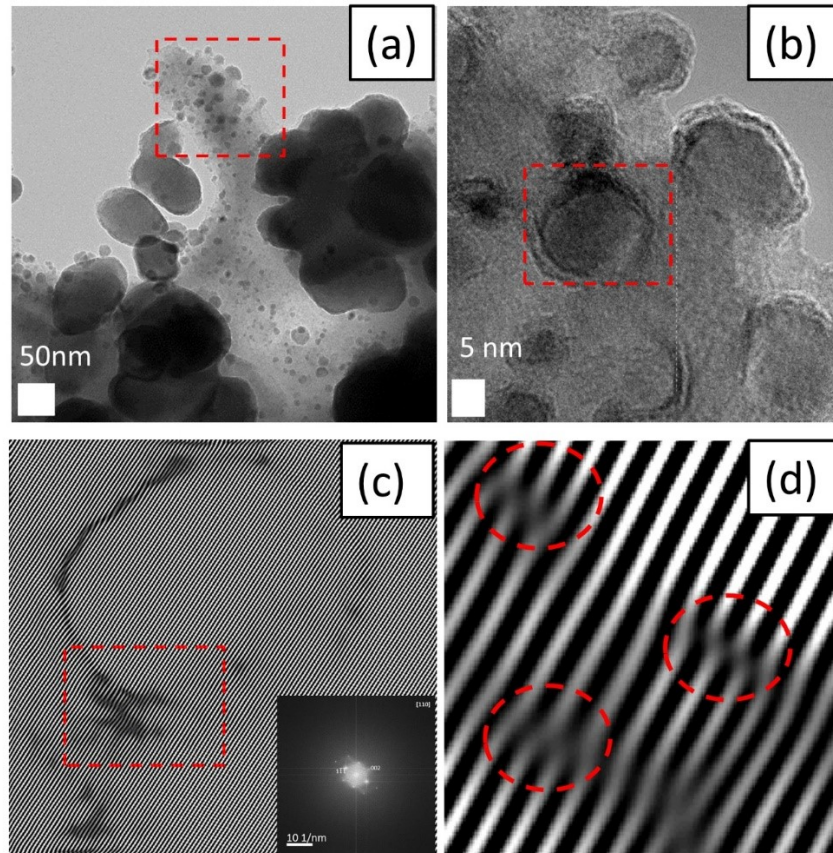


**Figure 4-6:** a) tertiary  $\gamma'$  homogeneous distribution within the matrix b) HRTEM of 6a marked area highlighting tertiary  $\gamma'$  c) IFFT on marked precipitate d) high magnification of marked 6c area highlighting dislocations on the interface.

APT was done for an accurate evaluation of the compositions in the observed precipitates. In Figure 4-7(a), the 3D reconstruction of the as received R65 shows two distinct sizes in tertiary  $\gamma'$  precipitates. A 1D compositional profile is shown in Figure 4-7 (b) which shows that the tertiary  $\gamma'$  precipitate has higher amount of Al than Ti. The smaller tertiary  $\gamma'$  precipitates show higher content of  $\gamma$  matrix elements, such as Mo, Cr and Co, than the large tertiary  $\gamma'$  precipitates (Table 4-3). This indicates they might have formed at a further lower temperature, which limits the outward diffusion of the  $\gamma$  matrix elements. Another possible explanation is that they are tertiary  $\gamma'$  precipitates that have not formed completely. To separate them, we call those smaller tertiary  $\gamma'$  precipitates quaternary  $\gamma'$ .

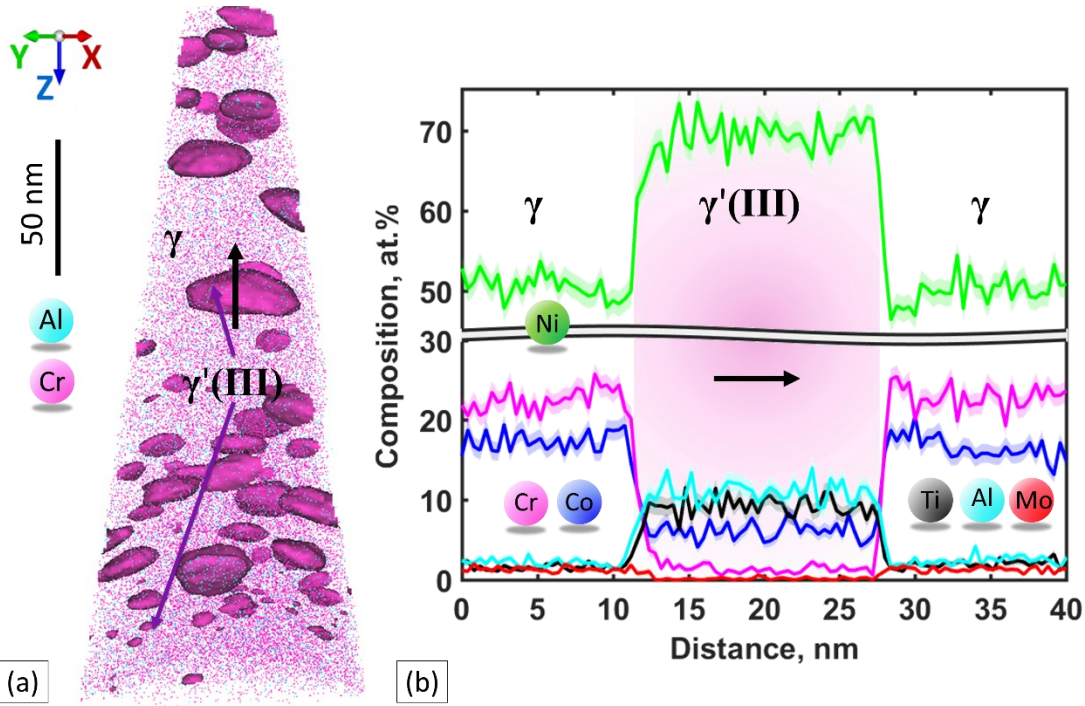


**Figure 4-7:** (a) 3D reconstructed volume of the as received tertiary  $\gamma'$  precipitates, highlighted by 13 at.% Cr iso-composition surfaces, in the  $\gamma$  matrix. The two distinct sizes of tertiary large and small (quaternary) precipitates are indicated by the purple arrows. (b) A 1D compositional profile along the tertiary  $\gamma'$  in  $\gamma$  matrix.

In Table 4-3 the average compositions of secondary and tertiary  $\gamma'$  (averaged from large and small tertiary  $\gamma'$  precipitates) are presented. As expected, since the tertiary  $\gamma'$  precipitates form at a lower temperature, they are rich in  $\gamma$  partitioning elements, such as Cr, Mo and Co, compared to the secondary  $\gamma'$ . Another key difference is the higher Al content than the Ti in the tertiary precipitates. In contrast, the secondary  $\gamma'$  show higher Ti content.

**Table 4-3:** APT compositions of the matrix, the secondary and the tertiary  $\gamma'$  precipitates in the as received sample.

<b>As received</b> <b>(at.%)</b>	<b>Ni</b>	<b>Al</b>	<b>Cr</b>	<b>Ti</b>	<b>W</b>	<b>Mo</b>	<b>Co</b>	<b>Fe</b>	<b>Nb</b>
<b>Matrix</b>	51.10	2.43	23.70	2.16	1.02	2.71	14.41	1.21	0.15
<b>Secondary <math>\gamma'</math></b>	68.45	9.46	1.49	10.9	0.55	0.88	6.69	0.2	0.44
<b>Tertiary <math>\gamma'</math></b>	63.43	11.2	3.22	8.08	1.09	1.81	6.79	0.3	0.60
<b>Large tertiary <math>\gamma'</math></b>	67.21	11.06	2.54	8.10	0.968	1.51	6.61	0.25	0.58
<b>Small tertiary <math>\gamma'</math>(quaternary)</b>	63.43	11.34	3.89	8.05	1.22	2.10	6.97	0.35	0.628

**Table 4-4:** APT compositions of the matrix and the secondary  $\gamma'$  precipitates after heat treatment.

<b>Heat treated</b> <b>(at.%)</b>	<b>Ni</b>	<b>Al</b>	<b>Cr</b>	<b>Ti</b>	<b>W</b>	<b>Mo</b>	<b>Co</b>	<b>Fe</b>	<b>Nb</b>
<b>Matrix</b>	48.65	2.88	23.24	2.72	1.26	3.02	15.7	1.24	0.22
<b>Secondary <math>\gamma'</math></b>	67.26	9.94	1.55	12.03	0.61	0.64	5.63	0.22	0.69

Using the composition of the primary  $\gamma'$  from SEM-EDS and the compositions of the matrix, secondary and tertiary  $\gamma'$  from the APT, the lattice parameters at room temperature were calculated. The same procedure was followed for the heat treated sample. This was done using the MAP\_NICKEL\_LATTICE program.

**Table 4-5:** Lattice parameters of matrix and precipitates for as received and heat treated conditions.

<b>Lattice parameters (Å)</b>									
<b>Condition</b>	Temperature (°C)	Primary $\gamma'$	error	Secondary $\gamma'$	error	Tertiary $\gamma'$	error	matrix	error
<b>As received</b>	25	3.566	0.0345	3.5838	0.0064	3.5829	0.0067	3.5521	0.0107
<b>Heat treated</b>	25	-	-	3.5859	0.018	-	-	3.5526	0.0117

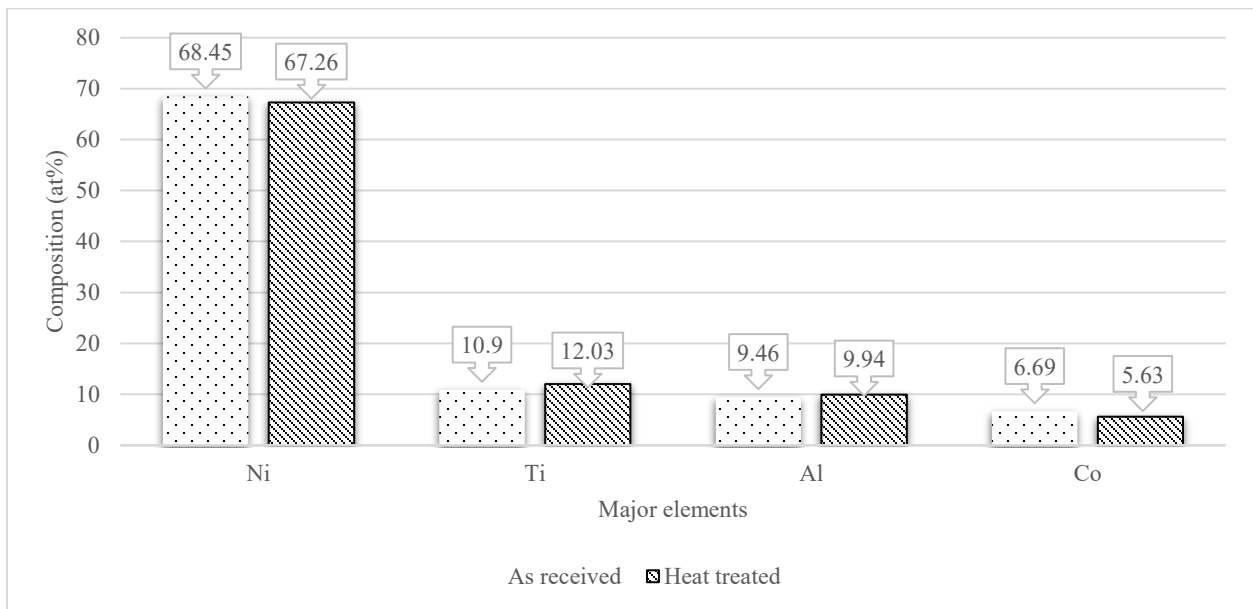
In the literature <sup>[34]</sup>, the lattice parameter of pure Ni<sub>3</sub>Al is reported to be 3.561 Å and can reach 3.568 Å for Ni<sub>3</sub>(Al<sub>0.5</sub>Ti<sub>0.5</sub>). In another reference <sup>[35]</sup>, pure Ni<sub>3</sub>Al was calculated with X-Ray Diffraction at various temperatures and Al at% compositions ranging from 3.555- 3.5674 Å. In similar alloys, such as RR1000, before ageing, the constrained  $\gamma'$  lattice parameter was found to be  $3.5981 \pm 0.0008$  Å <sup>[36]</sup>. In R88DT, secondary  $\gamma'$  was reported as 3.5917 Å and tertiary as 3.5923 Å <sup>[37]</sup>, which are higher than the empirical lattice parameters. From the calculated lattice parameters ( $\alpha_{\gamma'}$  and  $\alpha_{\gamma}$  for precipitates and matrix respectively), the lattice mismatch ( $\delta$ ) can be evaluated using  $\delta = (\alpha_{\gamma'} - \alpha_{\gamma}) / 0.5(\alpha_{\gamma'} + \alpha_{\gamma})$ . In this work, the calculated mismatch between secondary  $\gamma'$  and the matrix is 0.89%. The calculated mismatch between tertiary  $\gamma'$  and the matrix is 0.86 %. The lattice mismatch is higher for the secondary  $\gamma'$  precipitate. It is worth mentioning that the calculated mismatch of tertiary  $\gamma'$  differs greatly from the average experimental values- not the particular precipitate in Fig.4-6c that revealed a cuboidal edge (0.6%-0.8%). The TEM interplanar distance revealed a mismatch of approximate 0, indicating an almost spherical precipitate, whereas the empirical calculation indicates a more cuboidal shape, which matches the description for

secondary  $\gamma'$  precipitates but not for the tertiary  $\gamma'$  precipitates. This is reasonable considering that the database of the MAP\_LATTICE\_SIMULATION alloy database was created taking into consideration alloys with monomodal distribution and cuboidal precipitate morphologies, which is not the case for Rene 65. Furthermore, the database is based on bulk materials, so the calculated lattice mismatch is constrained.

As the percentage of Ti increases, the lattice parameter increases [35]. From the APT measurements, the secondary  $\gamma'$  has higher Ti than tertiary  $\gamma'$  and thus has a larger lattice parameter. In [38], a model Ni-base superalloy within the compositional range of RR1000 had higher Al than Ti in secondary  $\gamma'$ , which is not in agreement with the observations of this work. In [16], secondary  $\gamma'$  in Rene 88 DT, the predecessor of Rene 65, had higher Ti than Al, which agrees with our results, but only in the fast cooled samples of that work, whereas the opposite (higher Al than Ti) appeared in the slow cooled samples. In [38] and [36], in the model alloy and RR1000 respectively, tertiary  $\gamma'$  had higher Al than Ti before and after an aging heat treatment, which agrees with our observations. It seems that all  $\gamma'$  begin to nucleate as spheres and then, depending on the lattice misfit and, therefore, coherency, they change their morphology. This morphological development of  $\gamma'$  precipitates proceeds in the sequence: spheres-cuboids-cuboidal arrays-dendrites, and the growth is, at least partially, diffusion controlled [39-40]. According to Ricks et al [40], the size at which the first two transitions are accomplished is a function of the magnitude of the lattice misfit in the alloy, since the morphology is initially determined by coherency strain. Therefore, secondary  $\gamma'$  has a higher possibility to complete the transition than tertiary  $\gamma'$ . The growth sequence may be interrupted if there are sufficiently high  $\gamma'$  nucleation densities that could cause overlap of the diffusion fields, which is the case of tertiary  $\gamma'$ ; that is why their size remains small and their shape almost spherical. As mentioned above, the higher the Ti content the higher

the lattice mismatch, which is the case of secondary  $\gamma'$  that does not have a spherical morphology. In the case of tertiary  $\gamma'$ , on average, the precipitates have an almost spherical shape as observed from TEM imaging and their composition suggests that, with less Ti than Al, their lattice is smaller and therefore more coherent than secondary. During nucleation and growth of the different populations, the diffusion of  $\gamma'$  forming elements will significantly impact the final morphology which, is the reason that, in other studies, different cooling rates would lead to different diffusion of elements.

In Figure 4-8 the compositions measured from APT of the secondary  $\gamma'$  from both the as received and the heat-treated are shown for comparison.



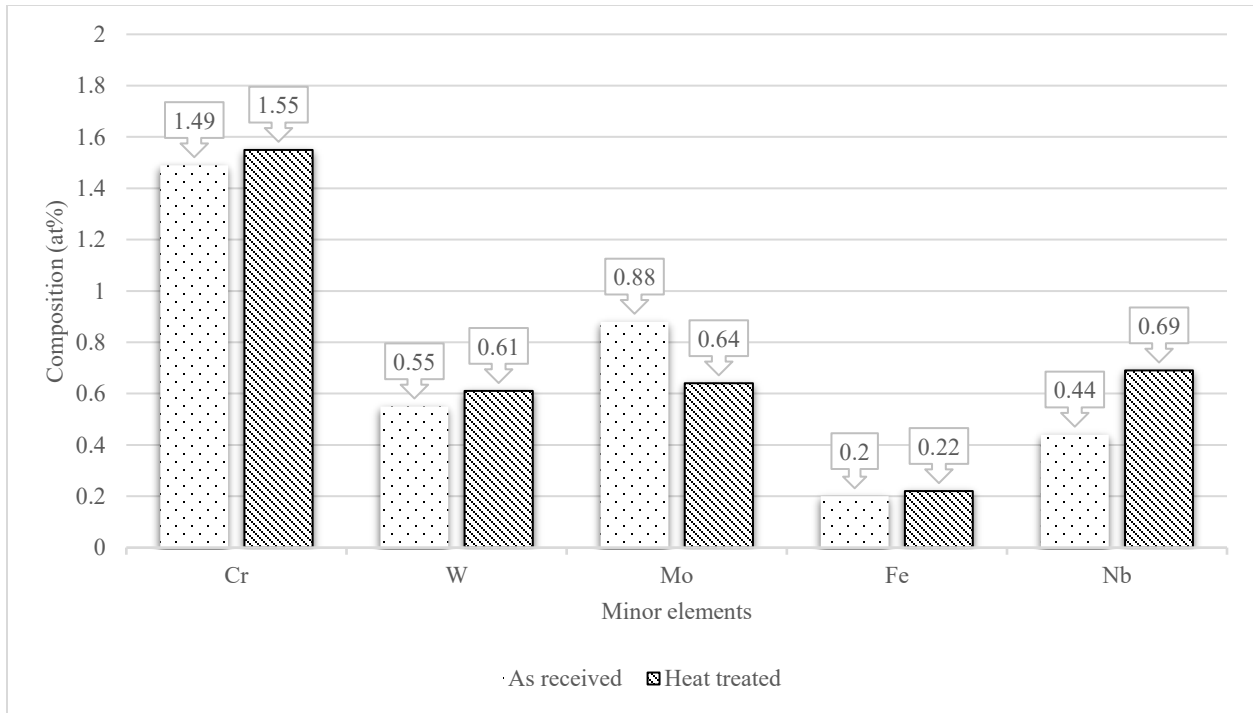


**Figure 4-8:** Comparison of the compositions of major(top) and minor (bottom) alloying elements between the as received and heat-treated state.

The secondary  $\gamma'$  does not seem to change significantly in composition between the two conditions. However, the Ti content has increased and Co content has decreased. The heat-treatment allowed the Co to partition to the matrix and Ti to the precipitate. Apart from that, the interface between the secondary  $\gamma'$  and the matrix appears to be chemically homogeneous. In the as-received state, as seen in Figure 4-9 (b) and (c), the 1D concentration profile shows a higher Al content than Ti (~10.9 at.%) in the precipitate near the interface. However, after heat-treatment, as shown in Figure 4-10 (b), near the interface in the precipitate, the Ti content is higher and appears to be same as the precipitate interior. This is also seen in the precipitate's composition, which shows higher Ti (~12.03 at.%) after heat-treatment.

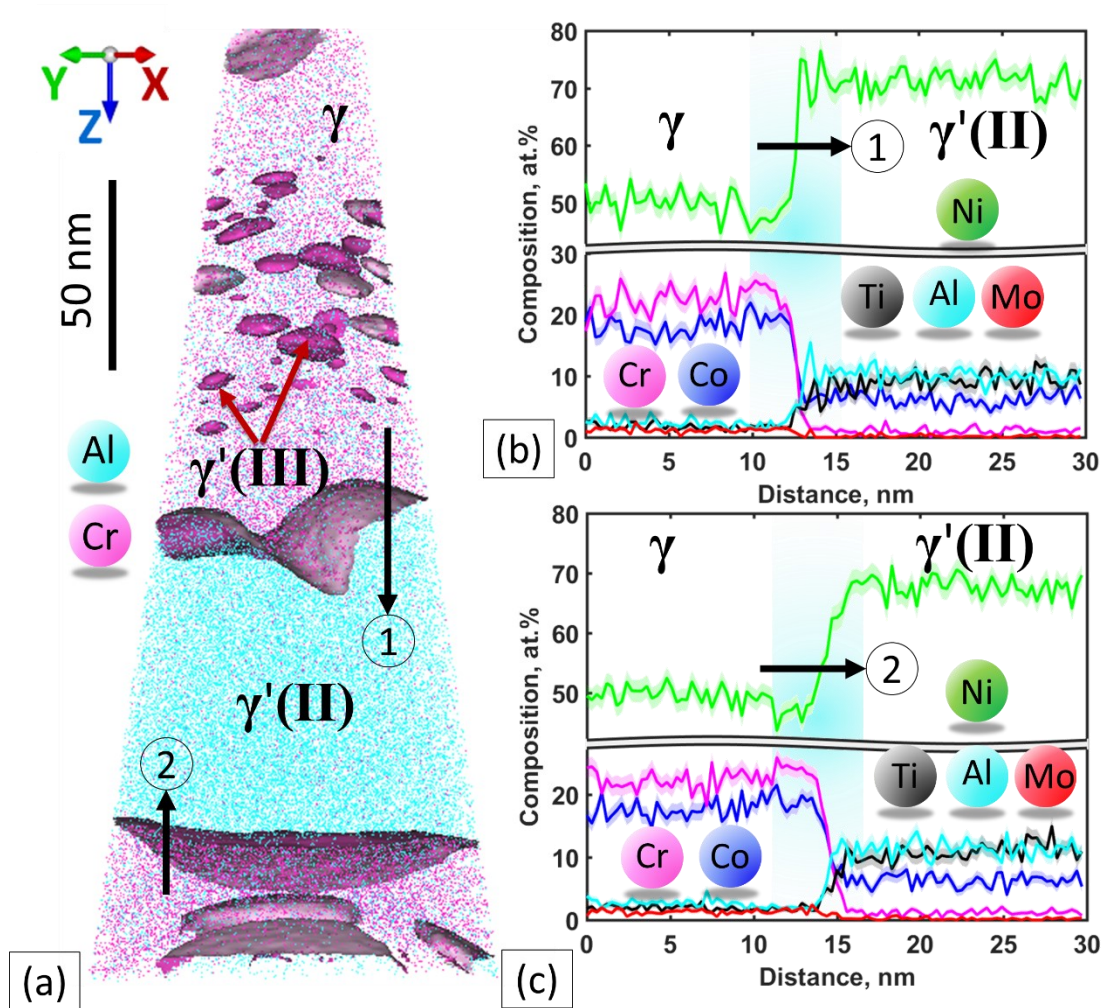


**Figure 4-9 :** (a) APT 3D reconstruction of as received sample showing secondary and tertiary precipitates highlighted by 13 at.% Cr iso-composition surface. (b) & (c) show 1D concentration profiles along the two interfaces between the matrix and secondary precipitate.

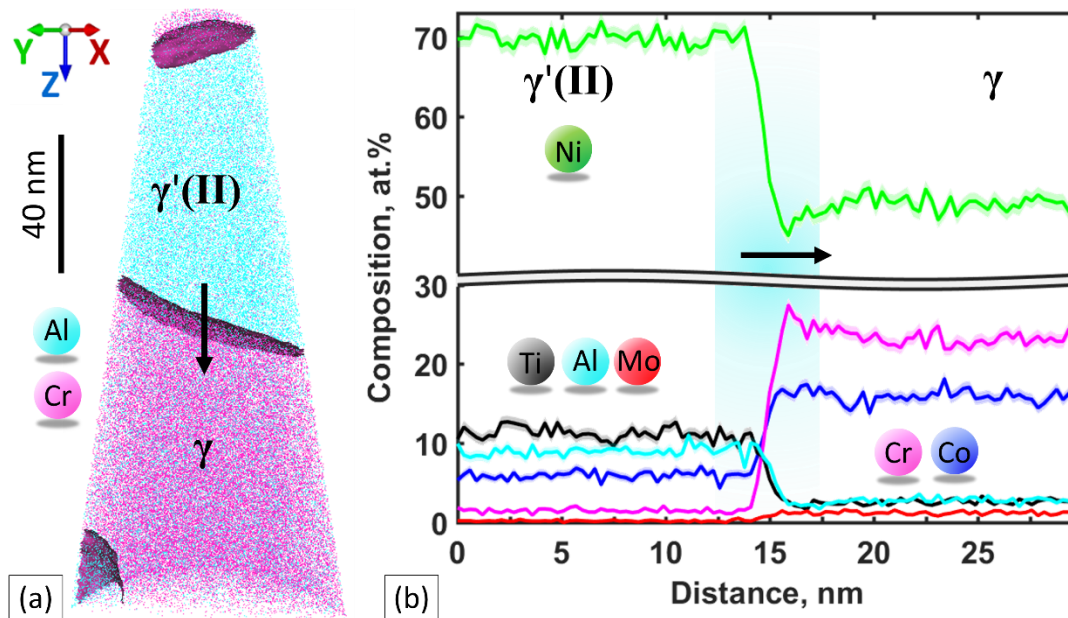


**Figure 4-10:** (a) APT 3D reconstructed volume of the heat treated sample showing only secondary precipitates highlighted by 13 at.% Cr iso-composition surface. (b) 1D concentration profile along the interface between the matrix and the secondary precipitate.

#### 4.4 Conclusions

In this paper, extruded R65 samples were studied in the as-received condition and after a softening heat treatment. The samples were microstructurally characterised to identify morphological and compositional differences between the precipitates. The findings can be summarized as follows:

- In the as received sample, the three traditional size distributions of the precipitates were observed with tertiary  $\gamma'$  present in clusters within the grains. The secondary  $\gamma'$  morphology is irregular with an average size of  $210.24 \pm 48$  nm X  $189.55 \pm 38$  nm and average aspect ratio of  $0.8 \pm 0.1$ . Tertiary  $\gamma'$  size was measured with TEM bright field images and had an average size of  $10.91 \pm 5$  nm by  $10.62 \pm 4.1$  nm and aspect ratio of  $0.9 \pm 0.1$ , which describes an almost spherical morphology.

- A further smaller size distribution of  $\gamma'$  precipitates was also observed. These small tertiary  $\gamma'$  precipitates (quaternary  $\gamma'$ ) were richer in  $\gamma$  forming elements Cr, Mo and Co than their larger counterparts. Hence indicating a lower formation temperature.
- SEM-EDS and APT were employed for this alloy to identify compositional differences in the intragranular precipitates. Primary and secondary  $\gamma'$  have higher Ti than Al percentage [Ni<sub>3</sub>(Ti,Al)] whereas tertiary  $\gamma'$  has higher Al [Ni<sub>3</sub>(Al,Ti)] in the as received condition.
- Lattice parameters and mismatch between the matrix and the precipitates of the as received and the heat treated sample were empirically calculated based on the experimental chemical composition. Higher Ti content in secondary  $\gamma'$  increases the lattice parameter and therefore there is a higher mismatch (0.89%) with the matrix compared to tertiary  $\gamma'$ .
- After the heat treatment, the composition of secondary  $\gamma'$  (and/or grown tertiary  $\gamma'$ ) had not changed significantly. However, the Ti content increased to 12 at.% from 10.9 at.% and a homogenous interface between the matrix and the precipitate is developed.

#### 4.5 Acknowledgements

Financial support from the Natural Science and Engineering Council of Canada, GE Aviation, Bromont, Quebec Canada, the Consortium de Recherche et D'innovation en Transformation Métallique, the McGill Engineering Doctoral Award (to C.M Katsari) and the Graduate Mobility Award (to C.M. Katsari) is gratefully acknowledged. We appreciate GE Aviation, Bromont for providing us with samples as well as useful discussions with Dr. Andrew Wessman and Mr. Martin Therer. We thank Mr. Nicolas Brodusch from McGill Electron Microscopy Research Group and Mr. David Liu at the Facility for Electron Microscopy Research of McGill University for help in microscope operation and data collection. We appreciate the

hospitality of Dr. Baptiste Gault's group in the Max Planck Institute for Iron Research in Germany, where the APT experiments were conducted.

#### **4.6 Bibliography**

- [1] J. A. Heaney, M. L. Lasonde, A. M. Powell, B. J. Bond, C. M. O'Brien, Development of a New Cast and Wrought Alloy (René 65) for High Temperature Disk Applications, in: 2014: pp. 67–77. <https://doi.org/10.1002/9781119016854.ch6>.
- [2] J. Groh, T. Gabb, R. Helmink, A. Wusatowska-Sarnek, René 65 billet material for forged turbine components, in: Proc. 8th Int. Symp. Superalloy 718 Deriv., John Wiley & Sons, 2014: p. 107.
- [3] A. Laurence, J. Cormier, P. Villechaise, T. Billot, J.-M. Franchet, F. Pettinari-Sturmel, M. Hantcherli, F. Momprou, A. Wessman, Impact of the solution cooling rate and of thermal aging on the creep properties of the new cast wrought Rene 65 Ni-based superalloy, in: 8th Int. Symp. Superalloy 718 Deriv. 2014, Sept. 28, 2014 - Oct. 1, 2014, John Wiley and Sons Inc., Institut Pprime, Physics and Mechanics of Materials Department, ISAE-ENSMA, 1 avenue Clement Ader, Futuroscope - Chasseneuil; 86961, FranceSnecma-Safran Group, Technical Department, 171 boulevard de Valmy - BP 31, Colombes Cedex; 92702, FranceSafran SA, M, 2014: pp. 333–348.
- [4] O.R. Terrazas, M.E. Zaun, R.S. Minisandram, M.L. Lasonde, Influence of temperature and strain rate during rolling of rene 65 bar, in: 9th Int. Symp. Superalloy 718 Deriv. Energy, Aerospace, Ind. Appl. June 3, 2018 - June 6, 2018, Springer International Publishing, ATI Specialty Materials, 4374 Lancaster Highway, Richburg; SC; 29729, United StatesATI Specialty Materials, 2020 Ashcraft Avenue, Monroe; NC; 28110, United StatesWilmot; NH; 28110, United States, 2018: pp. 977–986. [https://doi.org/10.1007/978-3-319-89480-5\\_65](https://doi.org/10.1007/978-3-319-89480-5_65).

- [5] T. Wojcik, M. Rath, E. Kozeschnik, Characterisation of secondary phases in Ni-base superalloy Rene 65, *Mater. Sci. Technol.* 34 (2018) 1558–1564. <https://doi.org/10.1080/02670836.2018.1505227>.
- [6] R.C. Reed, *The superalloys: fundamentals and applications*, Cambridge university press, 2008.
- [7] A. Wessman, A. Laurence, J. Cormier, P. Villechaise, T. Billot, J.-M. Franchet, Thermal stability of cast and wrought alloy Rene 65, in: 13th Int. Symp. Superalloys, SUPERALLOYS 2016, Sept. 11, 2016 - Sept. 15, 2016, Minerals, Metals and Materials Society, GE Aviation, One Neumann Way, Cincinnati; OH; 45215, United States Institut Pprime, UPR CNRS 3346, CNRS, Universite de Poitiers - ENSMA, Physics and Mechanics of Materials Department, ISAE-ENSMA, 1 avenue Clement Ader, Futuroscope - Chasseneuil; 86961, Fra, 2016: pp. 793–800.
- [8] A.E. Wessman, *Physical Metallurgy of Rene 65, a Next-Generation Cast and Wrought Nickel Superalloy for use in Aero Engine Components*, University of Cincinnati, 2016.
- [9] R.A. Ricks, A.J. Porter, R.C. Ecob, The growth of  $\gamma'$  precipitates in nickel-base superalloys, *Acta Metall.* 31 (1983) 43–53.
- [10] A.J. Porter, B. Ralph, Recrystallization of a nickel-base superalloy: Kinetics and microstructural development, *Mater. Sci. Eng.* 59 (1983) 69–78. [https://doi.org/https://doi.org/10.1016/0025-5416\(83\)90089-7](https://doi.org/https://doi.org/10.1016/0025-5416(83)90089-7).
- [11] J. V Bee, A.R. Jones, P.R. Howell, The interaction of recrystallizing interfaces with intragranular precipitate dispersions in a nickel-base superalloy, *J. Mater. Sci.* 16 (1981) 1471–1476. <https://doi.org/10.1007/bf02396865>.
- [12] R.J. Mitchell, M. Preuss, S. Tin, M.C. Hardy, S. Tin, M.C. Hardy, The influence of cooling rate from temperatures above the  $\gamma'$  solvus on morphology, mismatch and hardness in advanced

polycrystalline nickel-base superalloys, *Mater. Sci. Eng. A.* 473 (2008) 158–165.  
<https://doi.org/https://doi.org/10.1016/j.msea.2007.04.098>.

[13] P.M. Sarosi, B. Wang, J.P. Simmons, Y. Wang, M.J. Mills, Formation of multimodal size distributions of  $\gamma'$  in a nickel-base superalloy during interrupted continuous cooling, *Scr. Mater.* 57 (2007) 767–770.

[14] J. Tiley, G.B. Viswanathan, R. Srinivasan, R. Banerjee, D.M. Dimiduk, H.L. Fraser, Coarsening kinetics of  $\gamma'$  precipitates in the commercial nickel base Superalloy René 88 DT, *Acta Mater.* 57 (2009) 2538–2549. <https://doi.org/https://doi.org/10.1016/j.actamat.2009.02.010>.

[15] A.R.P. Singh, S. Nag, S. Chattopadhyay, Y. Ren, J. Tiley, G.B. Viswanathan, H.L. Fraser, R. Banerjee, Mechanisms related to different generations of  $\gamma'$  precipitation during continuous cooling of a nickel base superalloy, *Acta Mater.* 61 (2013) 280–293.  
<https://doi.org/https://doi.org/10.1016/j.actamat.2012.09.058>.

[16] A.R.P. Singh, S. Nag, J.Y. Hwang, G.B. Viswanathan, J. Tiley, R. Srinivasan, H.L. Fraser, R. Banerjee, Influence of cooling rate on the development of multiple generations of  $\gamma'$  precipitates in a commercial nickel base superalloy, *Mater. Charact.* 62 (2011) 878–886.  
<https://doi.org/https://doi.org/10.1016/j.matchar.2011.06.002>.

[17] M. Fahrman, A. Suzuki, Effect of cooling rate on Gleeble hot ductility of UDIMET alloy 720 billet, in: 12th Symp. Superalloys, Superalloys, 2008: pp. 311–316.

[18] M.-A. Charpagne, T. Billot, J.-M. Franchet, N. Bozzolo, Heteroepitaxial recrystallization: A new mechanism discovered in a polycrystalline  $\gamma$ - $\gamma'$  nickel based superalloy, *J. Alloys Compd.* 688 (2016) 685–694. <https://doi.org/https://doi.org/10.1016/j.jallcom.2016.07.240>.

- [19] T.M. Pollock, S. Tin, Nickel-Based Superalloys for Advanced Turbine Engines: Chemistry, Microstructure and Properties, *J. Propuls. Power.* 22 (2006) 361–374. <https://doi.org/10.2514/1.18239>.
- [20] K.M. Delargy, G.D.W. Smith, Phase composition and phase stability of a high-chromium nickel-based superalloy, IN939, *Metall. Trans. A.* 14 (1983) 1771–1783. <https://doi.org/10.1007/bf02645547>.
- [21] L. Pichon, J.-B. Dubois, S. Chollet, F. Larek, J. Cormier, C. Templier, Low temperature nitriding behaviour of Ni<sub>3</sub>Al-like  $\gamma'$  precipitates in nickel-based superalloys, *J. Alloys Compd.* 771 (2019) 176–186. <https://doi.org/https://doi.org/10.1016/j.jallcom.2018.08.187>.
- [22] P.A.J. Bagot, O.B.W. Silk, J.O. Douglas, S. Pedrazzini, D.J. Crudden, T.L. Martin, M.C. Hardy, M.P. Moody, R.C. Reed, An Atom Probe Tomography study of site preference and partitioning in a nickel-based superalloy, *Acta Mater.* 125 (2017) 156–165. <https://doi.org/https://doi.org/10.1016/j.actamat.2016.11.053>.
- [23] X.Z. Qin, J.T. Guo, C. Yuan, C.L. Chen, H.Q. Ye, Effects of long-term thermal exposure on the microstructure and properties of a cast Ni-base superalloy, *Metall. Mater. Trans. A.* 38 (2007) 3014–3022.
- [24] Y.Q. Chen, T.J.A. Slater, E.A. Lewis, E.M. Francis, M.G. Burke, M. Preuss, S.J. Haigh, Measurement of size-dependent composition variations for gamma prime ( $\gamma'$ ) precipitates in an advanced nickel-based superalloy, *Ultramicroscopy.* 144 (2014) 1–8. <https://doi.org/https://doi.org/10.1016/j.ultramicro.2014.04.001>.
- [25] Y.Q. Chen, E. Francis, J. Robson, M. Preuss, S.J. Haigh, Compositional variations for small-scale gamma prime ( $\gamma'$ ) precipitates formed at different cooling rates in an advanced Ni-

based superalloy, *Acta Mater.* 85 (2015) 199–206.

<https://doi.org/https://doi.org/10.1016/j.actamat.2014.11.009>.

[26] M. Durand-Charre, *The microstructure of superalloys*, CRC press, 1998.

[27] H.D. Monte Carlo simulation of electron trajectory in solids, Casino version 3.2.0.1, Casino Copyright ©, D. Drouin, A. Réal Couture, D. Joly, N. Poirier-Demers, Monte Carlo simulation of electron trajectory in solids, Casino version 3.2.0.1, Casino Copyright ©, Univ. Sherbrooke. (2011) monte CARlo Simulation of electroN trajectory in s. <https://www.gel.usherbrooke.ca/casino/index.html>.

[28] A.S.M. Handbook, *Metallography and microstructures*, Ed. by GF Vander Voort, ASM International. 9 (2004).

[29] K. Thompson, D. Lawrence, D.J. Larson, J.D. Olson, T.F. Kelly, B. Gorman, In situ site-specific specimen preparation for atom probe tomography, *Ultramicroscopy*. 107 (2007) 131–139. <internal-pdf://0569441310/Thompson-2007-In situ site-specific specimen p.pdf>.

[30] S.Y. Sree Harsha Lalam H. Harada, H.K.D.H. Bhadeshia, MAP\_NICKEL\_LATTICE , (1999). <https://www.phase-trans.msm.cam.ac.uk/map/nickel/programs/lattice.html#refer>.

[31] S. Yoshitake, V. Narayan, H. Harada, H.K.D.H. Bhadeshia, D.J.C. Mackay, Estimation of the  $\gamma$  and  $\gamma'$  Lattice Parameters in Nickel-base Superalloys Using Neural Network Analysis, *ISIJ Int.* 38 (1998) 495–502. <https://doi.org/10.2355/isijinternational.38.495>.

[32] D.J.C. MacKay, *Mathematical Modelling of Weld Phenomena 3*, ed. by H, Cerjak HKDH Bhadeshia, *Inst. Mater. London*. 359 (1997).

[33] C.M. Katsari, H. Che, D. Guye, A. Wessman, S. Yue, Microstructural Characterization and Mechanical Properties of Rene 65 Precipitates, in: E. Ott, X. Liu, J. Andersson, Z. Bi, K. Bockenstedt, I. Dempster, J. Groh, K. Heck, P. Jablonski, M. Kaplan, D. Nagahama, C. Sudbrack

(Eds.), Proc. 9th Int. Symp. Superalloy 718 Deriv. Energy, Aerospace, Ind. Appl., Springer International Publishing Ag, [Katsari, C. M.; Che, H.; Guye, D.; Yue, S.] McGill Univ, Dept Mat Engr, Wong Bldg, 3610 Univ, Montreal, PQ H3A 0C5, Canada. [Wessman, A.] GE Aviat, Struct Mat Dev, One Neumann Way, Cincinnati, OH 45215 USA. Katsari, CM (reprint author), McGill Univ, Dept , 2018: pp. 629–641. [https://doi.org/10.1007/978-3-319-89480-5\\_41](https://doi.org/10.1007/978-3-319-89480-5_41).

[34] A.S.M.H. Volume, 4: Heat treating, ASM Int. 1012 (1991).

[35] A. Taylor, R.W. Floyd, The constitution of nickel-rich alloys of the nickel-titanium-aluminium system, J. Inst. Met. 81 (1952).

[36] D.M. Collins, L. Yan, E.A. Marquis, L.D. Connor, J.J. Ciardiello, A.D. Evans, H.J. Stone, Lattice misfit during ageing of a polycrystalline nickel-base superalloy, Acta Mater. 61 (2013) 7791–7804. <https://doi.org/https://doi.org/10.1016/j.actamat.2013.09.018>.

[37] S.T. Wlodek, M. Kelly, D. Alden, The structure of N18, Superalloys 1992. (1992) 467–476.

[38] A.J. Goodfellow, E.I. Galindo-Nava, K.A. Christofidou, N.G. Jones, T. Martin, P.A.J. Bagot, C.D. Boyer, M.C. Hardy, H.J. Stone, Gamma prime precipitate evolution during aging of a model nickel-based superalloy, Metall. Mater. Trans. A. 49 (2018) 718–728. [internal-pdf://183.34.23.172/Gamma Prime Precipitate Evolution During Aging.pdf](internal-pdf://183.34.23.172/Gamma%20Prime%20Precipitate%20Evolution%20During%20Aging.pdf).

[39] D.A. Porter, K.E. Easterling, M. Sherif, Phase Transformations in Metals and Alloys, (Revised Reprint), CRC press, 2009.

[40] R.A. Ricks, A.J. Porter, R.C. Ecob, The growth of  $\gamma'$  precipitates in nickel-base superalloys, Acta Metall. 31 (1983) 43–53. [https://doi.org/https://doi.org/10.1016/0001-6160\(83\)90062-7](https://doi.org/https://doi.org/10.1016/0001-6160(83)90062-7).

# **Chapter 5 : Microstructural characterization and mechanical properties of Rene 65 precipitates**

## **Preface**

After verifying that there is indeed a difference in composition among the three sizes in Chapter 4, in this Chapter the traditional experimental approach of changing one factor at a time was applied. The samples were in the as extruded condition in this chapter too. A non- traditional heat treatment with the purpose of softening the material for manufacturing was introduced for the first time. Time at holding temperature was the main variable in this work and hardness was measured as the outcome.

This chapter has been published as: Katsari, C. M., Che, H., Guye, D., Wessman, A., & Yue, S. (2018). Microstructural Characterization and Mechanical Properties of Rene 65 Precipitates. In E. Ott, X. Liu, J. Andersson, Z. Bi, K. Bockenstedt, I. Dempster, J. Groh, K. Heck, P. Jablonski, M. Kaplan, D. Nagahama, & C. Sudbrack (Eds.), *Proceedings of the 9th International Symposium on Superalloy 718 & Derivatives: Energy, Aerospace, and Industrial Applications* (pp. 629-641). Cham: Springer International Publishing Ag.<sup>[2]</sup> and licence to reuse in this thesis has been granted from Springer Nature.

## Abstract

Nickel based superalloys are used in the aerospace industry as turbine rotor material due to their high strength and excellent fatigue resistance at high temperature. High strength is required for the high stress and high temperature environments in which these alloys operate. This is achieved by their microstructure of gamma matrix/gamma prime precipitates. The latter can cause thermomechanical processing issues since they can make the material extremely hard. The purpose of this work is to characterize the gamma prime precipitates which are present in Rene 65, a newly developed cast and wrought nickel-based superalloy by General Electric and ATI. The main precipitate that was examined was the gamma prime phase  $[\text{Ni}_3(\text{Al,Ti})]$ , which largely determines the mechanical properties of the alloy. The gamma prime in this particular alloy was found to form in three different sizes; primary, secondary and tertiary. After various heat treatments, the differences in the volume fraction and morphology of each precipitate type is described and the effect of the precipitates on hardness is determined.

**Keywords:** gamma prime, nickel-based superalloy, heat-treatment, precipitation, hardness

## 5.1 Introduction

The manufacture of single crystal and directional solidification turbine blades requires a high precision casting technique. For cast and wrought superalloys, a thermomechanical processing route is required for compressor blades. Nickel based superalloys consist of a gamma matrix ( $\gamma$ ) and usually gamma prime ( $\gamma'$ ) or gamma double prime ( $\gamma''$ ) precipitates as strengthening phases. Their mechanical properties depend mainly on the characteristics of those precipitates (e.g. size, volume fraction, morphology).

Rene 65 (R65) is a newly developed nickel-based superalloy by General Electric and ATI Allvac. Its microstructure consists of  $\gamma$  matrix and three sizes of  $\gamma'$   $\text{Ni}_3(\text{Al,Ti})$  precipitates. It can

perform at higher temperatures than the commonly used Inconel 718 and it has lower production cost than the similar chemistry alloy Rene 88DT. More specifically, R65 is designed to operate at temperatures up to 700 °C, whereas IN718 operates at 650 °C. Moreover, R65 is a cast and wrought alloy, so it is less costly than the powder metallurgy route of R88DT [1].

The microstructure of Rene 65 consists of the Ni gamma matrix (FCC) and three different sizes of gamma prime precipitates: primary, secondary and tertiary. The primary  $\gamma'$  serves the purpose of pinning the grain boundaries, which prevents grain coarsening and thereby increases fatigue resistance, whereas secondary and tertiary contribute to the strength and creep resistance of the alloy [2-4].

In this report, the effect of various heat treatments on the morphology and the volume fraction of each precipitate as well as the hardness will be presented.

## 5.2 Experimental procedure

As-extruded cylindrical compression samples (9mm height and 6mm diameter) of Rene 65 were provided by GE Aviation Canada (9mm height and 6 mm diameter). The nominal composition can be found in Table 5-1:

**Table 5-1:** Chemical composition of Rene 65 (wt%).

Fe	Co	Cr	Mo	W	Al	Ti	Nb	B	C	Zr	Ni
1	13	16	4	4	2.1	3.7	0.7	0.016	0.01	0.05	Bal.

As mentioned before, the objective of this work was to improve the formability of Rene 65. Therefore, a heat treatment of the superalloy samples was introduced in order to produce a microstructure that could be easily thermomechanically processed to produce blades. The approach for the design of the heat treatment was to dissolve the majority of precipitates that exist in as-extruded condition. The complete absence of precipitates would lead to grain coarsening,

which is not desirable for fatigue resistance. Therefore, the microstructure should consist of coarse precipitates that would inhibit grain coarsening, while minimizing the impact on strength.

The heat treatment design was based on the precipitation data of ref [5]. It consisted of firstly an anneal at 1095 °C which is close to, but below, the solutionizing temperature (1116 °C) for 30 minutes to ensure homogeneous annealing in an industrial environment; for the size of the samples given, 10 minutes should be sufficient. Following the annealing step, samples were cooled to 954 °C, held for various times from 0 minutes to 2 hours, and either air cooled (AC) or water quenched (WQ) to room temperature. The temperature of 954 °C was selected because the equilibrium precipitation quantity at that temperature as predicted by ref. [5] is almost 75% of the total precipitation available. Since only 25% of precipitates would be available at that point, the concept was to minimise any further precipitation during air cooling and coarsen the existing 75%.

For the heat treatments, an infra-red furnace was used in order to achieve the best temperature control. When compared to the box furnace there is less fluctuation in the temperature, which is particularly important for the annealing stage, as well as being able to better specify the cooling rate from annealing to the hold temperature, as well as the cooling rate to room temperature.

Characterisation by light optical microscopy (LOM) was achieved using a Nikon EPIPHOT 200 optical microscope coupled with CLEMEX image analysis software in order to measure the grain size. To etch the grain boundaries and primary  $\gamma'$  precipitates, an etchant based on Kalling's Reagent was used<sup>[6]</sup>. Scanning electron microscopy (SEM) was carried out using a Hitachi SU3500 Variable-Pressure microscope at accelerating voltages of 30kV and 5kV. To reveal the  $\gamma'$  under SEM conditions electropolishing and electroetching at 20V and 5V were carried out respectively. Image analysis for quantifying microstructural features was achieved using

ImageJ software. The secondary  $\gamma'$  precipitates, were measured manually by Image J software, with a range of 48-75 representative precipitate measurements for each mean value.

The effect of heat treatment on Vickers micro-hardness was measured using a Clark CM-100AT micro-hardness testing machine in conjunction with CLEMEX CMT indent measurement software. This was done as it is a quick way to initially evaluate the mechanical properties of the material, as there is a relationship between hardness and ultimate tensile stress and a rough correlation between hardness and yield stress. Indents were created with a force of 200g and measured at a magnification of 500X.

### 5.3 Results and discussion

Initially, the as received samples from GE Aviation were microstructurally characterized and all hardness results after heat treatment are compared with as received (extruded) sample hardness, 445HV. In Figure 5-1 the equiaxed grain structure of the superalloy can be observed, with ASTM grain size of 9.5 (11.9 $\mu$ m). The grain boundaries are pinned by the primary  $\gamma'$  precipitates which were 12% of the volume fraction. The primary  $\gamma'$  precipitates of the as extruded condition have a mean diameter of 2.69 $\pm$ 0.7  $\mu$ m.

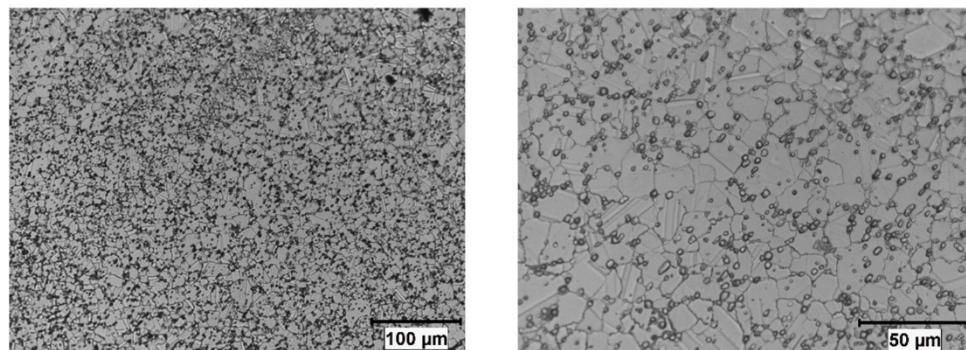


**Figure 5-1:** As extruded microstructure at x200 (left) and x500 (right).

Further investigation of precipitate microstructure characterization requires Scanning Electron Microscopy, therefore the heat treated samples were compared with the as extruded SEM images for this paper. In Figure 5-2 a multimodal distribution of  $\gamma'$  precipitates can be observed. In the as extruded state, secondary precipitates were determined to have a size of 121nm. Results of EDS analysis confirmed the composition of the primary and secondary precipitates to be consistent with the  $\gamma'$  intermetallic structure  $\text{Ni}_3(\text{Al,Ti})$ . Future experiments will determine the exact chemical composition of each precipitate.

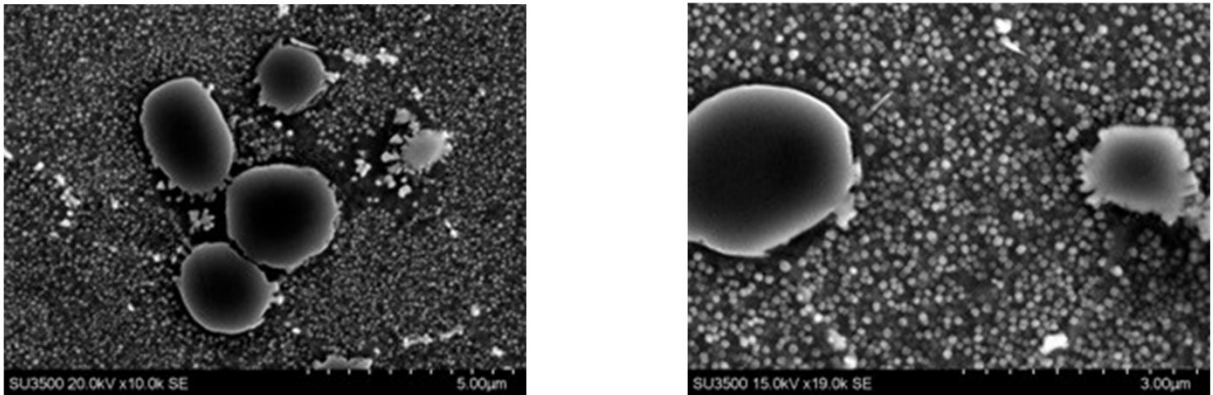


**Figure 5-2:** SEM images of multimodal  $\gamma'$  precipitate size distribution in as-extruded Rene 65.

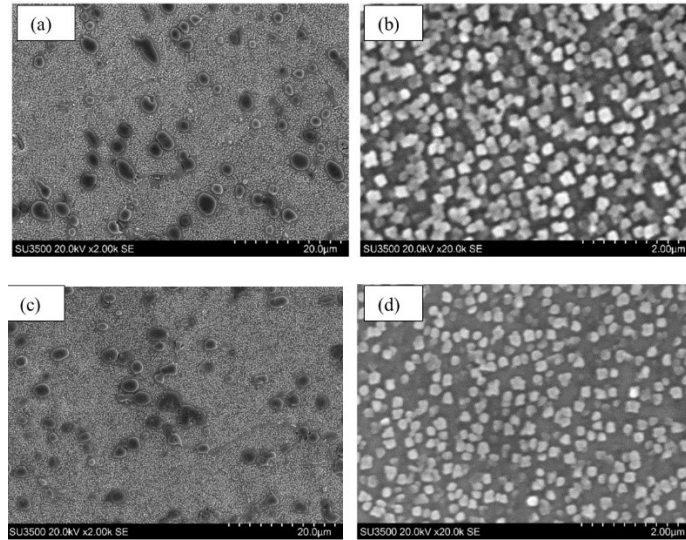
Optical microscopy of heat treated samples revealed grain sizes from 8.7 up to 9.9 ASTM, which is within the acceptable range for fatigue resistance (8-12 ASTM). For precipitate morphology characterization, SEM images of x2000 and x20000 were captured. In order to distinguish the heat treatments, the following notations are shown in Table 5-2, where i.e.  $\text{A}^{1095}_{30}$   $\text{H}^{954}_{30}$  WQ is an anneal (A) at 1095C for 30 minutes, followed by a hold (H) for 30 minutes at 954 °C, and finally water quench (WQ) until room temperature.

**Table 5-2:** Heat treatment terminology.

Term	Meaning
$A^{\text{temp}}_{\text{time}}$	Anneal temperature in °C and time in minutes
$H^{\text{temp}}_{\text{time}}$	Hold temperature in °C and time in minutes
AC	Air cooling
WQ	Water quenching

Figure 5-3 shows the structure of the  $A^{1095}_{30}H^{954}_0WQ$  and  $A^{1095}_{30}H^{954}_0AC$  samples at low (left) and high (right) magnification. From Fig. 5-3 (a) and (c), it is noted that the average size of the primary  $\gamma'$  precipitates of both heat treatments are from 1 to 5  $\mu\text{m}$  on average and the size and distribution are similar to the as-extruded microstructure. Image analysis revealed the volume fractions to be 11.70% for  $A^{1095}_{30}H^{954}_0WQ$  and 11.27% for  $A^{1095}_{30}H^{954}_0AC$ . The primary  $\gamma'$  volume fraction after heat treatment is approximately the same as the as extruded condition. From Ref [5], which is referring to the total volume fraction of  $\gamma'$  precipitates, and assuming the solution temperature seems close to what the extrusion temperature likely was, we could conclude that at these elevated temperatures, the only remaining gamma prime will be primary gamma prime. Primary  $\gamma'$  volume fraction remains in the same range after annealing at 1095°C, whereas after annealing at 1115°C for 30 minutes and then water quench, the primary  $\gamma'$  volume fraction dropped to 3.1%. Secondary  $\gamma'$  precipitates are intragranular, with the exception of the area close to primary  $\gamma'$  precipitates, where precipitate-free zones can be observed. At higher magnifications, in Fig.5-3 (c) and (d), the secondary  $\gamma'$  precipitates of both samples have an irregular or cuboidal morphology. The secondary precipitates in the  $A^{1095}_{30}H^{954}_0WQ$  sample have a mean diameter of  $206\pm 44.1$  nm

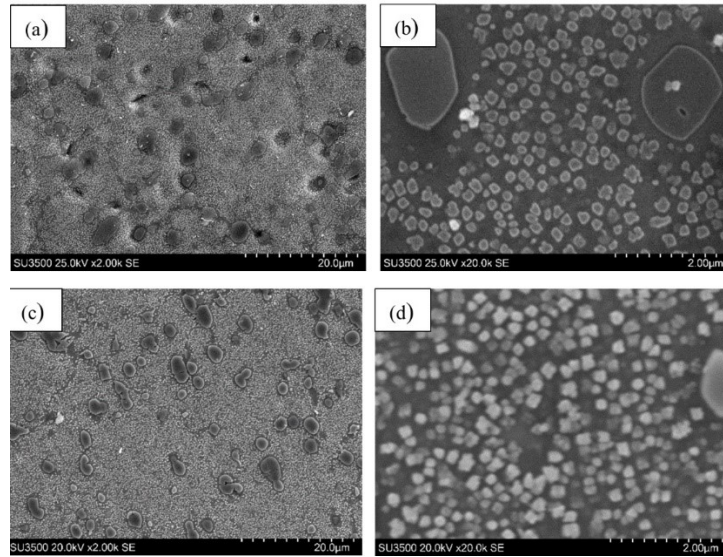
while for the  $A^{1095}_{30}H^{954}_0AC$  sample, the mean secondary precipitate size was  $189\pm 29.5$  nm. Further observations in higher magnifications will be conducted.



**Figure 5-3:** Representative SEM microstructures of 0 minute hold at  $954^{\circ}C$  heat-treated samples taken at: (a) and (c) low magnification of  $A^{1095}_{30}H^{954}_0WQ$  and  $A^{1095}_{30}H^{954}_0AC$  respectively and (b) and (d) high magnification  $A^{1095}_{30}H^{954}_0WQ$  and  $A^{1095}_{30}H^{954}_0AC$ .

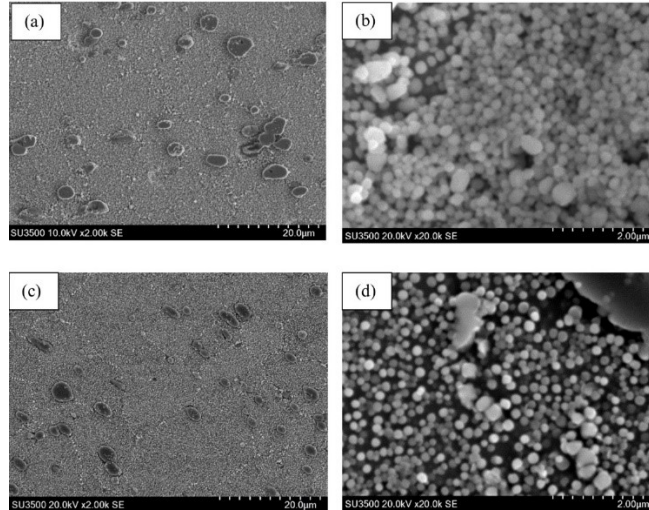
In Fig. 5-4 the microstructure of the  $A^{1095}_{30}H^{954}_{10}WQ$  and  $A^{1095}_{30}H^{954}_{10}AC$  samples at high and low magnification can be observed. At low magnification the primary  $\gamma'$  precipitate size and distribution is similar to that of the as-extruded structure. The primary  $\gamma'$  fraction of the structures shown in Fig.5-4 (a) and (c) are 11.0% and 13.0% respectively. The volume fraction of primary gamma prime should almost entirely depend on the anneal temperature the material reached at  $1095^{\circ}C$ , so the observable difference is related to the measurement mean error. Similarities appear for secondary  $\gamma'$  precipitates as well. The morphology of the secondary  $\gamma'$  precipitates are irregular or cuboidal. From images of a similar or higher magnification than those in Fig.5-4 (b) and (c), the secondary precipitates in the  $A^{1095}_{30}H^{954}_{10}WQ$  sample were found to have a mean diameter of  $181\pm 42.2$  nm while for the  $A^{1095}_{30}H^{954}_{10}AC$  sample, the mean secondary precipitate size was  $172\pm 27.1$  nm. Spheroidal tertiary  $\gamma'$  precipitates were also observed near the primary  $\gamma'$  precipitates

in the  $A^{1095}_{30}H^{954}_{10}AC$ . Their size is below 100 nm and they were difficult to distinguish to get an exact size.



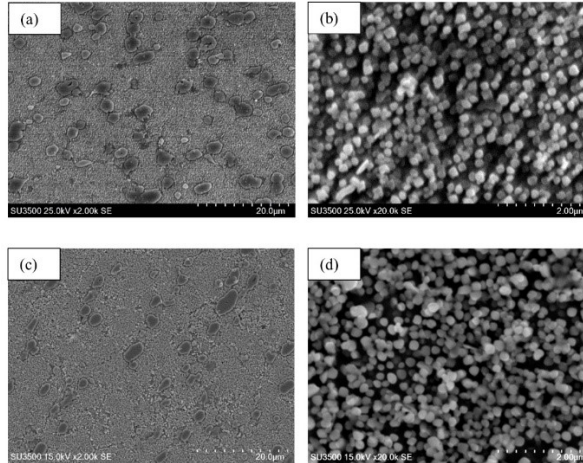
**Figure 5-4:** Representative SEM microstructures of 10 minute hold time at 954°C heat-treated samples taken at: (a) and (c) low magnification of  $A^{1095}_{30}H^{954}_{10}WQ$  and  $A^{1095}_{30}H^{954}_{10}AC$  respectively and (b) and (d) high magnification  $A^{1095}_{30}H^{954}_{10}WQ$  and  $A^{1095}_{30}H^{954}_{10}AC$ .

Figure 5.5  $A^{1095}_{30}H^{954}_{30}WQ$  and  $A^{1095}_{30}H^{954}_{30}AC$  heat treatment sample microstructure is presented. In Fig.5-5 (a) and (c), the primary  $\gamma'$  precipitates can be identified and appear to have either a spheroidal or an irregular morphology. Primary  $\gamma'$  precipitates make up 9.64% and 9.10% of the structure of the  $A^{1095}_{30}H^{954}_{30}WQ$  and  $A^{1095}_{30}H^{954}_{30}AC$  respectively, which is a lower percentage than 0 and 10 minutes at the hold temperature. Secondary  $\gamma'$  precipitates are located intragranular, however in this sample they appear to have a spheroidal morphology instead of the irregular or cuboidal morphology that was observed in the 0 and 10 min. hold at 954°C samples. The secondary precipitates in the  $A^{1095}_{30}H^{954}_{30}WQ$  sample were found to have a mean diameter of  $168 \pm 35.5$  nm while for the  $A^{1095}_{30}H^{954}_{30}AC$  sample, the mean secondary precipitate size was  $172 \pm 25.7$  nm. No tertiary  $\gamma'$  can be observed from those images.



**Figure 5-5:** Representative SEM microstructures of 30 minute hold time at 954°C heat-treated samples taken at: (a) and (c) low magnification of  $A^{1095}_{30}H^{954}_{30}WQ$  and  $A^{1095}_{30}H^{954}_{30}AC$  respectively and (b) and (d) high magnification  $A^{1095}_{30}H^{954}_{30}WQ$  and  $A^{1095}_{30}H^{954}_{30}AC$ .

Figure 5-6 shows the microstructure of the  $A^{1095}_{30}H^{954}_{60}WQ$  and  $A^{1095}_{30}H^{954}_{60}AC$  samples. The primary  $\gamma'$  precipitates can be identified from the low magnification images and appear to have either a spheroidal or an irregular morphology. Primary  $\gamma'$  precipitates make up 14.3% and 10.1% of the structure of the  $A^{1095}_{30}H^{954}_{60}WQ$  and  $A^{1095}_{30}H^{954}_{60}AC$  respectively. The primary fraction in the  $A^{1095}_{30}H^{954}_{60}WQ$  sample is larger than what is typically observed in samples which underwent this series of heat treatment steps. Secondary  $\gamma'$  precipitates are located in the grains, those which are observed in Fig.5-6 (b) and (d). They appear to have a spheroidal morphology with mean sizes of  $169\pm 22.4$  nm and  $196\pm 44.3$  nm for the  $A^{1095}_{30}H^{954}_{60}WQ$  and  $A^{1095}_{30}H^{954}_{60}AC$  samples respectively. A second size fraction of secondary  $\gamma'$  precipitates were identified in the  $A^{1095}_{30}H^{954}_{60}WQ$  sample which have a more cuboidal morphology and have and mean dimensions of  $197\pm 18$  nm X  $200\pm 17$  nm. In high magnification of a different site of  $A^{1095}_{30}H^{954}_{60}AC$  sample the presence of tertiary precipitates can be identified in Figure 5-7. Because of their size, these particles were difficult to resolve but have a diameter less than 100nm, as was mentioned above. Throughout the structure they are located in the regions near the primary  $\gamma'$  precipitates.



**Figure 5-6:** Representative SEM microstructures of 60 minute hold time at 954°C heat-treated samples taken at: (a) and (c) low magnification of  $A^{1095}_{30}H^{954}_{60}WQ$  and  $A^{1095}_{30}H^{954}_{60}AC$  respectively and (b) and (d) high magnification  $A^{1095}_{30}H^{954}_{60}WQ$  and  $A^{1095}_{30}H^{954}_{60}AC$ .

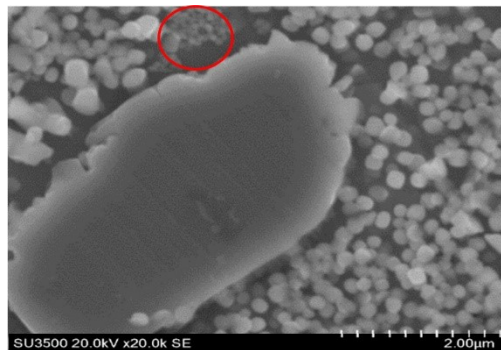


**Figure 5-7:** SEM Image of  $A^{1095}_{30}H^{954}_{60}AC$  sample highlighting tertiary  $\gamma'$ .

The two final heat treatment microstructures ( $A^{1095}_{30}H^{954}_{120}WQ$  and  $A^{1095}_{30}H^{954}_{120}AC$ ) can be seen in Figure 5-8. Primary  $\gamma'$  precipitates make up 11.6% and 10.6% of the structure of the  $A^{1095}_{30}H^{954}_{120}WQ$  and  $A^{1095}_{30}H^{954}_{120}AC$  respectively with either an irregular or spheroidal morphology. At higher magnifications, in Fig.5-8 (c) and (d), the secondary  $\gamma'$  precipitates have a spheroidal morphology which have a mean size of  $213\pm 37.4$  nm and  $179\pm 18.2$  nm for the  $A^{1095}_{30}H^{954}_{60}WQ$  and  $A^{1095}_{30}H^{954}_{60}AC$  samples respectively. A second size fraction of secondary precipitates with a cuboidal or irregular morphology can be observed in the  $A^{1095}_{30}H^{954}_{120}AC$  sample from Fig.5-8(c) and the details in Fig. 5-9. These larger secondary  $\gamma'$  precipitates have

mean dimensions of  $362 \pm 50.9$  nm X  $434 \pm 52.4$  nm. The larger mode of precipitates were included in the measurement of the size.

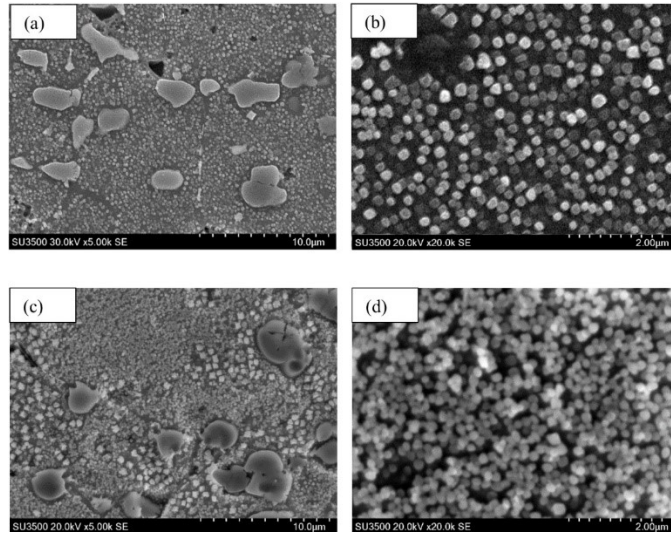


**Figure 5-8:** Representative SEM microstructures of 120 minute hold time at  $954^{\circ}\text{C}$  heat-treated samples taken at: (a) and (c) low magnification of  $\text{A}^{1095}_{30}\text{H}^{954}_{120}\text{WQ}$  and  $\text{A}^{1095}_{30}\text{H}^{954}_{120}\text{AC}$  respectively and (b) and (d) high magnification  $\text{A}^{1095}_{30}\text{H}^{954}_{120}\text{WQ}$  and  $\text{A}^{1095}_{30}\text{H}^{954}_{120}\text{AC}$ .

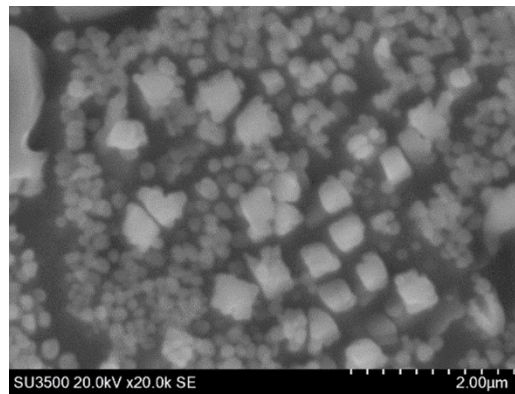


**Figure 5-9:** SEM image highlighting the details of larger secondary  $\gamma'$  precipitates in  $\text{A}^{1095}_{30}\text{H}^{954}_{120}\text{AC}$  sample.

As mentioned above, microhardness Vickers test was conducted to determine the mechanical properties after the various heat treatments. As can be observed from Figure 5-10, for both AC and WQ samples there is a general trend of increase in hardness for samples up to a hold period of 30 minutes after which the hardness of both the AC and WQ samples decrease in

hardness with increased hold time. All the heat treated samples had lower hardness values compared to the as-received condition.

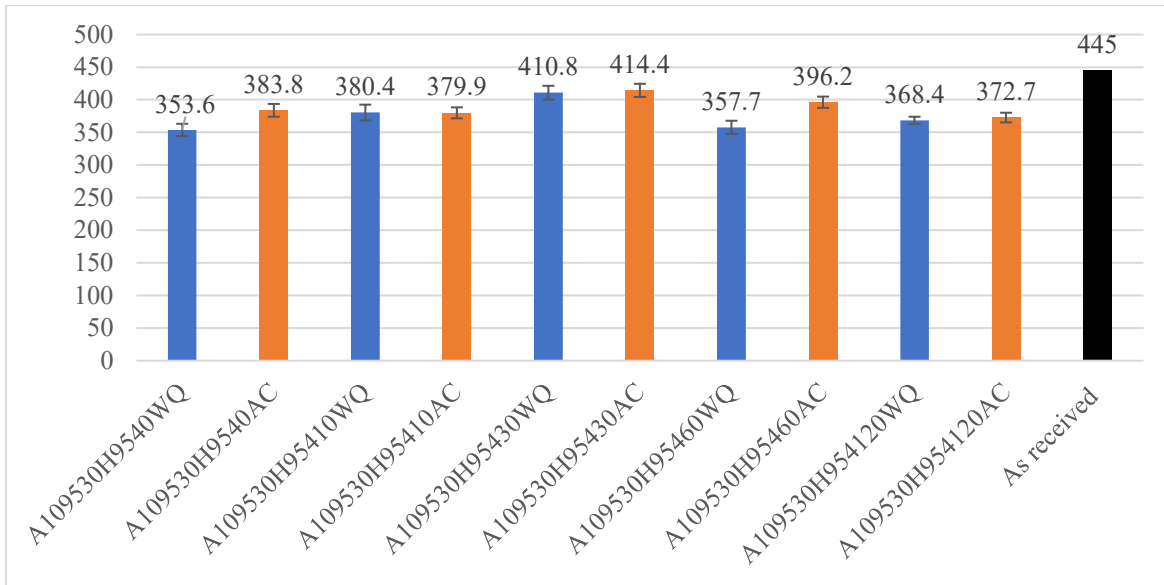


**Figure 5-10:** Hardness Profile, blue bars for WQ and orange bars for AC.

The mean secondary  $\gamma'$  precipitate size is decreasing at times less than 30 minutes after which the mean size of secondary  $\gamma'$  precipitates increases for all times investigated. It is also notable that for times less than 30 minutes mean precipitate size is larger in samples that underwent water-quenching than those which were subjected to air cooling to room temperature. However, for hold times at 954°C greater than 30, the mean secondary  $\gamma'$  precipitate size of air-cooled samples is greater than that determined for water quenched samples. In order to verify those results, nucleation and growth rates of each size of precipitates needs to be determined.

From the aforementioned observations, there is a notable relationship between the hardness and the mean secondary precipitate size as can be seen in Fig. 5-12. When there is a decrease in the mean secondary precipitate size hardness increases and when mean secondary precipitate size increases hardness decreases.

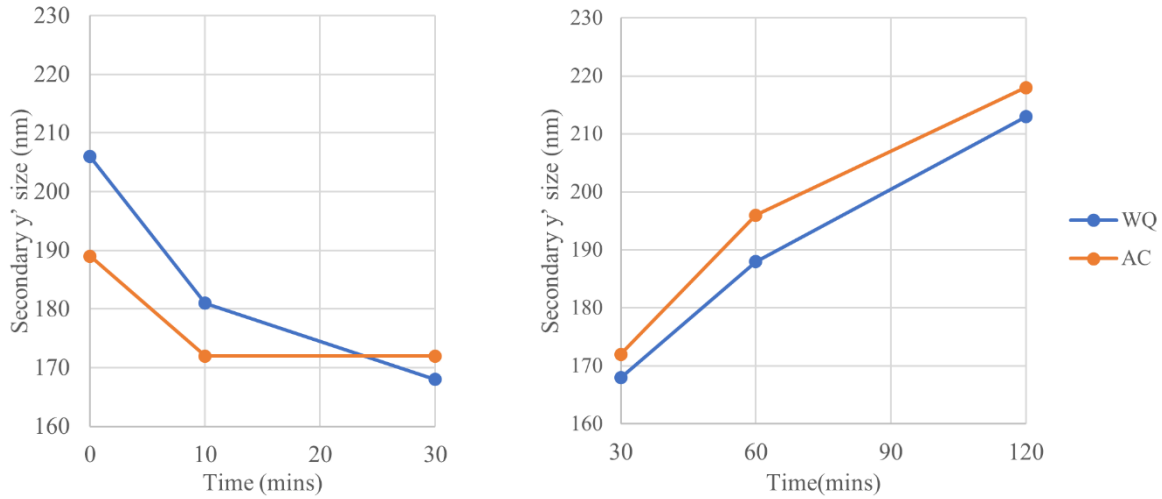


**Figure 5-11:** Change in the average size of secondary  $\gamma'$  precipitates as a function of hold time at 954°C differentiated by final cooling method.

The distribution of measured secondary precipitates for the air cooled series gives an indication of why the mean precipitate size behaves this way. Based on the literature <sup>[7]</sup>, the length of delay before the cooling and reduced severity of cooling always increases the size of the secondary  $\gamma'$  precipitates. Therefore, the expectation is that the mean size of the secondary  $\gamma'$  precipitates from hold times 0 to 120 minutes will be increasing. This is not the case, due to what appears to be an increasing number of fine secondary  $\gamma'$  precipitates being present in the structure. The secondary  $\gamma'$  precipitates, which are measured by Image J software, are considered to be representative of those which exist throughout the structure. It is clear that large secondary  $\gamma'$  precipitates (>180 nm) are present in all structures, however there is an increased frequency of small precipitates in the structure for all periods less than 30 minutes. As 48-75 precipitates are chosen for calculation of the mean secondary  $\gamma'$  precipitate size this will affect the mean. This could indicate the nucleation of new secondary  $\gamma'$  precipitates, which do not have sufficient time to grow to a size large enough to maintain the mean size; as well the growth of existing precipitates is not sufficient to offset the increase in the number of small precipitates. Beyond 30 minutes, the

reduced frequency of secondary  $\gamma'$  precipitates  $<160$  nm may indicate the reduction in the nucleation of new secondary  $\gamma'$  precipitates and the growth of existing precipitates dominates causing the mean size to increase. A similar case can be made for the water quenched samples.

As secondary precipitates, experience growth beyond 50 nm there is a decrease in strength of the material with increasing secondary precipitate size. If the mean secondary  $\gamma'$  precipitate sizes for hold times from 30 to 120 mins are used, due to the reduction in the evolution of new fine secondary  $\gamma'$  precipitate, there is a strong negative linear relationship between the secondary  $\gamma'$  precipitate size and hardness of Rene 65, highlighting the difference between air cooled and water quenched samples, as can be seen in Fig. 5-12.

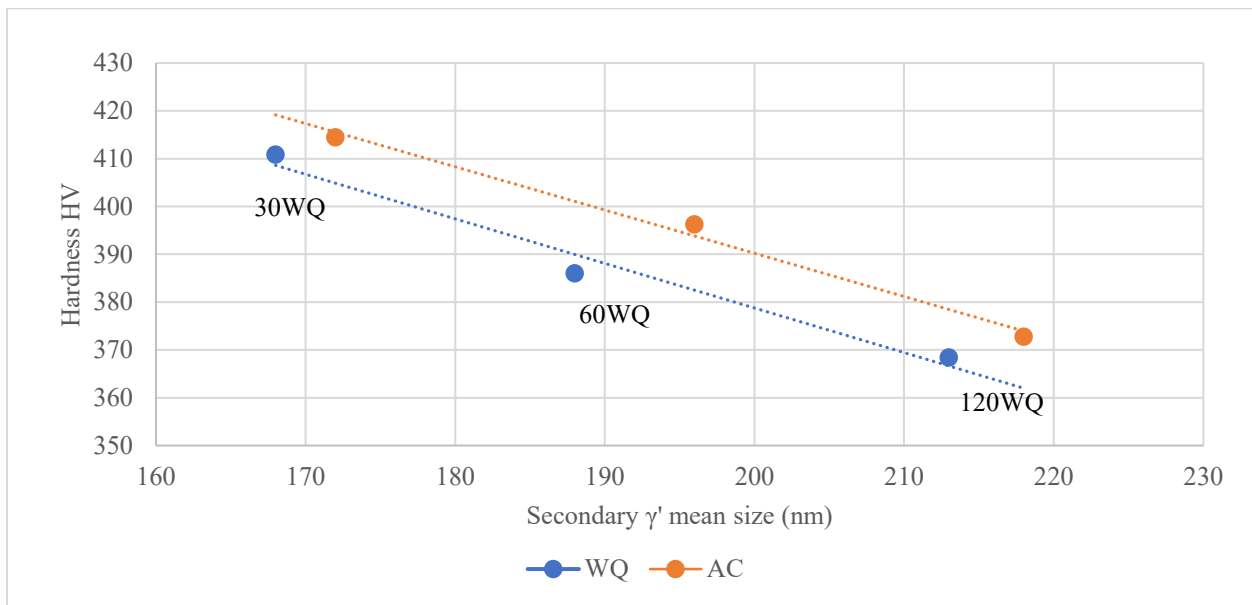


**Figure 5-12:** Relationship between hardness and secondary gamma prime precipitate size.

#### 5.4 Conclusions & Future Work

Microstructural characteristics and their effect of hardness of Rene 65 has been investigated. As conclusions from the current work, we can observe that the strength of that Rene 65 is dependent on the size and distribution of secondary  $\gamma'$  precipitates. Microstructural  $\gamma'$  precipitate evolution was shown to be influenced by holding at a temperature below the annealing

temperature. The mean secondary precipitate size decreases for short times because of the effect of nucleation new secondary precipitates being greater than the effect of the growth caused by delayed cooling of existing precipitates. For longer hold times at 954°C, the growth expected is seen because the effect of growth of secondary  $\gamma'$  precipitates is greater than the effect of nucleation of new precipitates.

There is a need to quantify the effect of heat treatment on the fraction of secondary  $\gamma'$  precipitates. Image analysis of SEM images appears to be a good method for the quantification of the primary  $\gamma'$  precipitates, it cannot be employed for accurate quantification of the secondary  $\gamma'$  precipitates. Although, after etching, the morphology of the secondary precipitates are revealed well, because of the volume of precipitates and the interaction of the electron beam with the sample, the area of the surface covered by secondary  $\gamma'$  precipitates cannot be determined.

For future work, further investigation of precipitate characterization with EBSD and STEM will be conducted as well as compression testing to enhance the hardness results of the current work.

## **5.5 Acknowledgements**

Financial support from the Natural Science and Engineering Council of Canada, GE Aviation, Bromont, Quebec Canada, the Consortium de Recherche et D'innovation en Transformation Métallique and the McGill Engineering Doctoral Award (to C.M. Katsari) is gratefully acknowledged.

## **5.6 References**

[1] Laurence A, Cormier J, Villechaise P, Billot T, Franchet J-M, Pettinari-Sturmel F, Et Al. Impact Of The Solution Cooling Rate And Of Thermal Aging On The Creep Properties Of The

New Cast & Wrought René 65 Ni-Based Superalloy. 8th International Symposium On Superalloy 718 And Derivatives: John Wiley & Sons, Inc.; 2014. P. 333-48.

[2] Wessman Al, Aude; , Cormier J, Villechaise P, Billot T, Franchet J-M, Editors. Thermal Stability Of Cast And Wrought Alloy Rene 65. Superalloys 2016: Proceedings Of The 13th International Symposium On Superalloys; 2016.

[3] Reed Rc. The Superalloys: Fundamentals And Applications. Cambridge: Cambridge University Press; 2006.

[4] Locq D, Caron P, Raujol S. On The Role Of Tertiary Gamma Prime Precipitates In The Creep Behavior At 700°C Of A Powder Metallurgy Disk Superalloy. Green Ka, Pollock Tm, Harada H, Et Al Superalloy, Warrendale, Pa: The Minerals, Metals And Materials Society (TMS). 2004:179-88

[5] Charpagne M-A, Billot T, Franchet J-M, Bozzolo N. Heteroepitaxial Recrystallization Observed In René 65™ And Udimet 720™: A New Recrystallization Mechanism Possibly Occurring In All Low Lattice Mismatch  $\Gamma$ - $\Gamma'$  Superalloys Superalloys 2016: John Wiley & Sons, Inc.; 2016. P. 415-26.

[6] Heaney Ja, Lasonde Ml, Powell Am, Bond Bj, O'brien Cm. Development Of A New Cast And Wrought Alloy (René 65) For High Temperature Disk Applications. 8th International Symposium On Superalloy 718 And Derivatives: John Wiley & Sons, Inc.; 2014. P. 67-77.

[7] P.R. Bhowal, Metallurgical Transactions A (Physical Metallurgy and Materials Science), 21 (1990) 1709-1717

## **Chapter 6 : Taguchi Design for heat treatment of Rene 65 components**

### **Preface**

In this chapter the first attempt to apply experimental design for the optimization of the proposed heat treatment schedule of Chapter 5 is presented. Taguchi design included a small number of experiments and the parameters as well as their level tested were based on results of Chapter 5, literature values and industrial applicability. The samples in this chapter were deformed in their as-received condition.

This chapter has been published as: Katsari, C. M., Wessman, A., & Yue, S. (2020). Taguchi Design for Heat Treatment of Rene 65 Components. *Journal of Materials Engineering and Performance*, 1-9.<sup>[3]</sup> and licence to reuse it in this thesis has been granted from Springer Nature.

## Abstract

Rene 65 is a nickel-based superalloy used in aerospace components such as turbine blades and disks. The microstructure in the as received condition of the superalloy consists of ~40% volume fraction of gamma prime precipitates, which gives such a high strength that thermomechanical processing is problematic. The goal of this study was to improve the processability of Rene 65 by developing a heat treatment to lower the strength through changes in the size distribution and volume fraction of those precipitates. Gamma prime in this alloy is observed in three sizes, ranging from a few  $\mu\text{m}$  to tens of nm. For the design of the heat treatments, Taguchi's L8 matrix Design of Experiments (DOE) was used. The four factors that are examined are cooling rate, hold temperature, hold time and cooling method to room temperature. The levels of the factors were two (high and low) with replication. Microstructures were characterized by Scanning Electron Microscopy, and mechanical properties by Vickers microhardness testing. Regression analysis on the results revealed that the most significant factor for this design is hold temperature. The softest sample and the hardest sample have a significant difference microstructurally, with the latter having a trimodal distribution of precipitates which is believed to cause the strength.

**Keywords:** Experimental Design, Taguchi, Heat Treatment, Superalloys, Thermomechanical Processing, Hardness

## 6.1 Introduction

Nickel based superalloys have been used in various aircraft engine components for many years due to their ability to operate at high temperature and high stress environments <sup>[1-4]</sup>. This comes usually from precipitation hardening, with the most common strengthening phase being the gamma prime ( $\gamma'$ ) precipitate <sup>[5]</sup>. The usual precipitation heat treatment for achieving this strength

is by solutionizing and quenching to form a bimodal gamma prime distribution and then aging to achieve peak strength via a trimodal gamma prime distribution [2, 5]. In Rene 65,  $\gamma'$  is present in the cast and wrought condition in three sizes ranging from a few  $\mu\text{m}$  to tens of nm [6-12]. Primary  $\gamma'$  ( $\mu\text{m}$ ) is observed at the grain boundaries while secondary  $\gamma'$  (hundreds of nm) and tertiary  $\gamma'$  (tens of nm) are nucleating within the grains. The latter two size ranges are contributing to strength whereas primary  $\gamma'$  serves as pinning mechanism for grain boundaries [13].

For manufacturing purposes, the hardness that to which  $\gamma'$  is contributing should be minimized without imparting the grain coarsening that could occur if primary  $\gamma'$  is dissolved. The aim of this work is to find a heat treatment to reduce the hardness of the alloy for manufacturing purposes, without changing the grain size for the final application.

From previous work on heat treatments for manufacturing of parts made of Rene 65 [10], it was observed that the proposed heat treatment schedule was indeed reducing the hardness since all the heat-treated samples had lower hardness values compared to the as-received condition. The variables of that heat treatment were “hold time at 954°C” and “cooling method to room temperature (air or water)”, with the latter being evaluated by a separate set of experiments. In other words, that experimentation setup was following the one- factor-at-a-time (OFAT) approach, which is not able to consider interactions between factors [14, 15]. In this work with the help of Design of Experiments and more specifically a Taguchi design, an attempt to find an optimum heat treatment as well as understand which parameters affect the reduction in hardness has been made. In addition, more experimental data are produced for this kind of processing heat treatments that could eventually be fitted to a supervised learning algorithm for machine learning.

## 6.2 Experimental methods

Samples of worked Rene 65 parts were provided by GE Aviation, Bromont. The original cast ingot was produced by triple melt (VIM,VAR,ESR) as described in [8]. The nominal composition of this Ni based alloy in wt% is: Cr 16 %, Co 13%, Mo 4%, W 4%, Ti 3.7%, Al 2.1%, Fe 1%, Nb 0.7%, C 0.015%, Zr 0.05%, B 0.016% [6]. Annealing and hold temperatures were based on ref [10]. The heat treatment design was based on Taguchi's L8 matrix, which for four factors is allowing calculations of two-way interactions [16]. To determine which factors would be examined as well as their levels, results from previous work [10] were used. From [11], the level of annealing temperature (1095°C) was determined in order for it to be sub-solvus since no thermodynamic calculations were made in this work to find the solvus temperature. Annealing temperature was not considered as a factor in this design. From [10], microstructural  $\gamma'$  precipitate evolution was shown to be influenced by holding at a temperature below the annealing temperature. Both air cooled and water quenched samples had a general trend of increasing hardness up to a hold period of 30 minutes at 954°C. Furthermore, 30 minutes is an industrially acceptable time, so this was the high level for factor "hold time". For "cooling method to room temperature" it was decided that gas quenching would not be as severe as water quenching for the parts and therefore air cooling (AC) and gas quenching (GC) were the two levels of this categorical factor. Gas quenching was achieved by applying compressed air after the sample was out of the furnace. This was a faster cooling rate than air but slower than water. Furthermore, it would be interesting to see how hold temperature is affecting the hardness. From the literature [12, 17-20], cooling rate is also an important factor affecting  $\gamma'$  morphology and therefore hardness, so it was also included in the design as a factor. The heating rate for all samples was 10°C/min and was not considered as a factor for this

design. The final assignment of names of factors was based on heat treatment sequence and their levels can be summarized in Table 6-1:

**Table 6-1:** Factors' levels.

<b>Factors</b>	<b>Low level</b>	<b>High level</b>
A: cooling rate from 1095°C	5 °C /min	25 °C /min
B: hold temperature	800 °C	900 °C
C: time at hold temperature	0 min	30 min
D: cooling method to room temperature	Air cool (AC)	Gas quench (GC)

Taguchi's L8 matrix was chosen since it allows estimation of two-way interactions among the parameters on the corners of the linear graphs. In this experimental design, as can be graphically described in Fig.6-1, only Factor D is assumed to have no interaction with the other three, since cooling to room temperature was the last step of the heat treatment and it was treated as separate set of experiments in the previous work. For the other three factors, interactions between cooling rate and hold temperature(A\*B) and hold temperature and hold time (B\*C) were considered logical for investigation.

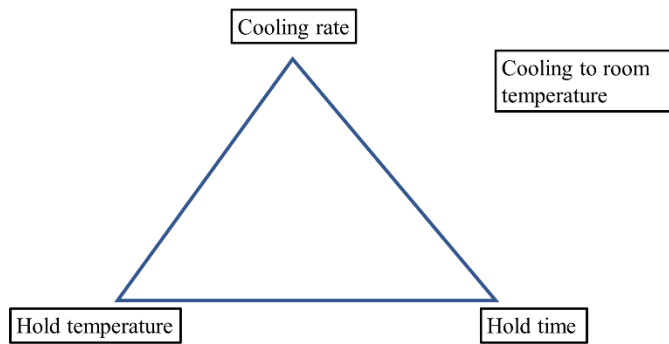


**Figure 6-1:**Interaction Lines.

For the statistical analysis, Minitab software was used, and the steps are described in Figure6-2.

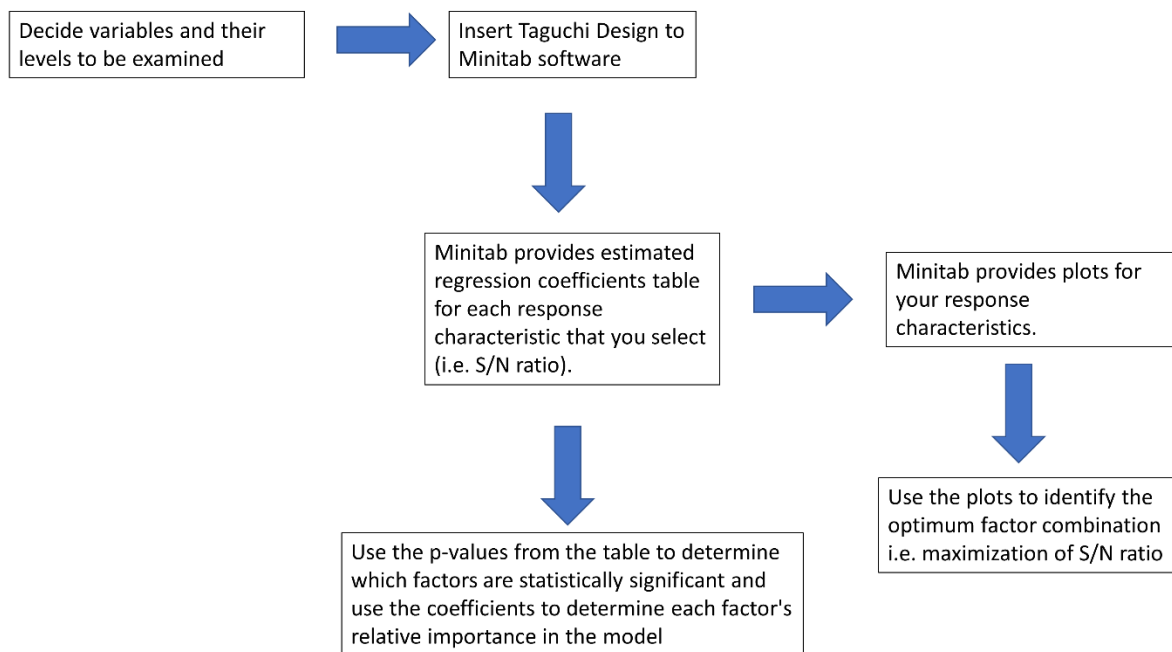


**Figure 6-2:** Flow chart of Taguchi design analysis using Minitab software.

For the heat treatments, a Sentro Tech box furnace with a Eurotherm 2408 process controller was used. The use of the process controller made varying furnace cooling rate (Factor A) possible.

Vickers microhardness was measured as a response for the design. A Clark CM-100AT micro-hardness tester equipped with CLEMEX CMT indent measurement software was used for those measurements. This was a fast way to measure mechanical properties as the response of the experiments and it provides information for future experiments such as compression tests for more comprehensive mechanical property characterization. Indents were created with a force of 200g, 15 sec dwell time and measured at a magnification of 500X.

A Hitachi SU3500 Variable-Pressure microscope at accelerating voltages of 20kV was used for low magnification (x1K) microstructural characterization of  $\gamma'$  precipitates. Energy Dispersive Spectroscopy (EDS) was used to identify second phases. A Hitachi SU8000 at 3kV was used for higher resolution imaging (x20K magnification) and EDS at 10kV for qualitative analysis of  $\gamma'$  and matrix. In both cases the objective lens aperture was set to 2 and the working distance was 13 mm. To reveal the  $\gamma'$  precipitation under SEM conditions, the  $\gamma$  matrix was selectively removed with electropolishing and electroetching at 15V and 5V respectively at room temperature with an etchant based on methanol and perchloric acid. Quantification of precipitate size was achieved using ImageJ image analysis software by measuring manually approximately 50 precipitates (where available) from 5 different regions.

### **6.3 Results and Discussion**

Statistical analysis

*Taguchi Design*

The combinations of factor levels as well as the average responses are recorded in Table 6-2. For the statistical analysis, only the average values were used, and the standard deviation is represented in Fig.6-3. The heat treatments were performed in random order.

**Table 6-2:** Experimental design.

<b>Standard order</b>	<b>A</b>	<b>B</b>	<b>C</b>	<b>D</b>	<b>HV 1</b>	<b>HV 2</b>
<b>1</b>	5	800	0	AC	401±12	392±8
<b>2</b>	5	800	30	GC	400±6	404±8
<b>3</b>	5	900	0	GC	371±5	379±9
<b>4</b>	5	900	30	AC	387±16	386±7
<b>5</b>	25	800	0	GC	427±9	420±4
<b>6</b>	25	800	30	AC	449±6	445±10
<b>7</b>	25	900	0	AC	402±9	410±4
<b>8</b>	25	900	30	GC	409±8	396±26

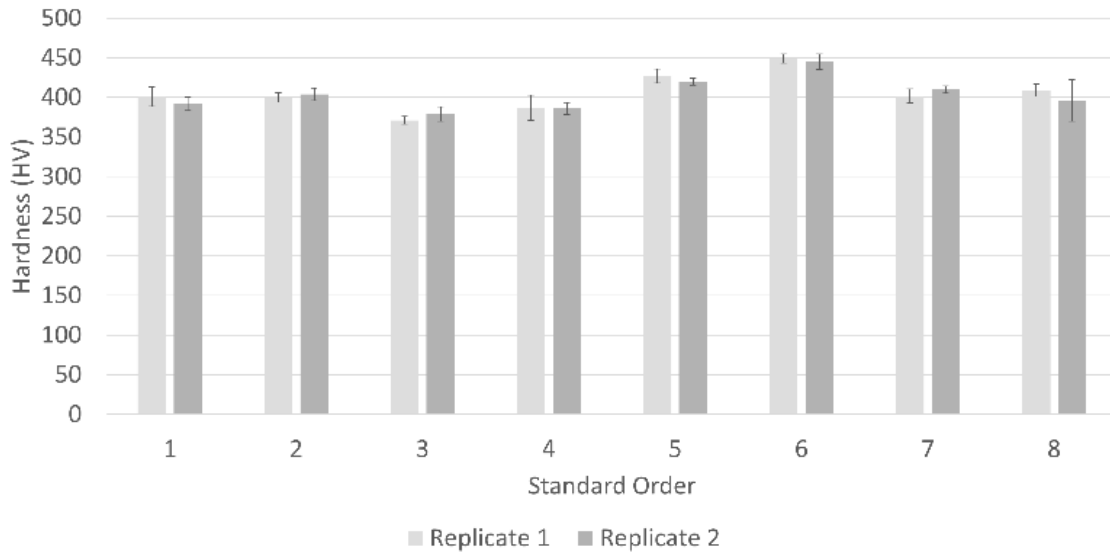


**Figure 6-3:** Hardness variation between replicates.

To check the variability of the furnace, two samples were placed at the same time next to the furnace thermocouple and their hardness responses were compared. Those samples were treated as replicates for each set of the different factor level combinations. In all 8 conditions, hardness variations did not exceed 3% of difference, verifying that the furnace is reliable for reproducible results if the samples are close to the thermocouple.

#### *Taguchi design analysis*

When using Taguchi's design, the ultimate goal is the identification of the factors that can be controlled, which can reduce the variability of a process by reducing the effects of uncontrollable factors, which are also called noise factors <sup>[21]</sup>. Having higher values of the signal-to-noise ratio (S/N) is desirable, as it determines which control factor settings can minimize the effects of the noise factors. The mean is the average response for each combination of control

factor levels. For parts manufacturing, the goal is to determine which factor level combinations would minimize the mean.

Minitab software provided an estimation of regression coefficients table for the signal-to-noise ratio (S/N) and the means. Using the p-values, the factors that were statistically significant were determined. The coefficients were used to determine relative importance of each factor in the model based on their absolute value. For S/N ratios and level of significance 0.10 factors A and B were statistically significant with p-values 0.056 and 0.067 respectively. Similarly, for the means, the same factors were statistically significant with p-values 0.069 for cooling rate and 0.082 for hold temperature. Generally, S/N ratios are preferably maximized in order to get more signal than noise, therefore as can be seen in Fig.6-4, the best conditions for minimizing the hardness would be the highest – low level of factor A and C and high level for factor B and D.

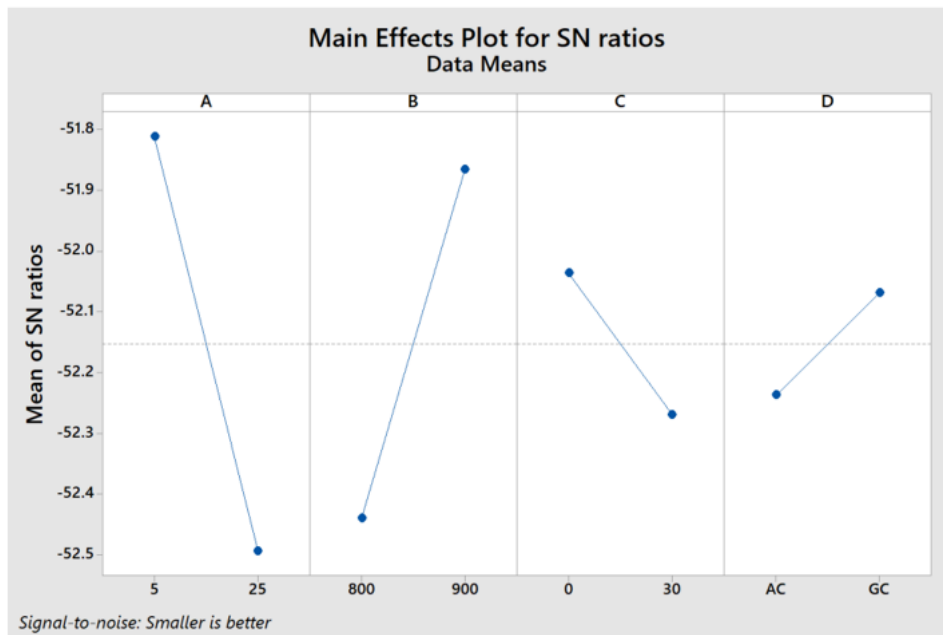


**Figure 6-4:** Main effects plot for S/N ratios.

On the contrary, for the means, the interest would be to minimize the response and therefore the best conditions are the lowest in Fig.6-5 which are the same factor levels as the S/N ratios.

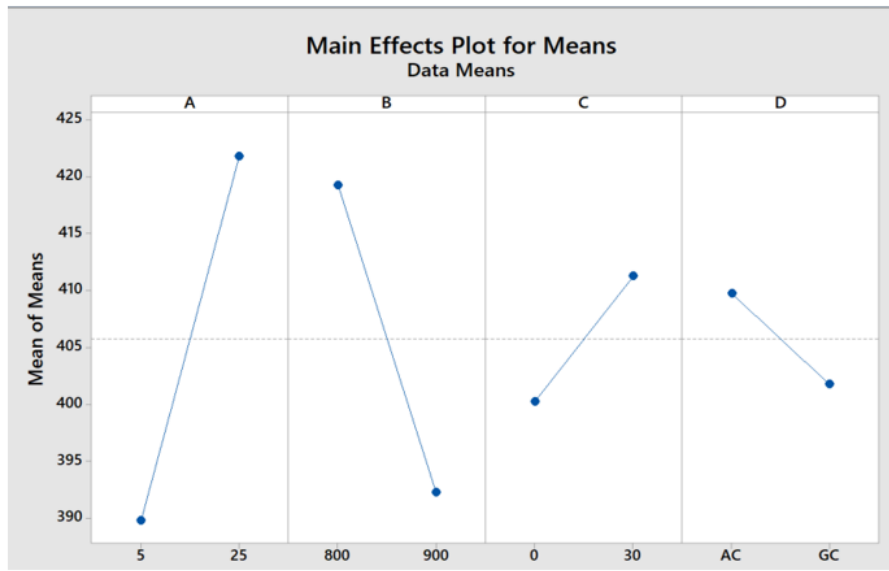


**Figure 6-5:** Main Effects plot for Means.

As mentioned above, the factors with the largest coefficients have the largest impact on a given response characteristic. From both responses (S/N and means) the following order of factors impact the outcome from highest to lowest: cooling rate, hold temperature, hold time, cooling to room temperature, interaction of the level of cooling rate with the level of temperature and lastly interaction of level of hold temperature with level of hold time.

From the positive or negative sign in front of the factor coefficients seen in Table 6-3, it can be concluded that cooling rate, hold time and interaction between cooling rate and hold temperature have a positive effect. Hold temperature, cooling method to room temperature and interaction between hold temperature and hold time have a negative effect.

**Table 6-3:** Estimated Model Coefficients for S/N ratios.

Term	Coefficient	P-value
Constant	-52.1523	0.000
A	0.3408	0.056

<b>B</b>	-0.2871	0.067
<b>C</b>	0.1164	0.161
<b>D</b>	-0.0844	0.219
<b>A*B</b>	0.0465	0.366
<b>B*C</b>	-0.0128	0.745

Similarly, for the means in Table 6-4, since the goal is to be minimized, the signs of the factors would indicate their effect; therefore, cooling rate, hold time and interaction between cooling rate and hold temperature should be decreased (i.e., the slower the cooling rate, the lower the hardness). Also, hold temperature, cooling method to room temperature and interaction between hold temperature and hold time should be increased to achieve the lowest means (i.e. the higher the temperature the lower the hardness).

**Table 6-4:** Estimated model coefficients for means.

<b>Term</b>	<b>Coefficient</b>	<b>P-value</b>
<b>Constant</b>	405.750	0.003
<b>A</b>	-16.000	0.069
<b>B</b>	13.500	0.082
<b>C</b>	-5.500	0.196
<b>D</b>	4.000	0.263
<b>A*B</b>	-2.750	0.361
<b>B*C</b>	0.250	0.910

*Regression analysis on Taguchi results*

A separate regression analysis on hardness results is presented on Table 6-5. With DF, degrees of freedom are annotated. The degrees of freedom show how much information a term of the equation uses. Adj SS is the adjusted sums of squares which are measures of variation for different components of the model [21]. Adj MS is the adjusted mean squares which measure how much variation a term or a model explains, assuming that all other terms are in the model, regardless of the order they were entered. The F-value is the test statistic used to determine whether the term is associated with the response [15]. The p value is a probability and if it is less than the alpha level, the results are statistically significant. From Table 6-5, only factor B (hold temperature) is significant for level of significance 0.05 (more accurate than the S/N and means of the Taguchi analysis) with p-value 0.004. Interactions between factors are again not considered significant.

**Table 6-5:** Regression analysis on Taguchi results.

<b>Source</b>	<b>DF</b>	<b>Adj SS</b>	<b>Adj MS</b>	<b>F-Value</b>	<b>P-Value</b>
<b>Regression</b>	6	1319083	219847	226.30	0.004
<b>A</b>	1	3795	3795	3.91	0.187
<b>B</b>	1	218584	218584	225.00	0.004
<b>C</b>	1	601	601	0.62	0.514
<b>D</b>	1	101	101	0.10	0.777
<b>A*B</b>	1	3313	3313	3.41	0.206
<b>B*C</b>	1	549	549	0.56	0.531
<b>Error</b>	2	1943	971		
<b>Total</b>	8	1321026			

Two equations depending on the cooling method to room temperature can be derived based on the first replicate hardness data:

$$\text{AC: HV} = 0.0 + 25.5 A + 0.4446 B + 8.6 C - 0.0280 A*B - 0.0097 B*C$$

$$\text{GC: HV} = -7.1 + 25.5 A + 0.4446 B + 8.6 C - 0.0280 A*B - 0.0097 B*C$$

Based on the absolute value of the coefficients, cooling rate seems to have relatively higher impact than the other two factors and the interactions for both equations. To verify the accuracy of those equations, two heat treatments were conducted, one for AC and one for GC. For the air cooled equation the heat treatment was annealing at 1095°C for 30 minutes, cool down to 1050°C with 1°C/min cooling rate and air cool (A=1, B=1050, C=0). For the gas quenched equation, the heat treatment was annealing at 1095°C for 30 minutes, cool down to 700°C with 1°C/min cooling rate and gas quench (A=1, B=700, C=0). The first heat treatment had a prediction of 463 HV and the actual value was 443±17 HV. For the GC sample, the prediction was 310 ±13 HV and the actual average value was 365HV. Since gas quenching requires a few seconds in the air after the sample is out of the furnace, it is logical the AC equation would be more accurate than the GC. Furthermore, some of the levels of the variables that were chosen for verification, were out of range of the original levels i.e., 1050°C and 700°C hold temperature in an attempt to see the predictability of the equations outside of the range of the levels tested.

In summary, the experimental factor levels as well as the optimum conditions for hardness reduction are presented in the Table 6-6:

**Table 6-6:** Summary of factor levels.

<b>Factors</b>	<b>Low level</b>	<b>High level</b>	<b>Optimum level</b>
A: cooling rate from 1095°C	5 °C/min	25 °C/min	5 °C/min
B: hold temperature	800 °C	900 °C	900 °C
C: time at hold temperature	0 min	30 min	0 min
D: cooling method to room temperature	Air cool	Gas quench	Gas quench

Microstructural analysis  
*As received condition*

The as-received (deformed) sample was microstructurally characterized and all hardness results after heat treatment were compared with the hardness of the as-received alloy, which is  $490 \pm 18$  HV. At low magnification in Fig.6-6, a high volume fraction of primary  $\gamma'$  can be observed at the grain boundaries. The size range is 1-5 $\mu$ m. The white phases are (Mo,W) carbides and/or borides, which, in BSE contrast, appear brighter than the  $\gamma'$  precipitates and their average size is  $1.4 \pm 0.5 \mu\text{m} \times 1.6 \pm 0.6 \mu\text{m}$ . EDS analysis confirmed that the precipitates are rich in Ni,Co and Ti,Al with a ratio that matched the  $(\text{Ni,Co})_3(\text{Al,Ti})$  whereas the matrix has less Ni and more Cr. The morphology of secondary  $\gamma'$  in the as received condition is cuboidal and spheroidal, with average size of  $439 \pm 49 \text{ nm} \times 396 \pm 39 \text{ nm}$  and  $225 \pm 51 \text{ nm} \times 199 \pm 41 \text{ nm}$  respectively as can be seen in Fig.6-7. No tertiary  $\gamma'$  was observed at high magnifications. The high hardness of the as received material is a result mainly from primary and secondary  $\gamma'$  precipitation as well as work hardening from the deformation process.

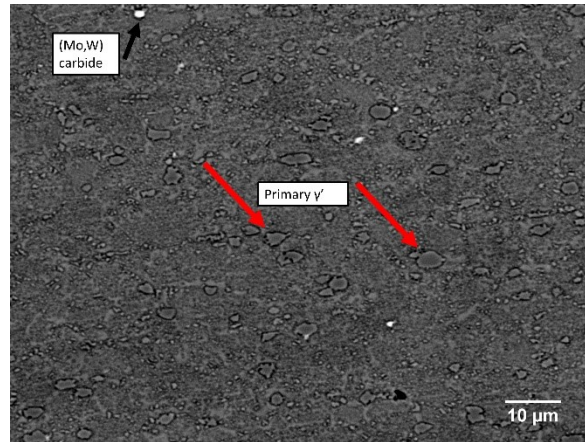


**Figure 6-6:** As received sample at low magnification. Red arrows indicate example positions of primary  $\gamma'$ .

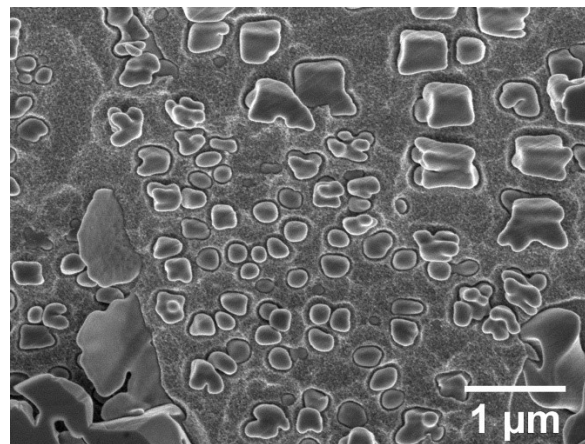


**Figure 6-7:** As received sample at higher magnification, highlighting secondary  $\gamma'$  in cuboidal and spheroidal morphologies.

The highest hardness (449HV) was achieved by 25°C/min cooling rate from 1095°C to 800°C, hold for 30 minutes and then air cooling. A significantly smaller volume fraction of primary  $\gamma'$  can be observed at low magnification in Fig.6-8 as well as grain coarsening, which has a direct correlation since primary  $\gamma'$  has a pinning effect. In Fig. 6-9, intergranular secondary  $\gamma'$  is observed in cuboidal/irregular morphology. The average size is  $357\pm 169$  nm X  $316\pm 139$  nm. The high standard deviation is caused by the large range of precipitate sizes. Compared with the as received condition, secondary  $\gamma'$  after this heat treatment is smaller than the cuboidal shape precipitates of the as-received but larger than the spheroidal morphology. Located around the primary  $\gamma'$ , as well

as within the  $\gamma$  matrix, a significant volume fraction of tertiary  $\gamma'$  is observed. This size was too small to accurately measure (tens of nm). Tertiary  $\gamma'$  is contributing to the final hardness by impeding dislocation motion [13].

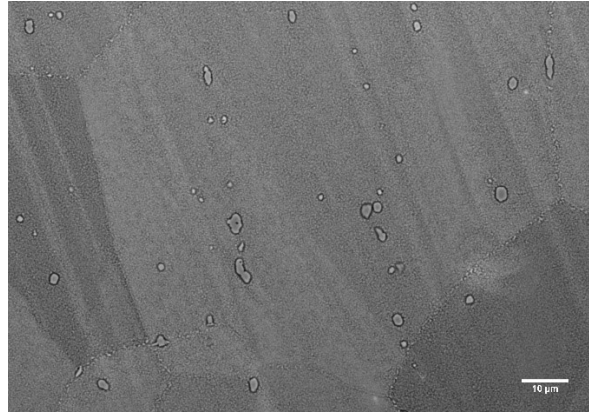


**Figure 6-8:** Hardest sample at low magnification. This was achieved by 25°C/min cooling rate from 1095°C to 800°C, hold for 30 minutes and then air cooling. Primary  $\gamma'$  is highlighted at the grain boundaries.

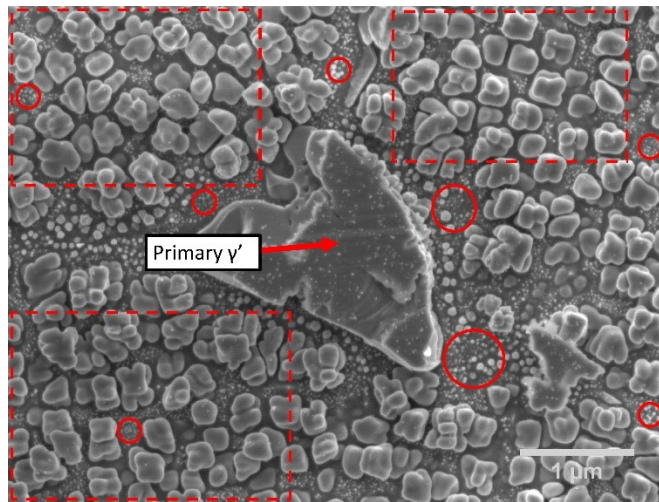


**Figure 6-9:** Hardest sample at high magnification. This was achieved by 25°C/min cooling rate from 1095°C to 800°C, hold for 30 minutes and then air cooling. Primary  $\gamma'$  (red arrow) is surrounded by tertiary  $\gamma'$ . Secondary (squares) and tertiary  $\gamma'$  (circles) are present intergranular.

The lowest hardness (371HV) was achieved by 5°C/min cooling rate from 1095°C to 900°C, no hold and then gas quenching. Primary  $\gamma'$  is present again along the grain boundaries as

can be seen in Fig.6-10. In higher magnification (Fig.6-11), detailed morphology of secondary  $\gamma'$  precipitates can be observed. In this sample, agglomerates of cuboidal secondary  $\gamma'$  seem to form within the grains. No tertiary  $\gamma'$  was observed at this sample within the grains. The average size of the agglomerate secondary  $\gamma'$  precipitation is  $793\pm 307$  nm X  $745\pm 306$  nm. The range of morphologies leads to a large standard deviation.

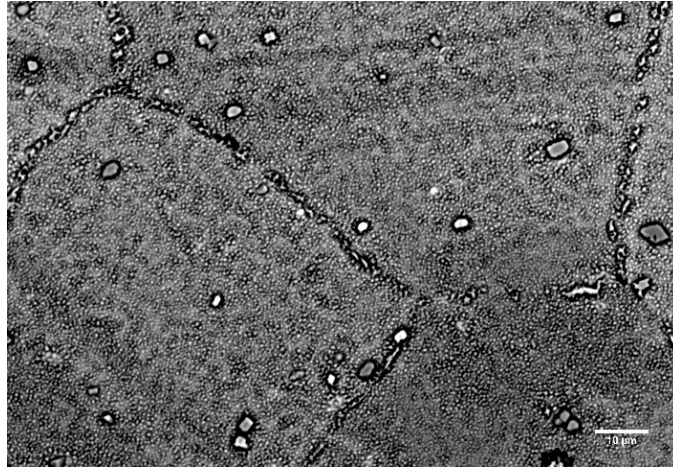


**Figure 6-10:** Softest sample at low magnification. This was achieved by  $5^{\circ}\text{C}/\text{min}$  cooling rate from  $1095^{\circ}\text{C}$  to  $900^{\circ}\text{C}$ , no hold and then gas quenching. Primary  $\gamma'$  is highlighted along the grain boundaries.

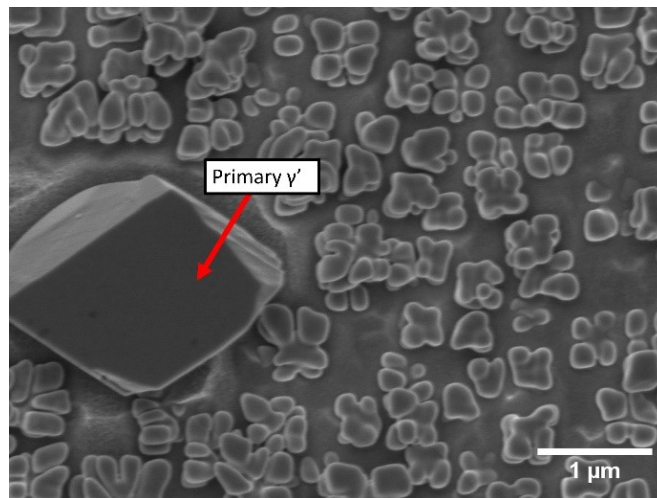


**Figure 6-11:** Softest sample at high magnification. This was achieved by  $5^{\circ}\text{C}/\text{min}$  cooling rate from  $1095^{\circ}\text{C}$  to  $900^{\circ}\text{C}$ , no hold and then gas quenching. Secondary  $\gamma'$  agglomerations are present intergranular. Tertiary  $\gamma'$  was observed close to primary  $\gamma'$  (red arrow) in a very small volume fraction.

The difference in hardness between the softest and the hardest sample derives from the presence of tertiary  $\gamma'$  and the size of secondary  $\gamma'$ . Initially, the deformed sample has a bimodal precipitate distribution as well as a work hardening effect. To achieve a high hardness, fast cooling rate from annealing temperature and air cooling to room temperature is applied. Since annealing is subsolvus, not all primary  $\gamma'$  is dissolved; some of it remains to pin grain boundaries and the  $\gamma'$  formers from the dissolved precipitates will reprecipitate as secondary and tertiary  $\gamma'$  at lower temperatures. The fast cooling rate does not facilitate diffusion of secondary  $\gamma'$  former elements and the 30- minute hold at 800°C is helping to grow the existing precipitates. Through air cooling, tertiary  $\gamma'$  is forming at lower temperatures and, since most of the precipitates are already formed, the driving force for growth (via further precipitation) is very small, therefore these are numerous but small (tens of nm) and spherical. Therefore, when tertiary  $\gamma'$  is present, the hardness is increasing since the precipitates mechanism are more effective in hindering dislocation motion.

On the contrary, for the softest sample, a slow cooling rate was applied and a gas quench. With slow cooling rate and no hold, more diffusion is possible and this is probably causing the agglomerates to form. The gas quench towards room temperature is suppressing the further nucleation of tertiary  $\gamma'$  that was observed at the air-cooled sample.

For further confirmation of the significance of the effect of hold temperature, the other two heat treatment combinations, apart from the softest sample that had the high level of the hold temperature parameter (900°C), were microstructurally characterised. The eighth heat treatment combination had the largest variation between the two replicates and was intentionally omitted from further analysis.

In the first case (the fourth heat treatment combination) the differences with the softest sample was 30 minutes hold instead of no hold and air cool instead of gas quench. The

microstructure at high magnification revealed the agglomerates that were observed in the softest sample and no tertiary  $\gamma'$  was observed (Fig.6-12). The size of the agglomerates was  $526 \pm 157$  nm X  $613 \pm 171$  nm, which is finer than the softer sample. This could explain the slight difference in hardness between the softest sample and the fourth heat treatment combination (387 HV instead of 371HV). A small volume fraction of tertiary  $\gamma'$  was observed in the sample around primary  $\gamma'$ .

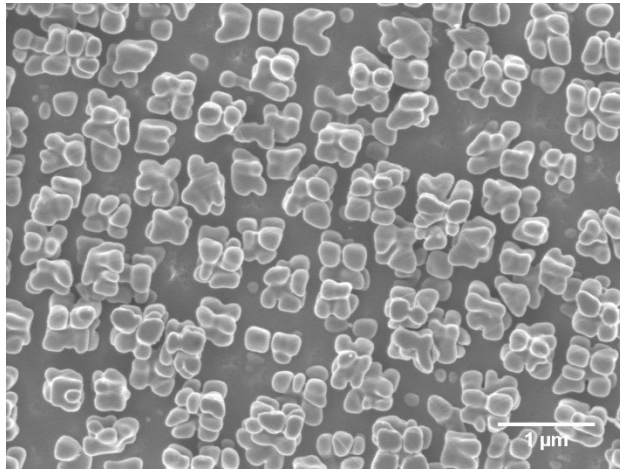


**Figure 6-12:** Comparison with other samples that were held at 900°C. This was achieved by 5°C/min cooling rate from 1095°C to 900°C, 30-minute hold and then air cooling. Secondary  $\gamma'$  agglomerations are present in this sample as well.

In the second case (the seventh heat treatment combination) the differences with the softest sample condition were higher cooling rate and air cooling instead of gas quenching. With higher cooling rate, fewer agglomerates are present and secondary  $\gamma'$  can also be observed as cuboidal particles (Fig.6-13). The average size of secondary  $\gamma'$  is  $242 \pm 66$  nm X  $247 \pm 54$  nm which is approximately 500 nm smaller. Furthermore, tertiary  $\gamma'$  was observed around primary  $\gamma'$ , which supports the hypothesis that tertiary  $\gamma'$  is forming during air cooling at lower temperatures. With a combination of smaller secondary  $\gamma'$  and the presence of tertiary  $\gamma'$ , the difference in hardness is +31 HV (from 371 HV in the softest sample the seventh heat treatment combination has a 402 HV hardness value).

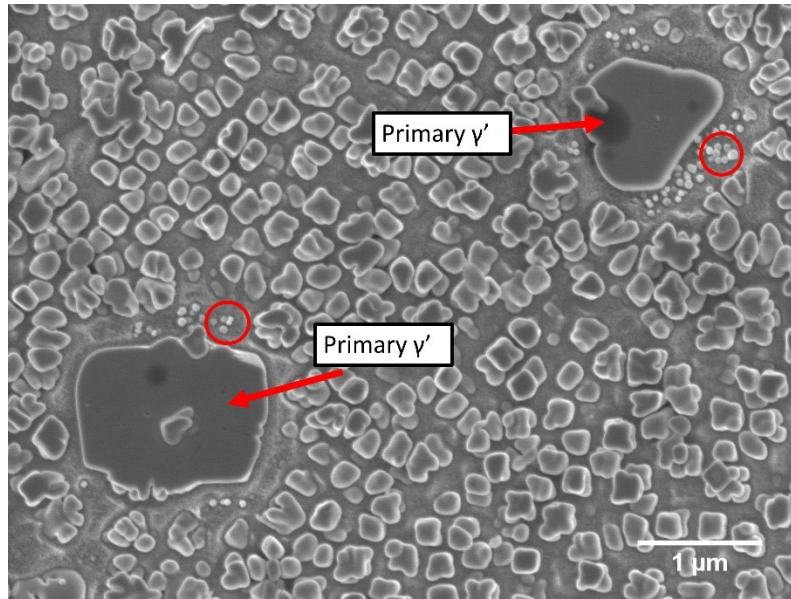


**Figure 6-13:** Comparison with other samples that were held at 900°C. This was achieved by 25°C/min cooling rate from 1095°C to 900°C, no hold and then air cooling. Smaller secondary  $\gamma'$  as well as tertiary  $\gamma'$ (circles) around primary  $\gamma'$  (red arrows) are present in this sample.

According to the microstructural analysis of the four heat treatment combinations, the effect of secondary  $\gamma'$  size as well as the volume fraction of tertiary  $\gamma'$  are the main variables that were affecting hardness. Compared to [12], where higher cooling rates resulted in smaller precipitate size, the trend of the results agree, although in [12] the heat treatment was continuously cooled from solution annealing temperature to room temperature, whereas in this work, furnace cooling is applied till a higher hold temperature. On the contrary, in this work tertiary  $\gamma'$  was mainly observed at high cooling rates although the comparison is not again exact as the slowest cooling rate (0.1K/s) in [12] would contribute to longer time in the furnace than in this work (25°C/min until 800/900°C). The hold temperature of 900°C that was determined from statistical analysis did not result in the formation of agglomerates in all cases. A combination of all four factors results in the final microstructure, although 900°C is proven to result in lower hardness in most cases. Further microstructural analysis on designs with higher range of factor level combinations will aid the understanding of the precipitation kinetics of the three sizes as well as further importance of other

design factors (i.e. cooling rate). Ultimately, stress-strain curves will be obtained to fully describe understand the effect of heat treatment on mechanical properties.

#### **6.4 Conclusions**

Taguchi's L8 matrix was successfully used to design a heat treatment plan for manufacturing of Rene 65 parts. Regression analysis on the results revealed that the most significant factor for this design is hold temperature. The softest sample and the hardest sample have significant microstructural differences, with the latter having a trimodal distribution of precipitates, which is believed to increase the strength. Further investigation on microstructural characteristics will be conducted in the future along with mechanical testing to determine the mechanical properties.

#### **6.5 Acknowledgments**

Financial support from the Natural Science and Engineering Council of Canada, GE Aviation, Bromont, Quebec Canada, the Consortium de Recherche et D'innovation en Transformation Métallique and the McGill Engineering Doctoral Award (to C.M. Katsari) is gratefully acknowledged. The authors would like to thank Mr. Martin Therer from GE Aviation, Bromont for his valuable insights on this work.

#### **6.6 References**

1. Durand-Charre, M., *The microstructure of superalloys*. 1998: CRC press.
2. Matthew J. Donachie and S.J. Donachie, *Superalloys A Technical Guide*. 2002.
3. Sims, C.T., *A history of superalloy metallurgy for superalloy metallurgists*. Superalloys, 1984. 1984: p. 399-419.
4. Sims, C.T., N.S. Stoloff, and W.C. Hagel, *superalloys II*. 1987: Wiley New York.

5. Reed, R.C., *The superalloys: fundamentals and applications*. 2008: Cambridge university press.
6. A. Heaney, J., et al., *Development of a New Cast and Wrought Alloy (René 65) for High Temperature Disk Applications*. 2014. p. 67-77.
7. Andrew, W., et al. *Thermal Stability of Cast and Wrought Alloy Rene 65*. in *Superalloys 2016: Proceedings of the 13th International Symposium of Superalloys*. Wiley Online Library.
8. Bond, B.J., et al. *Rene 65 billet material for forged turbine components*. in *8th International Symposium on Superalloy 718 and Derivatives 2014, September 28, 2014 - October 1, 2014*. 2014. Pittsburgh, PA, United states: John Wiley and Sons Inc.
9. Katsari, C., et al., *Precipitation Characteristics of Gamma Prime Precipitate in Rene 65*. 2017.
10. Katsari, C.M., et al., *Microstructural Characterization and Mechanical Properties of Rene 65 Precipitates*, in *Proceedings of the 9th International Symposium on Superalloy 718 & Derivatives: Energy, Aerospace, and Industrial Applications*, E. Ott, et al., Editors. 2018, Springer International Publishing Ag: Cham. p. 629-641.
11. Charpagne, M.A., et al. *Heteroepitaxial Recrystallization Observed in René 65™ and Udimet 720™: A New Recrystallization Mechanism Possibly Occurring in All Low Lattice Mismatch  $\gamma$ - $\gamma'$  Superalloys* in *Superalloys 2016: Proceedings of the 13th International Symposium of Superalloys*. 2016. Wiley Online Library.
12. Wojcik, T., M. Rath, and E. Kozeschnik, *Characterisation of secondary phases in Ni-base superalloy Rene 65*. *Materials Science and Technology*, 2018. 34(13): p. 1558-1564.
13. Jackson, M.P. and R.C. Reed, *Heat treatment of UDIMET 720Li: the effect of microstructure on properties*. *Materials Science and Engineering: A*, 1999. 259(1): p. 85-97.

14. Czitrom, V., *One-Factor-at-a-Time versus Designed Experiments*. The American Statistician, 1999. 53(2): p. 126-131.
15. Berger, P.D., R.E. Maurer, and G.B. Celli, *Introduction to Experimental Design*, in *Experimental Design*. 2018, Springer. p. 1-19.
16. Taguchi, G., S. Konishi, and S. Konishi, *Taguchi Methods: Orthogonal Arrays and Linear Graphs. Tools for Quality Engineering*. 1987: American Supplier Institute Dearborn, MI.
17. Singh, A., et al., *Influence of cooling rate on the development of multiple generations of  $\gamma'$  precipitates in a commercial nickel base superalloy*. Materials characterization, 2011. 62(9): p. 878-886.
18. Mitchell, R., et al., *The influence of cooling rate from temperatures above the  $\gamma'$  solvus on morphology, mismatch and hardness in advanced polycrystalline nickel-base superalloys*. Materials Science and Engineering: A, 2008. 473(1-2): p. 158-165.
19. Laurence, A., et al. *Impact of the solution cooling rate and of thermal aging on the creep properties of the new cast wrought Rene 65 Ni-based superalloy*. in *8th International Symposium on Superalloy 718 and Derivatives 2014, September 28, 2014 - October 1, 2014*. 2014. Pittsburgh, PA, United states: John Wiley and Sons Inc.
20. Singh, A.R.P., et al., *Mechanisms related to different generations of  $\gamma'$  precipitation during continuous cooling of a nickel base superalloy*. Acta Materialia, 2013. 61(1): p. 280-293.
21. *Minitab 18 Support - Taguchi designs*. 2019.

# Chapter 7 : Heat treatment optimization of a $\gamma'$ strengthened nickel-based superalloy based on Central Composite Design

## Preface

With Taguchi design in Chapter 6, hold time was found to be the most significant factor affecting hardness. Since with this design quadratic terms could not be measured and the experiments were small in number, in Chapter 7 Central Composite Design was used. This design allowed calculation of quadratic terms and with 40 runs of experiments the lowest point within the range of the parameters' levels could also be predicted from the regression equations. The samples in this chapter were in two conditions: deformed and deformed and annealed. A few interesting microstructural features were observed for the first time in this alloy.

This Chapter has been published in Metallurgical and Materials Transactions A journal as Katsari, C.M., Wessman, A. & Yue, S. Heat Treatment Optimization of a  $\gamma'$ -Strengthened Nickel-Based Superalloy Based on Central Composite Design. *Metall Mater Trans A* (2020). <https://doi.org/10.1007/s11661-020-05948-1> <sup>[4]</sup> and licence to be reused in this thesis has been granted from Springer Nature.

## Abstract

Thermomechanical processing of blades and disks can become challenging when the microstructure of the material consists of a high volume fraction of strengthening phases. In Rene 65 the precipitate volume fraction is 40 % in the as forged condition. The microstructure consists of a bimodal/trimodal  $\gamma'$  precipitate distribution on the grain boundaries and intergranularly. In order to control grain size and *reduce* hardness, primary  $\gamma'$  should be present on the grain boundaries and the secondary and tertiary precipitates should be coarse. In this work an attempt to optimize the heat treatments that coarsen those two populations by implementing tools from experimental design is attempted. Two sample categories were examined with different thermomechanical histories, one deformed and one deformed and annealed, in order to verify if the ultimate heat treatment can be applied at different processing steps. The results confirm that there is a definite effect of the original microstructure, since there were different heat treatments that were proven to be the most effective to reduce hardness for the two conditions. Microstructural analysis revealed precipitate splitting and coralloid microstructures were observed for the first time in this alloy. Two mechanisms are proposed for the reduction of hardness depending on the initial microstructure.

**Keywords:** Rene 65, heat treatments, central composite design, hardness, gamma prime, splitting

## 7.1 Introduction

Rene 65 is a recently developed nickel-based superalloy by General Electric and ATI Allvac that is used for manufacturing compressor blades and disks. It is designed to perform at temperatures up to 750°C due to the stability of gamma prime ( $\gamma'$ ) precipitation <sup>[1-3]</sup>. Therefore, it can exceed the temperature capabilities (650°C) of Inconel 718, the most commonly used nickel-based superalloy in various applications, which is not only strengthened by  $\gamma'$  but also by

metastable  $\gamma'$ . It is also worth mentioning that the production of Rene 65 is less costly than the powder metallurgy route of R88DT, its predecessor with a similar chemistry [3].

As mentioned before, the microstructure of Rene 65 contains  $\gamma$  (Ni) matrix and  $\gamma'$  -  $\text{Ni}_3(\text{Al,Ti})$  precipitates, which can be found in three different sizes [1,4]. The larger size is called primary  $\gamma'$  and serves the purpose of pinning the grain boundaries, which prevents grain coarsening and thereby increases fatigue resistance [3]. Its size is usually in the scale of a few microns. Secondary and tertiary  $\gamma'$  are found intergranularly in hundreds and tens of nm respectively [3,5,6]. They contribute to the strength and creep resistance of the alloy [2]. Secondary  $\gamma'$  can be found in various morphologies whereas tertiary is mainly observed in spherical particles. A representative microstructure of a heat-treated sample highlighting the trimodal distribution is presented in Fig. 7-1 as a reference. The mechanical properties depend directly on the size and volume fraction of the hardening precipitates [7]. In many cases, the secondary and tertiary  $\gamma'$  precipitates make the material so hard that it negatively impacts the ability to successfully form Rene 65 in thermomechanical processing [8].

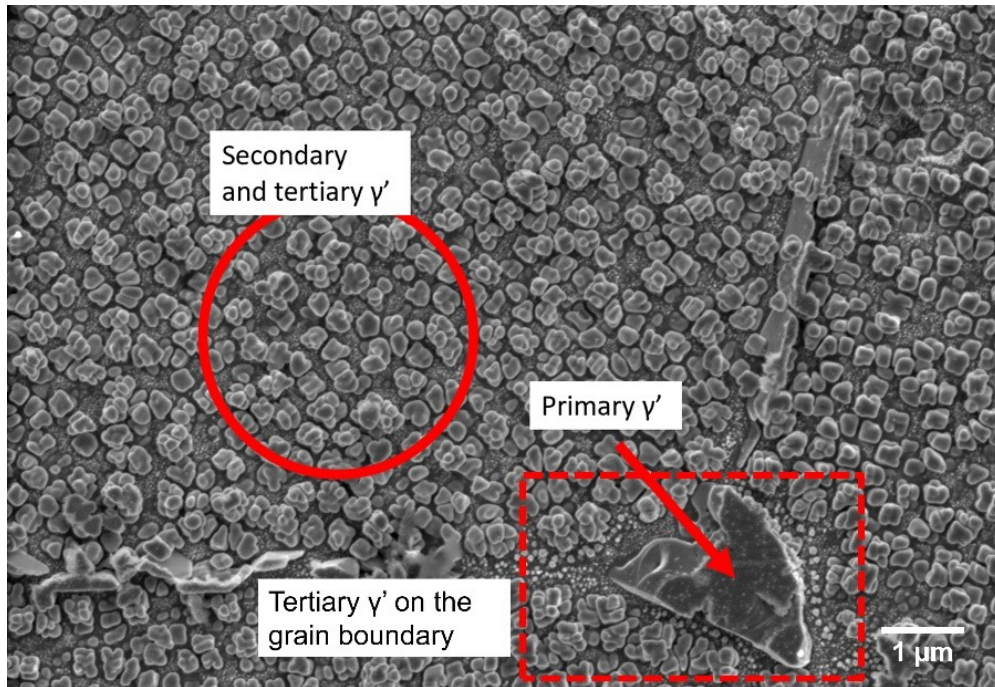


**Figure 7-1:** Trimodal distribution of  $\gamma'$  precipitates in Rene 65. Primary  $\gamma'$  is present on the grain boundaries (arrow), secondary and tertiary  $\gamma'$  can be found intragranularly (circle) and tertiary  $\gamma'$  is also present around primary  $\gamma'$  (square).

From previous experimental work on heat treatments for manufacturing of parts made of Rene 65 [5, 9], it was observed that the proposed heat treatment schedule was effective since the as received hardness was reduced. This involved sub-solvus annealing followed by furnace cooling to a lower temperature and a hold for various times followed by water quenching or air cooling (similar to Fig. 7-3 of this paper's heat treatment plan). In that work, only one factor (hold time) was varied to determine the effect on hardness (one-factor-at-a-time (OFAT) approach), which is proven not to have the ability to consider interactions between factors and therefore did not give the ultimate combination of factors for hardness reduction. Following that work [6], Design of Experiments tools, more specifically the Taguchi design, were used in an attempt to understand which parameters affect the reduction in hardness, as well as the effect of some of the interactions among the parameters. The four parameters that were examined were cooling rate from annealing temperature to hold temperature, hold temperature, hold time and cooling method from hold

temperature to room temperature. Regression analysis on the results showed that only hold temperature had a statistically significant effect. Based on [2], cooling rate affects the morphology and size distribution of precipitates which would then affect the hardness. Therefore, in this work an attempt to model the aforementioned results more accurately by determining the quadratic terms and then finding the optimum heat treatment to give the lowest hardness possible is presented.

## 7.2 Experimental methods

Two initial microstructural conditions are examined, one deformed (D) and one deformed and annealed (DA), in order to evaluate the feasibility of the same design applied to different points of manufacturing. The D samples were cold deformed, and the DA were hot deformed and super-solvus annealed in the as received condition. Rene 65 samples of both conditions were provided by GE Aviation, Bromont. The nominal composition of the alloy in wt% [10] can be found in Table 7-1:

**Table 7-1:** Nominal chemical composition of Rene 65 (wt%)<sup>[10]</sup>.

<b>Ni</b>	<b>Co</b>	<b>Cr</b>	<b>Mo</b>	<b>W</b>	<b>Al</b>	<b>Ti</b>	<b>Nb</b>	<b>B</b>	<b>C</b>	<b>Zr</b>	<b>Fe</b>
<b>Bal.</b>	13	16	4	4	2.1	3.7	0.7	0.016	0.01	0.05	1

For the heat treatment design and analysis of experiments, Minitab software was used. The design was based on Response Surface Methodology (RSM), more specifically on Central Composite design (CCD). In an RSM design, a low level and a high level for each factor is decided. These factor levels define the cube corners around which the design is built [11]. Alpha ( $\alpha$ ) determines the distance of each axial point from the center. A value greater than unity puts them outside the cube, as can be seen in Fig.7-2. Minitab's  $\alpha$  values agree with those listed by Montgomery [12] and for this design the value of 1.68 was chosen from the software's default options [13]. By choosing this  $\alpha$ , the design includes orthogonal blocks that allow model terms and

block effects to be estimated independently, while minimizing the variance in the regression coefficients <sup>[13]</sup>. The number of experiments, as well as the combination of the levels of parameters tested, allow the estimation of the curvature of the design as well as calculation of the error, since some of the runs were with the same factor levels and are therefore replicates. For a prediction model, multiple replicates can increase the precision of the model as well as create the ability to detect smaller effects <sup>[11]</sup>. In this design for four factors, a sum of 16 cube points, 12 center points in the cube and 12 axial points created a total of 40 run design, which was performed for both samples with the same run order.

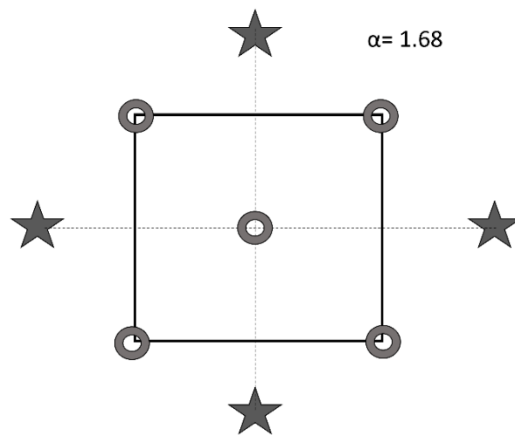


**Figure 7-2:** Central Composite Design points schematic: circle (cube) and star(axial) positions indicate the different factor levels in the design. For this experiment a sum of 16 cube points, 12 center points in the cube and 12 axial points created a total of 40 run design.

The four factors that were varied can be seen in Fig.7-3. Although the heat treatment parameters remained the same as <sup>[6]</sup>, their levels were expanded in order to capture the full range of available levels. The levels in <sup>[6]</sup> were based on previous experimentation as well as industrial applicability. In this work, for Factor A (furnace cooling rate from annealing temperature to hold temperature) low level - which was the optimum condition in <sup>[6]</sup>- was decreased to 1°C/min and

was constant at low values, while high level remained at 25°C/min since this is the maximum average cooling rate that the box furnace can achieve. The samples were 0.5 cm \* 0.5 cm squares and there was no thermal gradient. Factor B is the hold temperature and in [6] was, statistically, the most significant factor. Therefore, its levels were expanded as well on both sides with low value 700°C and high level 1000°C. Below 700°C from the TTT diagram [3] there is no precipitation. The high level was chosen as the maximum hold temperature where secondary  $\gamma'$  would not be completely dissolved as even higher temperatures are approaching the annealing temperature (1095°C). Full solvus curve can be seen in Fig. 7-4 from [14]. For the hold time (Factor C) the levels were kept the same as [6] since a maximum of 30 minutes is considered industrially applicable and, from previous work [6], Factor C was not significant. For Factor D, since, from [6], the high level (gas cooled (GC) samples) was the optimum condition, this was chosen as low level for this work and water quenching (WQ) as the high level, since it is an even faster method. It is worth mentioning that, as in [6], gas cooling was achieved by applying compressed air after the sample was out of the furnace. The parameters and their levels can be summarized in Table 7-2.

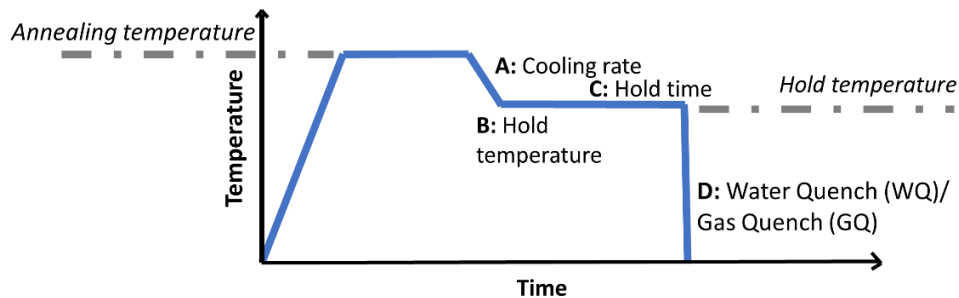


**Figure 7-3:** Heat treatment schematic.

**Table 7-2:** Factors' levels.

Factors	Low level	High level
A: cooling rate from 1095°C (°C/min)	1	25
B: hold temperature (°C)	700	1000
C: time at hold temperature (min)	0	30
D: cooling method to room temperature	Gas quenching (GC)	Water Quenching (WQ)

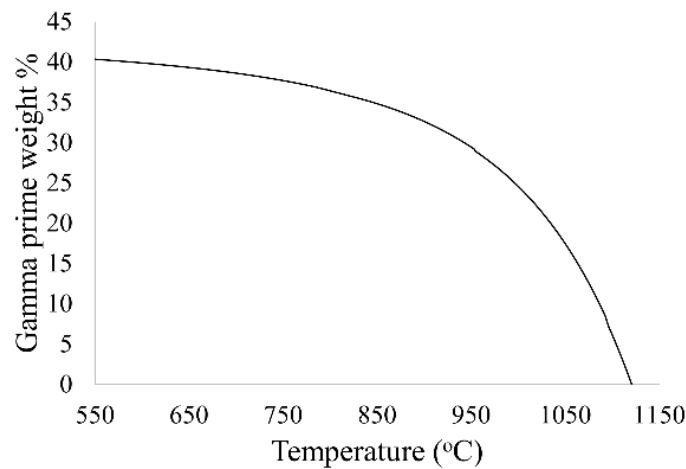


**Figure 7-4:** Solvus curve of  $\gamma'$  in Rene 65 (adapted in °C from <sup>[14]</sup>).

In order to determine the quadratic terms, a full quadratic model was used in the regression equation to fit all four terms (A, B, C, D), as main terms, their squares and the main interactions among them (excluding factor D). The results since factor D is a categorical factor are presented in two separate equations for each level in a generic form of:

$$D: HV = \text{Constant} + A + B + C + A * A + B * B + C * C + A * B + A * C + B * C$$

where A, B, C, D are replaced accordingly from Table 7-2.

Contour plots display a two-dimensional view in which points that have the same response value are connected to produce contour lines. In this design, these graphically represent the variation in hardness between two fixed parameters while varying the other two (i.e. the effect of cooling rate and hold temperature while keeping hold time and cooling method constant at 0 minutes and gas quench respectively).

For the heat treatments, a Sentro Tech box furnace with a Eurotherm 2408 process controller that allowed variation of Factor A, B and C was used. The temperature was monitored with the furnace thermocouple and the variability of the furnace gradient to the hardness was verified <sup>[6, 15]</sup> to be less than 3%.

The response that was measured for the design was Vickers microhardness as a fast and easy way of identifying the effect of heat treatment on mechanical properties. Furthermore, it was consistent with <sup>[6]</sup> to compare the lowest and highest points. A Clark CM-100AT micro-hardness tester equipped with CLEMEX CMT indent measurement software was used for the measurements. The indents were created with a force of 50gf at 15 sec dwell time and measured at a magnification of 500X in different regions of the samples.

For microstructural characterisation, a Hitachi Scanning Electron Microscope (SEM), SU8000, at 3kV was used for high resolution imaging coupled with Energy Dispersive Spectroscopy (EDS) at 10kV for qualitative analysis of  $\gamma'$  and matrix. To reveal the  $\gamma'$  precipitation under SEM conditions, the  $\gamma$  matrix was selectively removed by electropolishing and electroetching at 15V for 10 seconds and 5V for 5 seconds, respectively at room temperature. The etchant was methanol based (64% methanol and 30% ethylene glycol) with additions of perchloric acid (6%). The working distance for imaging was 12 mm and for EDS 20mm. For both imaging

and EDS analysis objective lens aperture was set to 2 and images were taken with the secondary electron detector. The samples were imaged up to x100K in order to confirm the presence of tertiary  $\gamma'$  (tens of nm precipitates), which would impact the hardness results analysis. Quantification of precipitate size was achieved by ImageJ image analysis software and the measurements were performed manually by drawing a line and measuring the X and Y values of the image on approximately 50 precipitates, where available, from five different regions (X and Y correspond to the horizontal and vertical axes of the image respectively). The average values are reported in X ( $\mu\text{m}/\text{nm}$ ) x Y( $\mu\text{m}/\text{nm}$ ) form.

### 7.3 Results

#### Statistical analysis

The combinations of factor levels as well as the average hardness responses with standard deviations for both sample conditions are presented in Table 7-3. The heat treatments were performed in the run order that is seen in Table 7-3, which was randomized. For the statistical analysis, only the average hardness values were used.

**Table 7-3:** Central Composite Design and responses in HV for deformed “D” sample condition and deformed and annealed “DA” sample condition.

<b>Run Order</b>	<b>A (<math>^{\circ}\text{C}/\text{min}</math>)</b>	<b>B(<math>^{\circ}\text{C}</math>)</b>	<b>C(min)</b>	<b>D (gas/water quench)</b>	<b>HV of “D” condition</b>	<b>HV of “DA” condition</b>
<b>0</b>	-	-	-	-	490±17	413±21
<b>1</b>	20	761	24	GQ	452±13	441±10
<b>2</b>	13	850	30	GQ	419±12	412±22

<b>3</b>	20	761	24	WQ	458±17	444±8
<b>4</b>	13	850	30	WQ	444±13	414±12
<b>5</b>	13	850	15	GQ	435±12	409±24
<b>6</b>	20	939	24	WQ	420±15	414±14
<b>7</b>	20	939	6	GQ	390±21	409±11
<b>8</b>	20	761	6	GQ	456±13	441±29
<b>9</b>	6	761	24	GQ	448±14	413±11
<b>10</b>	13	850	15	GQ	429±13	438±15
<b>11</b>	13	850	15	GQ	442±9	425±15
<b>12</b>	6	761	24	WQ	441±28	429±15
<b>13</b>	6	939	24	GQ	384±28	425±15
<b>14</b>	13	850	0	GQ	409±11	406±14
<b>15</b>	13	850	15	GQ	410±11	397±18
<b>16</b>	25	850	15	WQ	444±32	425±10
<b>17</b>	13	850	0	WQ	428±20	398±21
<b>18</b>	6	939	6	GQ	380±11	378±11
<b>19</b>	6	761	6	GQ	415±14	400±11

<b>20</b>	13	1000	15	WQ	349±23	361±15
<b>21</b>	13	850	15	WQ	421±20	405±13
<b>22</b>	6	761	6	WQ	416±20	425±6
<b>23</b>	13	850	15	WQ	437±11	410±10
<b>24</b>	20	761	6	WQ	449±27	423±8
<b>25</b>	1	850	15	GQ	368±11	378±14
<b>26</b>	13	850	15	WQ	419±14	421±15
<b>27</b>	13	700	15	GQ	417±17	432±18
<b>28</b>	20	939	6	WQ	423±11	409±15
<b>29</b>	13	850	15	WQ	446±16	431±11
<b>30</b>	13	850	15	WQ	443±11	400±12
<b>31</b>	25	850	15	GQ	445±14	415±16
<b>32</b>	1	850	15	WQ	387±14	347±15
<b>33</b>	20	939	24	GQ	412±18	374±10
<b>34</b>	13	1000	15	GQ	410±20	360±10
<b>35</b>	6	939	6	WQ	401±7	380±13
<b>36</b>	13	850	15	GQ	410±15	423±12

<b>37</b>	6	939	24	WQ	383±16	373±14
<b>38</b>	13	850	15	WQ	421±20	402±19
<b>39</b>	13	850	15	GQ	418±14	427±13
<b>40</b>	13	700	15	WQ	422±11	414±12

A regression analysis on the response surface design was performed using Minitab. The regression model included quadratic terms and it revealed that the most significant factors that affect the hardness response on the deformed sample were, in descending order, hold temperature, cooling rate and hold temperature squared, and were the only factors that had p-value of less than the 0.05 significance level in the ANOVA table. The p value is a probability and if it is less than the alpha level (0.05), the results are statistically significant. On the contrary, for the deformed and annealed sample only the hold temperature and cooling rate played a significant role in the outcome.

To investigate the independence of the residuals (observed error), the residuals versus order plot is used to verify the assumption that the residuals are independent from one another. Independent residuals show no trends or patterns when displayed in time order. In Figs. 7-5 and 7-6 it is clearly shown that there is no pattern or trend for either sample as the residuals on the plot fall randomly around the center line; i.e. there is no downward trend or a cycling phenomenon, indicating that the residuals are not correlated and therefore independent from one another.

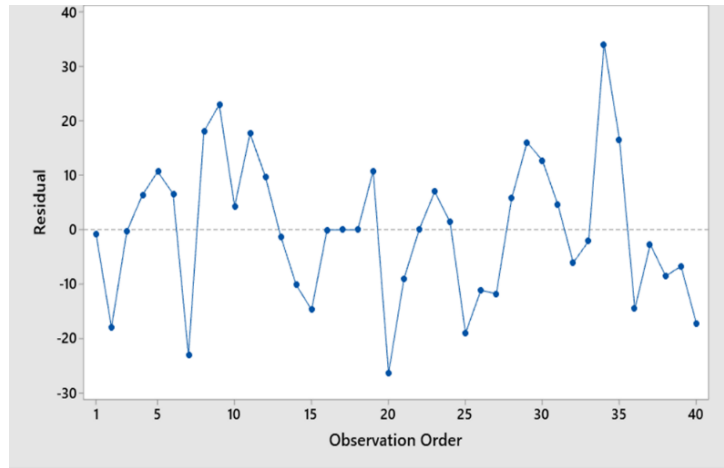


**Figure 7-5:** Residuals versus order plot for deformed sample. No particular trend is observed.

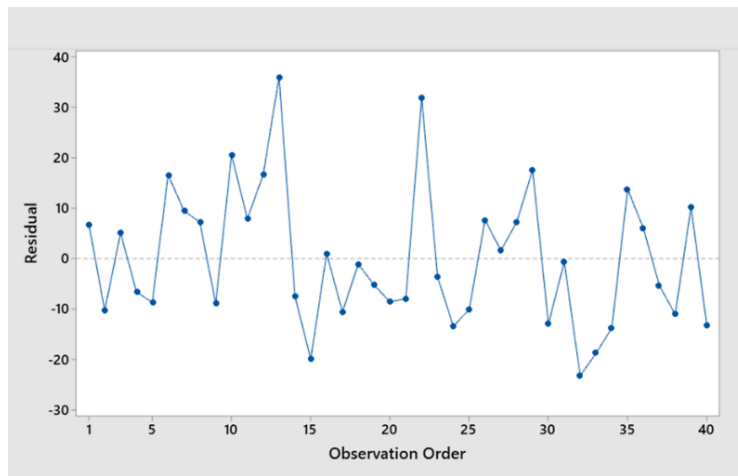


**Figure 7-6:** Residuals versus order plot for deformed and annealed sample. No particular trend is observed.

From the analysis, it is possible to generate two equations with uncoded variables depending on the cooling method to room temperature for each sample condition:

For the deformed sample:

$$\text{GQ: HV} = -254 + 4.54 \text{ Cooling rate} + 1.589 \text{ Hold Temperature} + 4.10 \text{ Hold Time} - 0.0792 \text{ Cooling rate} * \text{Cooling rate} - 0.001002 \text{ Hold Temperature} * \text{Hold Temperature} + 0.0145 \text{ Hold Time} * \text{Hold Time} + 0.00007 \text{ Cooling rate} * \text{Hold Temperature} - 0.0215 \text{ Cooling rate} * \text{Hold Time} - 0.00433 \text{ Hold Temperature} * \text{Hold Time}$$

WQ: HV = -215 + 4.46 Cooling rate + 1.555 Hold Temperature + 3.84 Hold Time - 0.0792 Cooling rate\*Cooling rate - 0.001002 Hold Temperature\*Hold Temperature + 0.0145 Hold Time\*Hold Time + 0.00007 Cooling rate\*Hold Temperature - 0.0215 Cooling rate\*Hold Time - 0.00433 Hold Temperature\*Hold Time

whereas for the deformed and annealed sample:

GQ: HV = -17 + 7.81 Cooling rate + 1.014 Hold Temperature + 2.99 Hold Time - 0.1092 Cooling rate\*Cooling rate - 0.000662 Hold Temperature\*Hold Temperature + 0.0042 Hold Time\*Hold Time - 0.00333 Cooling rate\*Hold Temperature - 0.0655 Cooling rate\*Hold Time - 0.00231 Hold Temperature\*Hold Time

WQ: HV = -33 + 8.89 Cooling rate + 1.011 Hold Temperature + 3.09 Hold Time - 0.1092 Cooling rate\*Cooling rate - 0.000662 Hold Temperature\*Hold Temperature + 0.0042 Hold Time\*Hold Time - 0.00333 Cooling rate\*Hold Temperature - 0.0655 Cooling rate\*Hold Time - 0.00231 Hold Temperature\*Hold Time

### **Contour plots**

For both samples the contour plots indicate, with a variance from red to green, the harder to softer predictions respectively. The plots indicate the variation of two variables while keeping the other two constant. The regions that are interesting for parts manufacturing are at the lower ends of the spectra for both cases (dark green). For the deformed samples that were gas quenched, the lowest values could be achieved by holding at the hold temperature for 15 minutes, low cooling rate and high hold temperature, which was the same trend for the water quenched samples, as can be seen in Fig.7-7 and Fig.7-8.

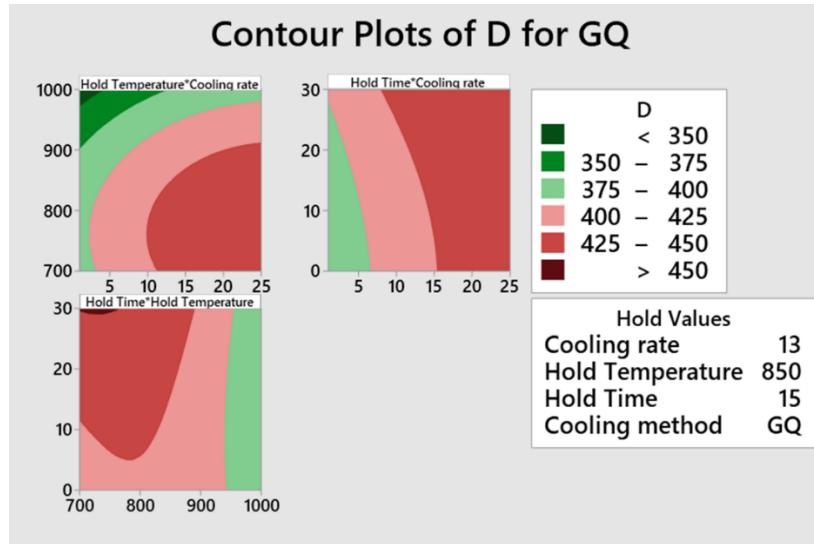


**Figure 7-7:** Contour plots for deformed (D) samples that were gas quenched to room temperature. Legends on top of plots are in the form Y axis \*X axis i.e. Hold Temperature (Y axis) \* Cooling rate (X axis). Hardness units in HV, cooling rate in °C /min, hold temperature in °C, hold time in min and GQ indicates gas quench.

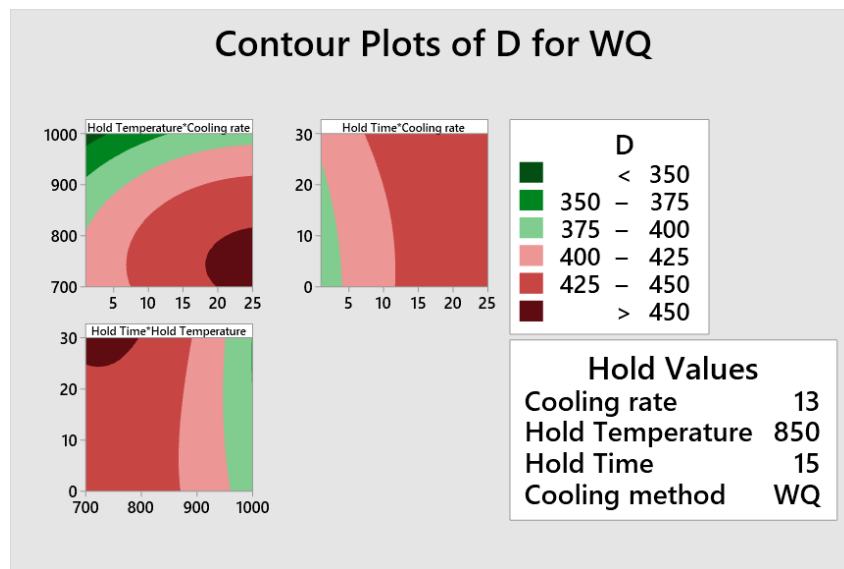


**Figure 7-8:** Contour plots for deformed (D) samples that were water quenched to room temperature. Legends on top of plots are in the form Y axis \*X axis i.e. Hold Temperature (Y axis) \* Cooling rate (X axis). Hardness units in HV, cooling rate in °C /min, hold temperature in °C, hold time in min and WQ indicates water quench.

For the deformed and annealed samples (Fig.7-9 and 7-10) the factor level trend is similar to the deformed samples but lower hardnesses are possible for the water quenched samples.

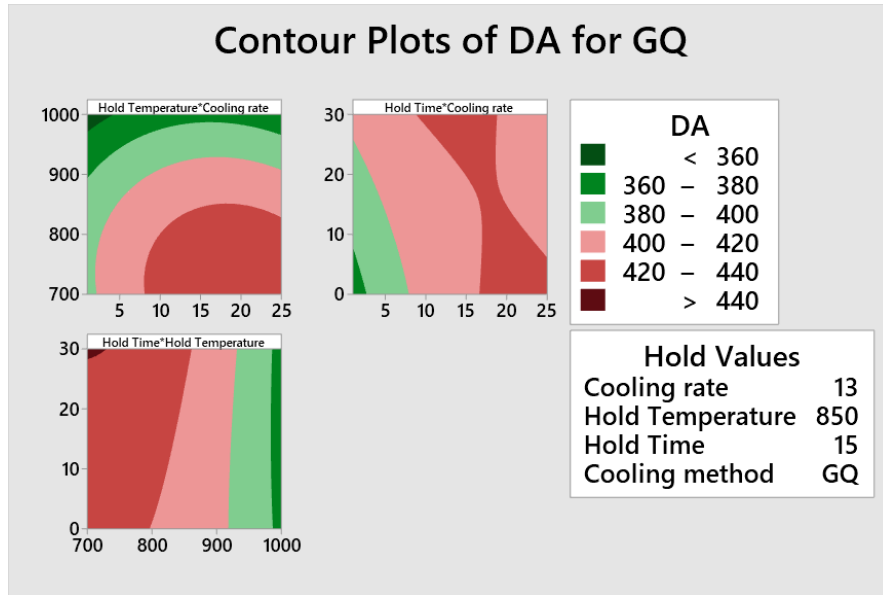


**Figure 7-9:** Contour plots for deformed and annealed samples (DA) that were gas quenched to room temperature. Legends on top of plots are in the form Y axis \*X axis i.e. Hold Temperature (Y axis) \* Cooling rate (X axis). Hardness units in HV, cooling rate in °C /min, hold temperature in °C, hold time in min and GQ indicates gas quench.

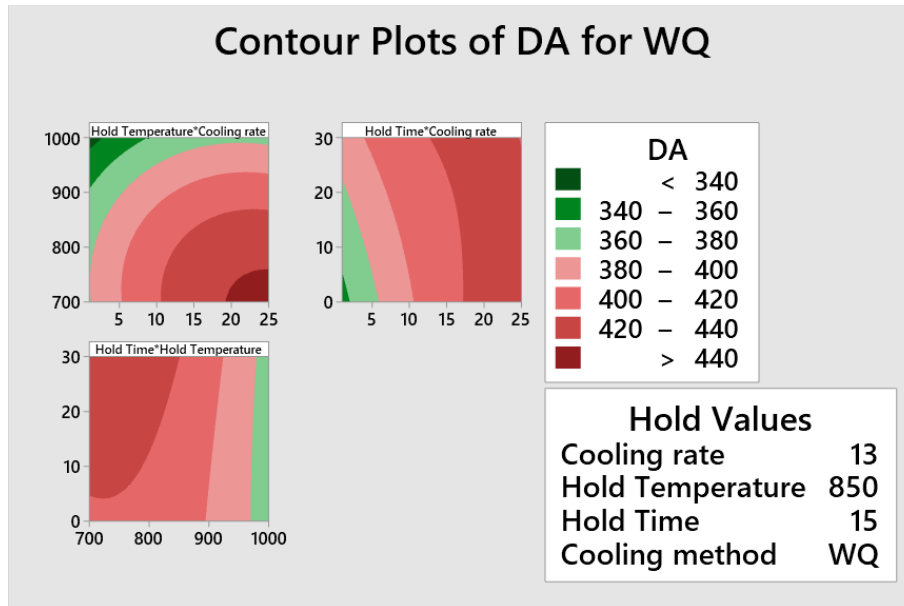


**Figure 7-10:** Contour plots for deformed and annealed samples (DA) that were water quenched to room temperature. Legends on top of plots are in the form Y axis \*X axis i.e. Hold Temperature (Y axis) \* Cooling rate (X axis). Hardness units in HV, cooling rate in °C /min, hold temperature in °C, hold time in min and WQ indicates water quench.

## Microstructural analysis

### *Deformed sample (D)*

The as-received deformed sample revealed a bimodal distribution of precipitates. Primary  $\gamma'$  was found on the grain boundaries with sizes ranging from 2-9  $\mu\text{m}$ . Secondary  $\gamma'$  was observed in two distinct morphologies, which also varied in size. The cuboidal morphology had an average size of  $439\pm 49\text{ nm} \times 396\pm 39\text{ nm}$  whereas the spheroidal was relatively smaller with an average size of  $225\pm 51\text{ nm} \times 199\pm 41\text{ nm}$ . Tertiary  $\gamma'$  was not observed in the as-received condition. The hardness of the deformed sample was  $490\pm 17\text{ HV}$ .

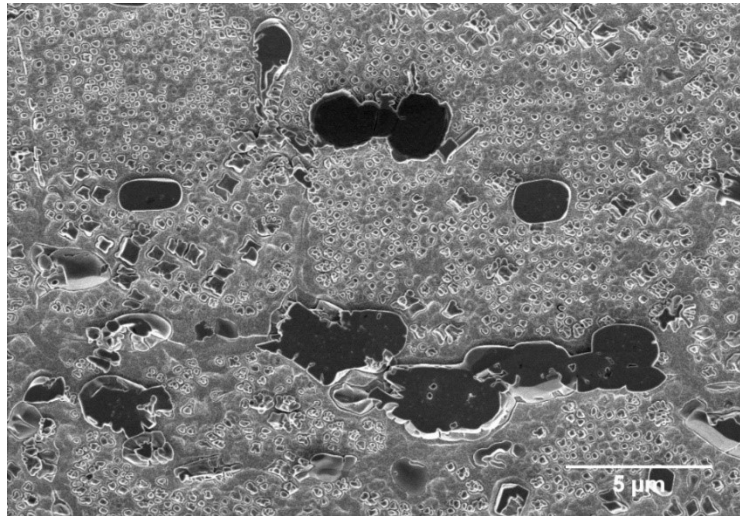


**Figure 7-11:** As received condition of the deformed sample. Primary  $\gamma'$  is present on the grain boundaries and secondary  $\gamma'$  is observed in cuboidal and spheroidal morphologies.

The factor levels that resulted in the lowest hardness ( $349\pm 23\text{ HV}$ ) were  $13^\circ\text{C}/\text{min}$  cooling rate from  $1095^\circ\text{C}$  annealing temperature to  $1000^\circ\text{C}$  hold temperature, 15 minutes hold time and water quench to room temperature. After heat treatment secondary  $\gamma'$  could be observed at  $258\pm 6 \times 267\pm 5$  average size in a uniform spheroidal morphology.

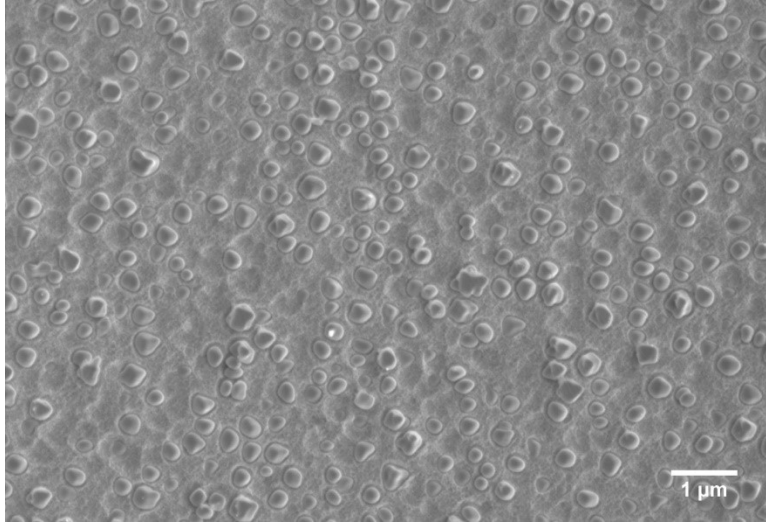


**Figure 7-12:** Softest sample after heat treatment. Secondary  $\gamma'$  could be observed at a uniform spheroidal morphology.

*Deformed and annealed sample (DA)*

The hardness of the as received deformed and annealed sample was  $413 \pm 21$  HV. Its microstructure was similar to the deformed sample, with a bimodal distribution of primary and secondary  $\gamma'$ . In this case, the primary  $\gamma'$  size range was from 2.5-5.9  $\mu\text{m}$  and the secondary  $\gamma'$   $234 \pm 57\text{nm} \times 216 \pm 48\text{nm}$  on the spheroidal morphology and  $544 \pm 122 \times 557 \pm 154\text{nm}$  on the cuboidal.

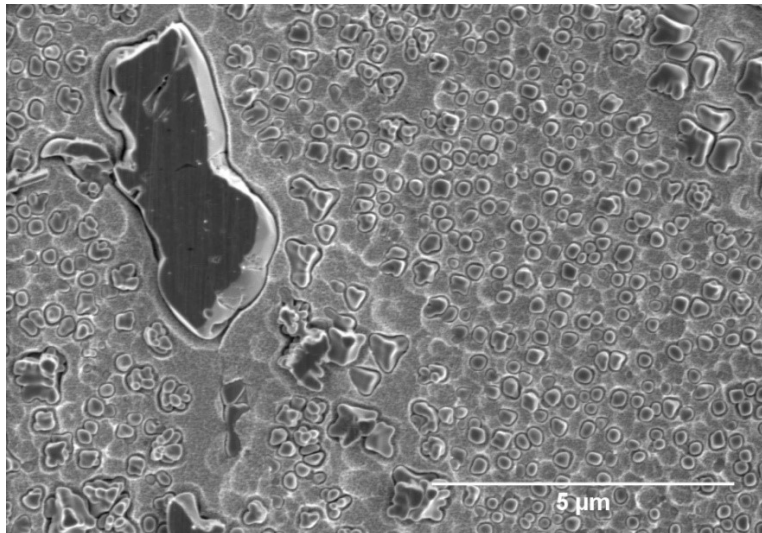


**Figure 7-13:** As received condition of the deformed and annealed sample. Primary  $\gamma'$  is present on the grain boundaries and secondary  $\gamma'$  is observed in cuboidal and spheroidal morphologies.

In higher magnifications, secondary  $\gamma'$  was observed to be splitting (Fig.14) in the first stages of the mechanism. A different mechanism of decomposition was observed on primary  $\gamma'$  particles in “medusa” (Fig.7-15) and “coral” (Fig. 7-16 and Fig.7-17) morphologies. Similar microstructural features to the coral morphology have been observed in other superalloys and are called “fan”  $\gamma'$  [16, 17] or “cellular” [18, 19]. Since those morphologies were observed rarely in the sample, representative microstructures are presented in Figs. 7-15 – 7-17 but no further analysis of the mechanism was conducted at this time. Tertiary  $\gamma'$  was not observed in the as-received condition of the deformed an annealed sample.

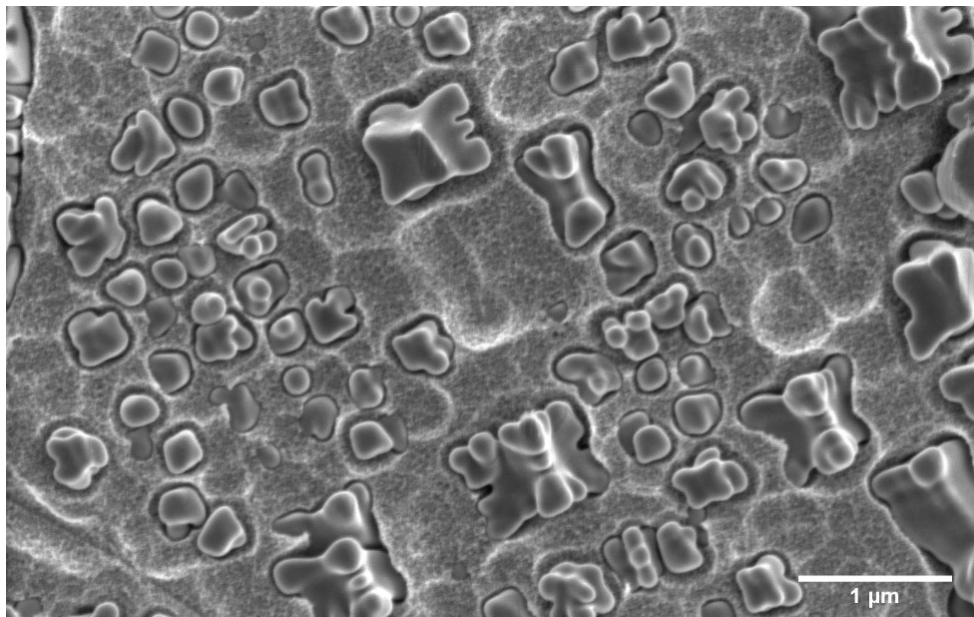


**Figure 7-14:**Secondary  $\gamma'$  splitting.

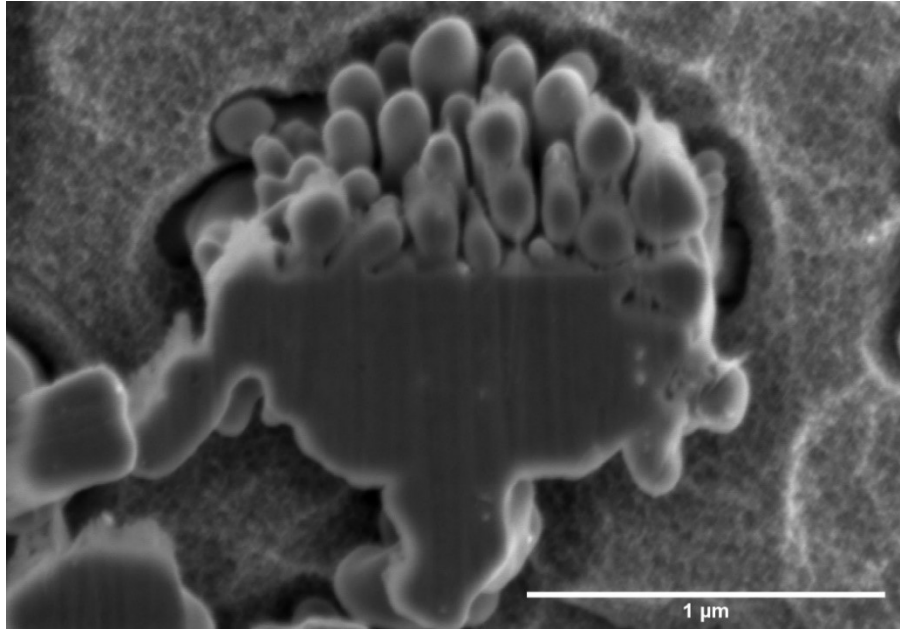


**Figure 7-15:** Primary  $\gamma'$  decomposing called “medusa” morphology.

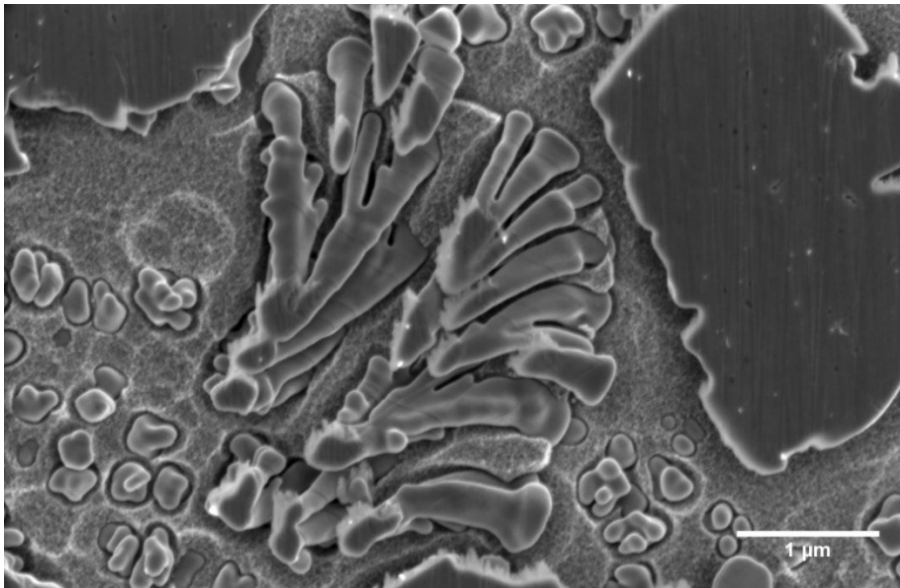


**Figure 7-16:** Primary  $\gamma'$  “coral” morphology.

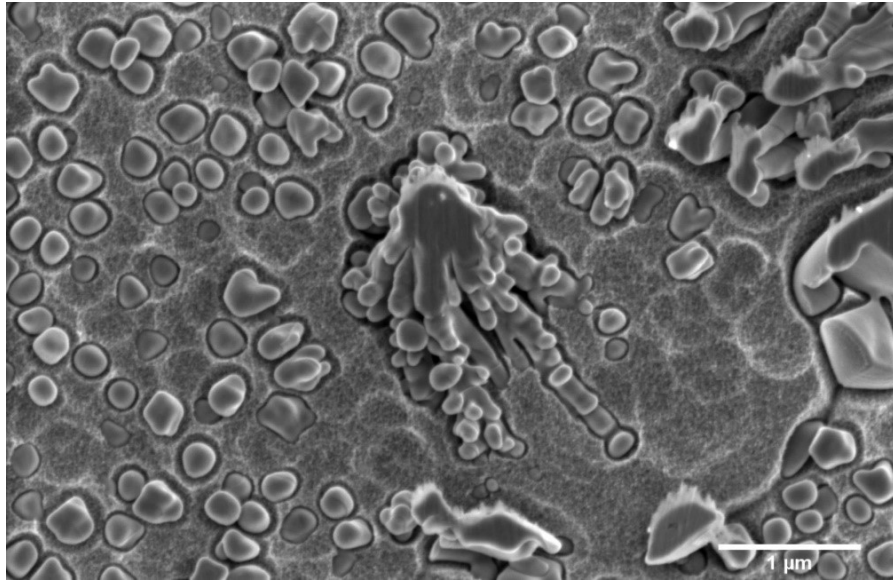


**Figure 7-17:** Primary  $\gamma'$  “coral” morphology.

The lowest hardness ( $347 \pm 15$  HV) was achieved by a different heat treatment factor combination than the one of the deformed samples. In this case, were  $1^\circ\text{C}/\text{min}$  cooling rate from  $1095^\circ\text{C}$  annealing temperature to  $850^\circ\text{C}$  hold temperature, 15 minutes hold time and water quench to room temperature. In Fig. 7-18 secondary  $\gamma'$  precipitates are observed in various stages of splitting, initialization of the cuboidal particles to final octacets as has been observed in the literature in other alloys <sup>[20]</sup>.

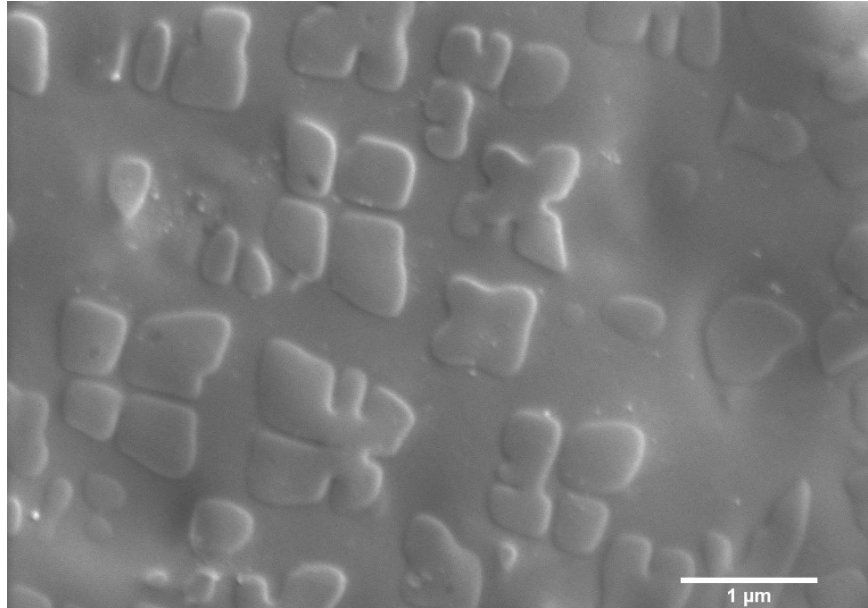


**Figure 7-18:** Secondary  $\gamma'$  precipitates after heat treatment are observed in various stages of splitting.

#### 7.4 Discussion

Rene 65 samples of two different initial microstructures, produced by different thermomechanical processing paths, were subjected to the same heat treatments and their hardnesses were measured. Theoretically, the factors that affect the hardness (i.e. cooling rate) should not change based on the initial microstructure although the hardness should be at different levels. In other words, the variance of the factors would alter the final microstructure, but it might be expected that, for the same material, the same factors would be statistically significant to affect the measured outcome (i.e. hardness). From the analysis of the experimental designs it seems that initial microstructure plays a role in determining which factors are statistically significant. More specifically, when the sample is deformed, the hold temperature has a stronger effect since both B and  $B^2$  terms were significant, compared to the deformed and annealed sample where only B was significant. Cooling rate (A) was found to be significant in both cases, which aligns with literature

[2], confirming that it is an important factor that could not be predicted from the Taguchi design in [6].

From a microstructural perspective, the two initial microstructures were quite similar, with a bimodal precipitate distribution in similar size ranges in both cases. Primary  $\gamma'$  was observed at the grain boundaries in both conditions with an interesting decomposition to secondary  $\gamma'$  phenomenon occurring in the deformed and annealed samples. The statistical equations that predict the final hardness from experimental design take into consideration only the factors that were varied and the two different initial microstructural conditions are treated as different experiments. Since the visible microstructural characteristics are similar, the respective equations for the deformed sample and for the deformed and annealed sample may be interchangeable. However, in both cases, there is an overestimation of + 45 HV and + 20 HV respectively, which underlines the importance of the initial microstructure.

Several microstructural characteristics may be influencing the results. It is well established that the energy state of a coherent precipitate is controlled by elastic strain energy due to lattice misfit, the interfacial energy between the matrix and the precipitate and the elastic interaction energy, which is related to the interaction between each precipitate with its neighbours. Splitting during coarsening occurs in elastic and strongly constrained systems and it is mainly related to the elastic interaction energy. It is undeniable that, when splitting occurs, since more surfaces are created, the interfacial energy will increase. Therefore, it is not energetically reasonable for the system to prefer this coarsening mechanism during heat treatment. Nevertheless, this phenomenon has been observed in the literature after aging in various Ni-based superalloys [20-23]. The split morphology is considered the equilibrium shape after total minimization of the energy and it has been observed in alloys with large misfit between  $\gamma$  and  $\gamma'$  [24]. The “medusa” secondary  $\gamma'$

morphology could be related to flower morphologies observed in [24] with the difference that those samples were aged and then furnace cooled to produce these microstructures while in this study the samples were deformed and annealed.

After heat treatment in the deformed and annealed sample, the slow cooling rate of 1°C/min from the annealing temperature to the hold temperature is favoring splitting into an octacet as it has also been observed in [25] where a split into an *ogdoad* occurred during slow continuous cooling slow cooling, whereas isothermal aging favors a split into a doublet. This is verified in the deformed sample where higher cooling rate (13°C/min) did not lead to splitting.

In general, reverse coarsening or splitting is a mechanism where the total number of individual particles increases and therefore the precipitation mechanism is more effective. It could be suggested from the observations of this work that the deformation part of the thermomechanical processing is favoring elastic constraining of the system. Therefore, secondary  $\gamma'$  tend to split into smaller particles to minimise the elastic interaction energy. After heat treatment the splitting is complete in most precipitates that were observed in the deformed and annealed sample and the hardness is decreasing since the split particles are still considered large secondary  $\gamma'$  and therefore their size is large enough to inhibit dislocation motion but not as effectively as tertiary  $\gamma'$  as pointed out by the work of Galindo-Nava [26].

The deformed sample had a smaller secondary  $\gamma'$  precipitate size in the as received microstructure compared to the deformed and annealed in both morphologies (spheroidal and cuboidal particles). A different heat treatment combination was necessary for the reduction of hardness of those smaller precipitates, since the lowest hardness was achieved without splitting of the precipitates. Therefore, it could be suggested that, depending on the residual stress and the original precipitate size, there should be a different mechanism activated in order to achieve

hardness reduction. In the case of large strain (deformed sample) and small precipitate size, a high cooling rate (13°C/min) from annealing temperature and a high hold temperature (1000°C) are resulting in a uniform secondary  $\gamma'$  without the necessity of precipitate splitting mechanism activation. For lower strain (deformed and annealed sample) and larger precipitates, splitting is necessary for hardness reduction and it is achieved by slow cooling rate (1°C/min) to a lower hold temperature (850°C).

## 7.5 Conclusions

Two initial microstructural conditions were examined with the same experimental design. The design based on Response Surface Methodology and more specifically Central Composite Design varied four parameters: cooling rate from annealing temperature, hold temperature, time at hold temperature and cooling method to room temperature. The conclusions of this work can be summarised as follows:

- There is an effect of the initial microstructure on the heat treatment combination that is most effective to reduce hardness, since the lowest hardness was achieved by a different set of conditions (different levels of each parameter) for both samples.
- The parameters themselves that affect more the response (hardness) are also varying based on the initial microstructure, with some similarities. On the deformed sample the most significant factors were, in descending order hold temperature, cooling rate and hold temperature squared. On the contrary on the deformed and annealed sample only the hold temperature and cooling rate.
- The heat treatment parameter combinations that achieved the lowest hardness were 13°C/min cooling rate from 1095°C annealing temperature to 1000°C hold temperature, 15 minutes hold time and water quench to room temperature for the deformed sample

(349±23HV) and 1°C/min cooling rate from 1095°C annealing temperature to 850°C hold temperature, 15 minutes hold time and water quench to room temperature for the deformed and annealed sample (347±15 HV).

- There were two mechanisms proposed for hardness reduction depending on the initial microstructure. For the deformed samples where there is a large strain induced and the precipitates are relatively smaller, a high cooling rate is proposed from annealing temperature to a high hold temperature since it is resulting in a uniform secondary  $\gamma'$  without the necessity to activate the precipitate splitting mechanism. On the contrary, for the deformed and annealed samples where there is less strain induced (after the annealing step) but larger precipitates are present, splitting is necessary for hardness reduction and it can be achieved by slow cooling rate to a lower hold temperature.

Interesting microstructural observations of primary  $\gamma'$  decomposing into smaller particles will be further investigated in the future for possible variation in composition, lattice mismatch or grain boundary mobility. A possible approach to study these features could be based on <sup>[27]</sup> where focused ion beam sectioning can reveal the 3D structure.

## 7.6 Acknowledgements

Financial support from the Natural Science and Engineering Council of Canada, GE Aviation, Bromont, Quebec Canada, the Consortium de Recherche et D'innovation en Transformation Métallique and the McGill Engineering Doctoral Award (to C.M. Katsari) is gratefully acknowledged. Dr. Ozan Kokkilic from McGill University and Dr. Oluwole A. Olufayo from Ecole Technologie Superieure are acknowledged for the useful discussions regarding Response Surface Methods. The authors would also like to thank Mr. Martin Therer from GE Aviation, Bromont for his valuable inputs on this work from the industrial point of view.

## 7.7 References

- 1 M.-A. Charpagne, T. Billot, J.-M. Franchet, and N. Bozzolo: in *13th International Symposium on Superalloys, SUPERALLOYS 2016, September 11, 2016 - September 15, 2016*, vol. 2016-Janua, Minerals, Metals and Materials Society, MINES ParisTech, PSL - Research University, CEMEF - Centre de Mise en Forme des Materiaux, CNRS UMR 7635, CS 10207 rue Claude Daunesse, Sophia Antipolis Cedex; 06904, France Snecma-Safran Group, Technical Department, 171 boulevard de Valmy, Colombes Cedex;, 2016, pp. 417–26.
- 2 A. Laurence, J. Cormier, P. Villechaise, T. Billot, J.-M. Franchet, F. Pettinari-Sturmel, M. Hantcherli, F. Mompiau, and A. Wessman: in *8th International Symposium on Superalloy 718 and Derivatives 2014, September 28, 2014 - October 1, 2014*, John Wiley and Sons Inc., Institut Pprime, Physics and Mechanics of Materials Department, ISAE-ENSMA, 1 avenue Clement Ader, Futuroscope - Chasseneuil; 86961, France Snecma-Safran Group, Technical Department, 171 boulevard de Valmy - BP 31, Colombes Cedex; 92702, France Safran SA, M, 2014, pp. 333–48.
- 3 A. Wessman, A. Laurence, J. Cormier, P. Villechaise, T. Billot, J.-M. Franchet, W. Andrew, L. Aude, C. Jonathan, V. Patrick, B. Thomas, and F. Jean-Michel: in *Superalloys 2016: Proceedings of the 13th Intenational Symposium of Superalloys*, vol. 2016-Janua, Minerals, Metals and Materials Society, GE Aviation, One Neumann Way, Cincinnati; OH; 45215, United States Institut Pprime, UPR CNRS 3346, CNRS, Universite de Poitiers - ENSMA, Physics and Mechanics of Materials Department, ISAE-ENSMA, 1 avenue Clement Ader, Futuroscope - Chasseneuil; 86961, Fra, 2016, pp. 793–800.
- 4 T. Wojcik, M. Rath, and E. Kozeschnik: *Mater. Sci. Technol.*, 2018, vol. 34, pp. 1558–64.
- 5 C.M. Katsari, H. Che, D. Guye, A. Wessman, and S. Yue: in *Proceedings of the 9th International Symposium on Superalloy 718 & Derivatives: Energy, Aerospace, and Industrial*

*Applications*, E. Ott, X. Liu, J. Andersson, Z. Bi, K. Bockenstedt, I. Dempster, J. Groh, K. Heck, P. Jablonski, M. Kaplan, D. Nagahama, and C. Sudbrack, eds., Springer International Publishing Ag, [Katsari, C. M.; Che, H.; Guye, D.; Yue, S.] McGill Univ, Dept Mat Engn, Wong Bldg, 3610 Univ, Montreal, PQ H3A 0C5, Canada. [Wessman, A.] GE Aviat, Struct Mat Dev, One Neumann Way, Cincinnati, OH 45215 USA. Katsari, CM (reprint author), McGill Univ, Dept , 2018, pp. 629–41.

6 C.M. Katsari, A. Wessman, and S. Yue: *J. Mater. Eng. Perform.*, 2020, pp. 1–9.

7 T.M. Pollock and S. Tin: *J. Propuls. Power*, 2006, vol. 22, pp. 361–74.

8 O.R. Terrazas, M.E. Zaun, R.S. Minisandram, and M.L. Lasonde: in *9th International Symposium on Superalloy 718 and Derivatives: Energy, Aerospace, and Industrial Applications, June 3, 2018 - June 6, 2018*, vol. 2018-June, Springer International Publishing, ATI Specialty Materials, 4374 Lancaster Highway, Richburg; SC; 29729, United States ATI Specialty Materials, 2020 Ashcraft Avenue, Monroe; NC; 28110, United States Wilmot; NH; 28110, United States, 2018, pp. 977–86.

9 C.M. Katsari, H. Che, B. Turner, A. Wessman, and S. Yue: in *Materials Science and Technology Conference and Exhibition 2017, MS and T 2017, October 8, 2017 - October 12, 2017*, vol. 2, Association for Iron and Steel Technology, AISTECH, Materials Engineering Dept., McGill University, Wong Building, 3610 University, Montreal; QC; H3A 0C5, Canada GE Aviation, Structural Materials Development, One Neumann Way, Cincinnati; OH; 45215-1988, United States, 2017, pp. 1375–81.

10 B.J. Bond, C.M. O'Brien, J.L. Russell, J.A. Heaney, and M.L. Lasonde: in *8th International Symposium on Superalloy 718 and Derivatives 2014, September 28, 2014 - October 1, 2014*, John Wiley and Sons Inc., ATI Specialty Materials, 2020 Ashcraft Ave., Monroe; NC;

28110, United States General Electric Aviation, One Neumann Way, Cincinnati; OH; 45215, United States, 2014, pp. 107–18.

11 P.D. Berger, R.E. Maurer, and G.B. Celli: in *Experimental Design*, Springer, 2018, pp. 533–84.

12 D.C.L.B.-D.O.E. Montgomery: *Design and Analysis of Experiments*, John Wiley & Sons, 2017.

13 Minitab 18 Support: Overview for Create Response Surface Design (Central Composite).

14 A.E. Wessman: University of Cincinnati, 2016.  
[http://rave.ohiolink.edu/etdc/view?acc\\_num=ucin1467126769](http://rave.ohiolink.edu/etdc/view?acc_num=ucin1467126769)

15 C.M. Katsari, A. Wessman, and S. Yue: *Heat Treat 1930th Heat Treat. Soc. Conf. Expo.*, 2019.

16 D.U. Furrer and H.-J. Fecht: *Scr. Mater.*, 1999, vol. 40, pp. 1215–20.

17 A. Powell, K. Bain, A. Wessman, D. Wei, T. Hanlon, and D. Mourer: in *Superalloys 2016: Proceedings of the 13th International Symposium of Superalloys*, Wiley Online Library, 2016, pp. 187–97.

18 L. Zhuo, M. Huang, F. Wang, J. Xiong, J. Li, and J. Zhu: *Mater. Lett.*, 2015, vol. 139, pp. 232–6.

19 J.D. Nystrom, T.M. Pollock, W.H. Murphy, and A. Garg: *Metall. Mater. Trans. A*, 1997, vol. 28, pp. 2443–52.

20 M. Doi: *Mater. Trans. JIM*, 1992, vol. 33, pp. 637–49.

21 Y.S. Yoo, D.Y. Yoon, Henry, and MF: *Met. Mater.*, 1995, vol. 1, pp. 47–61.

22 M. Doi, D. Miki, T. Moritani, and T. Kozakai: *Superalloys 2004*, 2004, pp. 109–14.

23 M. Doi and T. Miyazaki: *Superalloys 1984*, 1984, pp. 543–52.

- 24 Y.S. Yoo: *Scr. Mater.*, 2005, vol. 53, pp. 81–5.
- 25 M. Doi, T. Miyazaki, and T. Wakatsuki: *Mater. Sci. Eng.*, 1985, vol. 74, pp. 139–45.
- 26 E.I. Galindo-Nava, L.D. Connor, and C.M.F. Rae: *Acta Mater.*, 2015, vol. 98, pp. 377–90.
- 27 J. MacSleyne, M.D. Uchic, J.P. Simmons, and M. De Graef: *Acta Mater.*, 2009, vol. 57, pp. 6251–67.

## Chapter 8 : General Discussion

This thesis focused on the determination of a softening heat treatment for manufacturing purposes by characterizing the strengthening precipitates and, with this knowledge, designing heat treatments to control them.

Previous studies at McGill (unpublished work) showed that secondary and tertiary  $\gamma'$  were dissolved at 1095°C and only primary  $\gamma'$  was present at room temperature after water quenching. Nevertheless, water quenching from such high temperatures is not always an option for industrial applications, as it is a very severe cooling method for the parts. This set the 1095°C as the annealing temperature, since primary  $\gamma'$  need always to be present to stop grain growth.

Another heat treatment was then explored, which was furnace cooling from the annealing temperature (1095°C) to a lower (but still high) temperature. The idea behind the intermediate temperature heat treatment was to coarsen the re-precipitated  $\gamma'$  particles. Indeed, in all four proposed heat treatments, the microstructural characteristics of the strengthening precipitates were a monomodal secondary  $\gamma'$  size of more than 200 nm and, interestingly, the morphologies differed in all cases, as they were cuboidal (as-extruded OFAT), agglomerates (deformed-Taguchi), spheroidal (deformed-CCD), split/cuboidal (deformed an annealed-CCD). None of the “soft” microstructures contained tertiary  $\gamma'$  precipitates, but primary  $\gamma'$  was always present for the pinning effect.

From all three approaches in optimizing the intermediate temperature heat treatment, OFAT, Taguchi and CCD, the average hardness values that could be achieved were very similar for each thermomechanical processed condition; as-extruded (OFAT) 354 HV, deformed (Taguchi) 371 HV, deformed (CCD) 349 HV, deformed and annealed (CCD) 347 HV. However, the heat treatments that achieved those similar hardness values were largely different, the only

commonality being the 1095 °C annealing temperature. For the as-extruded condition, 15 °C/min to 954 °C no hold and water quenching gave the softest sample. In the Taguchi design for the deformed sample condition, a slower cooling rate (5 °C/min) to a lower temperature (900 °C), but again no hold and gas quench (which was the fastest cooling method in this design) achieved the lowest hardness. The same sample condition in CCD needed a cooling rate similar to that for the as - extruded (13 °C/min) but to a higher temperature (1000 °C) and a hold of 15 minutes finishing with a water quench, like the extruded sample, to yield the lowest hardness. For another type of deformation and annealing, the slowest cooling rate used in all approaches (1°C/min), to the lowest temperature (850 °C), but, again, a hold of 15 minutes finishing with a water quench leads to the lower hardness.

The general trend for cooling to room temperature seems to be the fastest the better, since precipitation of the smallest precipitate populations is suppressed and, as this is the most effective strengthening mechanism, its suppression is beneficial for the softening. The hold time does not seem to have an effect, as in most cases there was no or minimal time (i.e., 15 minutes) that resulted in the lowest hardness values. It seems that the main effect is with the other two factors, as was evident from the CCD statistical analysis. What is interesting is that hold temperature has a strong effect by itself (from both Taguchi and CCD designs in both conditions) but the interaction with cooling rate was not deemed significant; rather, cooling rate and hold temperature were significant as separate (main) factors. From a microstructural point of view though, there is an interplay of the hold temperature to be reached by a specific rate, i.e., higher cooling rates reached higher hold temperatures, and lower cooling rates reached lower temperatures. As mentioned in Chapter 7, it could be suggested that, depending on the residual stress and the precipitate size in the as received microstructure, there should be a different mechanism activated to achieve hardness reduction. For

strain-induced samples (deformed) and small precipitate sizes, a high cooling rate from annealing temperature and a high hold temperature are resulting in a uniform secondary  $\gamma'$  without the necessity of precipitate splitting mechanism activation. For lower strain (deformed and annealed samples) and larger precipitates, the splitting mechanism is necessary for hardness reduction.

As mentioned in Chapters 6 and 7, the 3 factor levels were based on lab equipment capabilities (i.e., furnace cooling rate) and industrial applicability (i.e., short hold times, air and gas quench), while temperatures were based on metallurgical principles. Water quenching was examined to preserve the high temperature microstructure at room temperature, although as mentioned above this can be limited in industrial applications in some cases. As stated before, the annealing temperature was chosen at 1095°C and was fixed to retain primary  $\gamma'$  in the microstructure to limit grain growth. In Chapters 5, 6 and 7 the reasoning behind the level range is addressed, i.e., hold temperature levels were chosen based on thermodynamic calculations and the TTT diagram. It would be interesting to evaluate the interplay of cooling rate with these hold temperatures with a lab or industrial furnace that can achieve higher difference among levels, since the maximum difference between high and low levels that was achieved in this thesis was 24°C, due to lab furnace limitations.

In Chapter 4, the chemical compositions of each precipitate size were found to differ within the same processing condition, which then affected their lattice mismatch with the matrix. Since secondary and tertiary  $\gamma'$  affect the hardness, it is an important metallurgical factor that could be included in the empirical equations that were created for hardness predictions. As APT is a high-resolution technique and the sample preparation as well as the equipment are highly specialised, expensive, or difficult to use, it is currently difficult to get enough data points to include in such equations. Literature values or theoretical calculations can be used as a numerical indicator that is

affecting the precipitate morphology. Average aspect ratio is another numerical factor that could be included in the equations, which describes the variability of  $\gamma'$  morphologies in the structure. This, along with precipitate volume fraction, can be collected from the analysis of SEM images, which are easier to acquire than APT data.

In summary, Ni-based superalloys are sensitive to their thermomechanical processing history. It was proven that precipitates can split in Rene 65 to reduce the overall hardness, but this depends on the initial condition of the sample. The different regression equations and contour plots provided can be used for predictions within the ranges tested in each Chapter, but, due to the sensitivity of the microstructures, caution must be taken before applying a heat treatment to different processing steps. In the future, these equations can be further enriched by including microstructural factors (i.e., phase volume fractions, chemical compositions, aspect ratio etc).

## Chapter 9 : Summary and Conclusions

In this thesis, Rene 65 samples from various thermomechanical processing histories were examined. An approach to thermomechanical processing optimization was achieved via heat treatment experimental design as well as microstructural and statistical analysis. More specifically, in Chapter 4 a thorough microstructural characterisation of the three different sizes of  $\gamma'$  before and after a softening heat treatment was conducted to identify compositional and microstructural differences between the precipitates. Then, in Chapter 5, to soften the material for manufacturing purposes, the traditional experimental approach of changing one factor at a time was applied. A non-traditional heat treatment sequence based on holding at an intermediate temperature was suggested. In Chapters 6 and 7, Taguchi design and Central Composite Design respectively were applied to optimize this heat treatment sequence.

The main conclusions can be summarised as follows:

1. In the as-extruded condition, primary and secondary  $\gamma'$  had higher Ti than Al percentage [ $\text{Ni}_3(\text{Ti},\text{Al})$ ], whereas tertiary  $\gamma'$  had higher Al [ $\text{Ni}_3(\text{Al},\text{Ti})$ ]. The secondary  $\gamma'$  morphology was irregular with an average size of  $210.24 \pm 48 \text{ nm} \times 189.55 \pm 38 \text{ nm}$  and average aspect ratio of  $0.9 \pm 0.19$ . Tertiary  $\gamma'$  average size was found to be  $10.91 \pm 5 \text{ nm}$  by  $10.62 \pm 4.1 \text{ nm}$  with aspect ratio of 0.97, which indicates an almost spherical morphology. A further smaller size distribution of  $\gamma'$  precipitates, (quaternary  $\gamma'$ ) were richer in  $\gamma$  forming elements Cr, Mo and Co, indicating a lower formation temperature. In secondary  $\gamma'$ , the higher % Ti increases the lattice parameter and therefore there is a higher mismatch (0.89%) with the matrix compared to the mismatch of tertiary  $\gamma'$  with the matrix. The composition of secondary  $\gamma'$  had not changed significantly after the

- heat treatment. However, the Ti content increased and the interface between the matrix and the precipitate became chemically homogenous.
2. It was observed that the strength of Rene 65 depends on secondary  $\gamma'$  precipitates' size and volume fraction. Holding at 954°C, a temperature below the annealing temperature influenced precipitation kinetics. The average size of secondary  $\gamma'$  decreased for short hold times because of nucleation of new secondary precipitates. For longer hold times, growth kinetics were faster than nucleation kinetics.
  3. A softening heat treatment was designed based on Taguchi's L8 matrix. The most significant factor affecting hardness was hold temperature based on the regression analysis. The softest sample and the hardest sample were microstructurally different. The increase in strength is attributed to the presence of three distinct sizes of  $\gamma'$ .
  4. The initial microstructure (thermomechanical history) has an effect on the heat treatment combination that is most effective to reduce hardness. The heat treatment parameter combinations that achieved the lowest hardness were 13°C/min cooling rate from 1095°C annealing temperature to 1000°C hold temperature, 15 minutes hold time and water quench to room temperature for the deformed (D) sample. For the deformed and annealed sample (DA) it was 1°C/min cooling rate from 1095°C annealing temperature to 850°C hold temperature, 15 minutes hold time and water quench to room temperature. On the "D" condition the most significant factors were: hold temperature, cooling rate and hold temperature squared. On the contrary, on the "DA" condition only the hold temperature and cooling rate were found significant. Splitting was observed in the "DA" condition, where samples had larger precipitates and less strain induced, as a hardness reduction mechanism. Split morphologies were not observed in

the “D” condition, where precipitates were smaller in size and there was more strain induced.

## Chapter 10 : Future work

Rene 65 is an extraordinary alloy that has potential for many applications. As future steps after this thesis, the researcher can delve into the following topics, which are scientific and engineering oriented:

- Extensive TEM analysis for precipitate coherency determination
- Atom probe tomography on split morphologies and further understanding of the mechanism behind them.
- Mechanical properties testing such as torsion/compression/tensile/shear punch to support the hardness results.
- Experimental design including heating rate and solution temperature as parameters.
- Multiple deformation steps while applying the softening heat treatment between them.
- Machine learning correlation with statistical analysis results of this work.

The TEM and APT analysis will help further understand fundamentally those unusual  $\gamma'$  morphologies as they do not appear frequently in the microstructure and if their effect proves to be beneficial, it might be another microstructural design characteristic to consider while designing a heat treatment.

The effect of each heat treatment was assessed after deformation, so the next step would be to apply these heat treatments at consecutive deformation steps, i.e., torsion testing, to evaluate their effect at multiple passes (tensile and compression testing have similar limitations for multiple passes due to shape changes, torsion specimens do not undergo shape changes and can therefore be subjected to high deformation strains). For a single pass though, mechanical properties after heat treatment could be easily assessed by compression tests for the as extruded samples. Indeed,

for the deformed and deformed and annealed industrial samples, the mechanical properties correlation could be more easily evaluated by shear punch tests correlation with tensile curves.

An interesting approach would be the use of supervised machine learning. With predictive models and a large dataset of all experimental results, of this thesis as well as past and future data points of this alloy, other heat treatments may be found that reduce the hardness to a larger extent. Design of Experiments tool can also be utilized including more variables, which would complicate the design as well as other factor levels that are not limited to i.e., furnace cooling maxima.

## Chapter 11 : Contribution to original knowledge

The intended contribution to original knowledge is summarized in the following points:

1. For the first time in the newly developed nickel-base superalloy Rene 65, the exact chemical composition of the three size fractions of gamma prime phase was accurately determined by high resolution characterisation techniques. The higher contribution of Ti in secondary  $\gamma'$  which increases the lattice parameter is an indicator of the difference in morphology and could be used as an alloy design factor for future alloys with trimodal distribution.
2. The findings of this thesis are adding important data points in the precipitation characteristics of trimodal precipitation cast and wrought superalloys and can be utilized to enhance thermodynamic/kinetic software databases (e.g., Thermocalc).
3. Introduction and optimization of interrupted temperature heat treatment step (hold temperature and time) by using “Experimental Design” tools. In contrast to traditional Ni-based superalloy heat treatments (i.e., annealing and aging), which are mainly focused on increasing the strength for the final application, the proposed heat treatments succeeded in softening the parts for manufacturing purposes.
4. Regression equations for hardness predictions were developed highlighting the importance of thermomechanical history of the alloy. Two mechanisms were proposed for softening the alloy, depending on the initial microstructure and strain applied in the as-received condition. This can be used as a guide to develop thermo-mechanical processing schedules.
5. For the first time, the splitting mechanism of secondary  $\gamma'$  was observed in this alloy. Also, decomposition phenomena were observed in primary  $\gamma'$ .

## Chapter 12 : Bibliography

- 1 C.-M. Katsari, S. Katnagallu, and S. Yue: *Mater. Charact.*,  
DOI:10.1016/j.matchar.2020.110542.
- 2 C.M. Katsari, H. Che, D. Guye, A. Wessman, and S. Yue: in *Proceedings of the 9th International Symposium on Superalloy 718 & Derivatives: Energy, Aerospace, and Industrial Applications*, E. Ott, X. Liu, J. Andersson, Z. Bi, K. Bockenstedt, I. Dempster, J. Groh, K. Heck, P. Jablonski, M. Kaplan, D. Nagahama, and C. Sudbrack, eds., vol. 2018-June, Springer International Publishing Ag, 2018, pp. 629–41.
- 3 C.M. Katsari, A. Wessman, and S. Yue: *J. Mater. Eng. Perform.*, DOI:10.1007/s11665-020-04783-0.
- 4 C.M. Katsari, A. Wessman, and S. Yue: *Metall. Mater. Trans. A Phys. Metall. Mater. Sci.*, DOI:10.1007/s11661-020-05948-1.
- 5 R.C. Reed: *The Superalloys: Fundamentals and Applications*, Cambridge university press, 2008.
- 6 Statista: *Market Share of the Leading Commercial Aircraft Engine Manufacturers Worldwide as of December 2019, 2020*.
- 7 R.E. Schafrik, D.D. Ward, and J.R. Groh: *Superalloys*, 2001, vol. 718, pp. 1–11.
- 8 R.E. Schafrik: *Metall. Mater. Trans. A*, 2016, vol. 47, pp. 2539–49.
- 9 A. Wessman, A. Laurence, J. Cormier, P. Villechaise, T. Billot, J.-M. Franchet, W. Andrew, L. Aude, C. Jonathan, V. Patrick, B. Thomas, F. Jean-Michel, A. Wessman, A. Laurence, J. Cormier, P. Villechaise, T. Billot, and J.-M. Franchet: in *Superalloys 2016: Proceedings of the 13th International Symposium of Superalloys*, vol. 2016-Janua, Minerals, Metals and Materials Society, 2016, pp. 793–800.

- 10 B.J. Bond, C.M. O'Brien, J.L. Russell, J.A. Heaney, and M.L. Lasonde: in *8th International Symposium on Superalloy 718 and Derivatives 2014, September 28, 2014 - October 1, 2014*, John Wiley and Sons Inc., 2014, pp. 107–18.
- 11 M.J. Donachie and S.J. Donachie: DOI:10.1361/stgs2002p011.
- 12 M. Durand-Charre: *The Microstructure of Superalloys*, CRC press, 1998.
- 13 J. Sato, T. Omori, K. Oikawa, I. Ohnuma, R. Kainuma, and K. Ishida: *Science (80-. )*, 2006, vol. 312, pp. 90–1.
- 14 John Marcin and Matthew Donachie: in *Heat Treating of Nonferrous Alloys*, G.E. Totten and D.S. MacKenzie, eds., vol. 4E, 2016, pp. 459–78.
- 15 J. Liu, J.J. Yu, Y.H. Yang, Y.Z. Zhou, and X.F. Sun: *Mater. Sci. Eng. A*, 2019, vol. 745, pp. 404–10.
- 16 F. Zhong, S. Li, and J. Sha: *Mater. Sci. Eng. A*, 2015, vol. 637, pp. 175–82.
- 17 G.H. Gessinger: in *Powder Metallurgy of Superalloys*, G.H. Gessinger, ed., Butterworth-Heinemann, 1984, pp. 112–31.
- 18 A. Banik, K.A. Green, M.C. Hardy, D.P. Mourer, and T. Reay: in *10th International Symposium on Superalloys, Seven Springs Mountain Resort, Champion, PA*, 2004, pp. 19–23.
- 19 G.H. Gessinger: in *Powder Metallurgy of Superalloys*, G.H. Gessinger, ed., Butterworth-Heinemann, 1984, pp. 328–37.
- 20 K. Minet, A. Saharan, A. Loesser, and N. Raitanen: in *Additive Manufacturing for the Aerospace Industry*, F. Froes and R. Boyer, eds., Elsevier, 2019, pp. 163–85.
- 21 S.E. Atabay, O. Sanchez-Mata, J.A. Muñoz-Lerma, R. Gauvin, and M. Brochu: *Mater. Sci. Eng. A*, 2020, vol. 773, p. 138849.

- 22 O. Sanchez-Mata, X. Wang, J. Muñiz-Lerma, M. Attarian Shandiz, R. Gauvin, and M. Brochu: *Materials (Basel)*, 2018, vol. 11, p. 1288.
- 23 CMF International : The power of Flight.
- 24 J. Jewell, C. Soret, P. Bradley, and T.A. Almahmood: CFM LAUNCHES A NEW ERA AS FIRST LEAP ENGINE BEGINS GROUND TESTING,  
<https://www.cfmaeroengines.com/press-articles/cfm-launches-a-new-era-as-first-leap-engine-begins-ground-testing/713/>.
- 25 CFM International: ‘How do jet engines work ?’, <https://www.safran-aircraft-engines.com/media/how-do-jet-engines-work-20140121>.
- 26 A. Laurence, J. Cormier, P. Villechaise, T. Billot, J.-M. Franchet, F. Pettinari-Sturmel, M. Hantcherli, F. Momprou, and A. Wessman: in *8th International Symposium on Superalloy 718 and Derivatives 2014, September 28, 2014 - October 1, 2014*, John Wiley and Sons Inc., 2014, pp. 333–48.
- 27 D. Greenfield: *ATI Pre-Airshow Event Bakers, NC*, 2017.
- 28 J. A. Heaney, M. L. Lasonde, A. M. Powell, B. J. Bond, and C. M. O’Brien: 2014, pp. 67–77.
- 29 P. Samal and J. Newkirk: .
- 30 S.T. Wlodek, M. Kelly, and D.A. Alden: *Superalloys*, 1996, vol. 1996, pp. 129–36.
- 31 A.E. Wessman: University of Cincinnati, 2016.
- 32 J.H. Weber, Y.E. Khalfalla, and K.Y. Benyounis: .
- 33 A. Kracke and A. Allvac: in *7th international symposium on Superalloy*, vol. 718, 2010, pp. 13–50.
- 34 *ASM Handbook Volume 15: Casting*, ASM International, 2008.

- 35 A. Mitchell: *High Temp. Mater. Process.*, 2005, vol. 24, pp. 101–10.
- 36 T.M. Pollock and S. Tin: *J. Propuls. Power*, 2006, vol. 22, pp. 361–74.
- 37 A.P.B.T.-I. to A.M. Mouritz, ed.: Woodhead Publishing, 2012, pp. 128–53.
- 38 PCT/US2016/035659: 2016.
- 39 P.N. Quested and M. McLean: *Mater. Sci. Eng.*, 1984, vol. 65, pp. 171–80.
- 40 S. Duval, S. Chambrelan, P. Caron, and D. Blavette: *Acta Metall. Mater.*, 1994, vol. 42, pp. 185–94.
- 41 N.K. Arakere and G. Swanson: *J. Eng. Gas Turbines Power*, 2002, vol. 124, pp. 161–76.
- 42 J. William D. Callister: .
- 43 M.-A. Charpagne, T. Billot, J.-M. Franchet, and N. Bozzolo: *J. Alloys Compd.*, 2016, vol. 688, pp. 685–94.
- 44 M.-A. Charpagne, T. Billot, J.-M. Franchet, and N. Bozzolo: in *13th International Symposium on Superalloys, SUPERALLOYS 2016, September 11, 2016 - September 15, 2016*, vol. 2016-Janua, Minerals, Metals and Materials Society, 2016, pp. 417–26.
- 45 S.L. Semiatin and J.J. Jonas: *Am. Soc. Met. 1984*, 1984, p. 299.
- 46 G.E. Dieter and D. Bacon: *Mechanical Metallurgy*, vol. 3, McGraw-hill New York, 1986.
- 47 J. V Bee, A.R. Jones, and P.R. Howell: *J. Mater. Sci.*, 1981, vol. 16, pp. 1471–6.
- 48 R.S. Minisandram, L.A. Jackman, J.L. Russell, M.L. Lasonde, J.A. Heaney, and A.M. Powell: in *8th International Symposium on Superalloy 718 and Derivatives 2014, September 28, 2014 - October 1, 2014*, John Wiley and Sons Inc., 2014, pp. 95–105.
- 49 O.R. Terrazas, M.E. Zaun, R.S. Minisandram, and M.L. Lasonde: in *9th International Symposium on Superalloy 718 and Derivatives: Energy, Aerospace, and Industrial Applications, June 3, 2018 - June 6, 2018*, vol. 2018-June, Springer International

- Publishing, 2018, pp. 977–86.
- 50 M.C. Hardy, M. Detrois, E.T. McDevitt, C. Argyrakis, V. Saraf, P.D. Jablonski, J.A. Hawk, R.C. Buckingham, H.S. Kitaguchi, and S. Tin: *Metall. Mater. Trans. A*, 2020, vol. 51, pp. 2626–50.
- 51 M. Mirzaei and R. Karimi: in *ICF10, Honolulu (USA) 2001*, 2001.
- 52 C.T. Sims, N.S. Stoloff, and W.C. Hagel: *Superalloys II*, Wiley New York, 1987.
- 53 K. Brun and R. Kurz: *Introduction to Gas Turbine Theory*, 3rd Editio., 2019.
- 54 G. Welsch, R. Boyer, and E.W. Collings: *Materials Properties Handbook: Titanium Alloys*, ASM international, 1993.
- 55 H. Harada, M. Yamazaki, Y. Koizumi, N. Sakuma, N. Furuya, and H. Kamiya: D. Coutsouradis, T.B. Gibbons, Y. Lindblom, D.B. Meadowcroft, and R. Stickler, eds., Springer Netherlands, Dordrecht, 1982, pp. 721–35.
- 56 A.K. Jena and M.C. Chaturvedi: *J. Mater. Sci.*, 1984, vol. 19, pp. 3121–39.
- 57 T.B. Bhat and V.S. Arunachalam: *Proc. Indian Acad. Sci. Sect. C Eng. Sci.*, 1980, vol. 3, pp. 275–96.
- 58 A.J. Goodfellow: *Mater. Sci. Technol.*, 2018, vol. 34, pp. 1793–808.
- 59 R.W. Kozar, A. Suzuki, W.W. Milligan, J.J. Schirra, M.F. Savage, and T.M. Pollock: *Metall. Mater. Trans. A*, 2009, vol. 40, pp. 1588–603.
- 60 M.A. González, D.I. Martínez, A. Pérez, H. Guajardo, and A. Garza: *Mater. Charact.*, 2011, vol. 62, pp. 1116–23.
- 61 T. Connolley, P.A.S. Reed, and M.J. Starink: *Mater. Sci. Eng. A*, 2003, vol. 340, pp. 139–54.
- 62 X.Z. Qin, J.T. Guo, C. Yuan, C.L. Chen, and H.Q. Ye: *Metall. Mater. Trans. A*, 2007, vol.

- 38, pp. 3014–22.
- 63 R.L. Ashbrook and R.L. Dreshfield: .
- 64 B. Seiser, R. Drautz, and D.G. Pettifor: *Acta Mater.*, 2011, vol. 59, pp. 749–63.
- 65 V. Levitin: 2014.
- 66 J.R. Mihalisin and D.L. Pasquine: *Superalloys 1968*, 1968, pp. 134–70.
- 67 C. Booth-Morrison, Z. Mao, R.D. Noebe, and D.N. Seidman: *Appl. Phys. Lett.*, 2008, vol. 93, p. 33103.
- 68 S. Rosen and P.G. Sprang: *Adv. X-ray Anal.*, 1965, vol. 9, pp. 131–41.
- 69 M. Sundararaman, P. Mukhopadhyay, and S. Banerjee: *Metall. Trans. A*, 1992, vol. 23, pp. 2015–28.
- 70 D.A. Porter, K.E. Easterling, and M. Sherif: *Phase Transformations in Metals and Alloys, (Revised Reprint)*, CRC press, 2009.
- 71 A. Müller and W. Reimers: *Phys. status solidi*, 1996, vol. 156, pp. 47–58.
- 72 W. Hagel and H. Beattie: *Iron and Steel Institute Special Report*, London, 1964.
- 73 T. Grosdidier, A. Hazotte, and A. Simon: *Mater. Sci. Eng. A*, 1998, vol. 256, pp. 183–96.
- 74 M.P. Jackson and R.C. Reed: *Mater. Sci. Eng. A*, 1999, vol. 259, pp. 85–97.
- 75 G. Tellier: .
- 76 Y. Ji, Y. Lou, M. Qu, J.D. Rowatt, F. Zhang, T.W. Simpson, and L.-Q. Chen: *Metall. Mater. Trans. A*, 2016, vol. 47, pp. 3235–47.
- 77 R.A. Ricks, A.J. Porter, and R.C. Ecob: *Acta Metall.*, 1983, vol. 31, pp. 43–53.
- 78 A. Hazotte, T. Grosdidier, and S. Denis: *Scr. Mater.*, 1996, vol. 34, pp. 601–8.
- 79 Y.S. Yoo, D.Y. Yoon, Henry, and MF: *Met. Mater.*, 1995, vol. 1, pp. 47–61.

- 80 J. Tiley, G.B. Viswanathan, R. Srinivasan, R. Banerjee, D.M. Dimiduk, and H.L. Fraser: *Acta Mater.*, 2009, vol. 57, pp. 2538–49.
- 81 M. Doi: *Mater. Trans. JIM*, 1992, vol. 33, pp. 637–49.
- 82 M. Doi, T. Miyazaki, and T. Wakatsuki: *Mater. Sci. Eng.*, 1984, vol. 67, pp. 247–53.
- 83 M. Doi and T. Miyazaki: *Mater. Sci. Eng.*, 1986, vol. 78, pp. 87–94.
- 84 M. Doi, D. Miki, T. Moritani, and T. Kozakai: *Superalloys 2004*, 2004, pp. 109–14.
- 85 T. Miyazaki, H. Imamura, and T. Kozakai: *Mater. Sci. Eng.*, 1982, vol. 54, pp. 9–15.
- 86 Y.S. Yoo: *Scr. Mater.*, 2005, vol. 53, pp. 81–5.
- 87 X. Fan, Z. Guo, X. Wang, J. Yang, and J. Zou: *Mater. Charact.*, 2018, vol. 139, pp. 382–9.
- 88 M. Doi, T. Miyazaki, and T. Wakatsuki: *Mater. Sci. Eng.*, 1985, vol. 74, pp. 139–45.
- 89 C.L. Qiu and P. Andrews: *Mater. Charact.*, 2013, vol. 76, pp. 28–34.
- 90 R.D. Doherty: *Met. Sci.*, 1982, vol. 16, pp. 1–14.
- 91 R.R. Unocic, L. Kovarik, C. Shen, P.M. Sarosi, Y. Wang, J. Li, S. Ghosh, and M.J. Mills: *Superalloys*, 2008, vol. 8, p. 377.
- 92 M. Fahrmann and A. Suzuki: in *12th Symposium on Superalloys, Superalloys*, 2008, pp. 311–6.
- 93 Y.Q. Chen, T.J.A. Slater, E.A. Lewis, E.M. Francis, M.G. Burke, M. Preuss, and S.J. Haigh: *Ultramicroscopy*, 2014, vol. 144, pp. 1–8.
- 94 S.T. Wlodek, M. Kelly, and D. Alden: *Superalloys 1992*, 1992, pp. 467–76.
- 95 T. Osada, Y. Gu, N. Nagashima, Y. Yuan, T. Yokokawa, and H. Harada: *Acta Mater.*, 2013, vol. 61, pp. 1820–9.
- 96 D. Locq, P. Caron, S. Raujol, F. Pettinari-Sturmel, A. Coujou, and N. Clément:

- Superalloys 2004*, 2004, pp. 179–87.
- 97 R.J. Mitchell, M. Preuss, S. Tin, M.C. Hardy, S. Tin, and M.C. Hardy: *Mater. Sci. Eng. a-Structural Mater. Prop. Microstruct. Process.*, 2008, vol. 473, pp. 158–65.
- 98 P.M. Sarosi, B. Wang, J.P. Simmons, Y. Wang, and M.J. Mills: *Scr. Mater.*, 2007, vol. 57, pp. 767–70.
- 99 T.P. Gabb, J. Gayda, J. Telesman, and A. Garg: .
- 100 J. Mao, K.-M. Chang, W. Yang, K. Ray, S.P. Vaze, and D.U. Ferrer: *Metall. Mater. Trans. A*, 2001, vol. 32, pp. 2441–52.
- 101 A.M. Wusatowska-Sarnek, G. Ghosh, G.B. Olson, M.J. Blackburn, and M. Aindow: *J. Mater. Res.*, 2003, vol. 18, pp. 2653–63.
- 102 E.I. Galindo-Nava, L.D. Connor, and C.M.F. Rae: *Acta Mater.*, 2015, vol. 98, pp. 377–90.
- 103 R. Jiang, S. Everitt, M. Lewandowski, N. Gao, and P.A.S. Reed: *Int. J. Fatigue*, 2014, vol. 62, pp. 217–27.
- 104 C. Papadaki, W. Li, and A.M. Korsunsky: *Materials (Basel)*., 2018, vol. 11, p. 1528.
- 105 S.L. Semiatin, S.-L. Kim, F. Zhang, and J.S. Tiley: *Metall. Mater. Trans. A*, 2015, vol. 46, pp. 1715–30.
- 106 F. Masoumi, D. Shahriari, M. Jahazi, J. Cormier, and A. Devaux: *Sci. Rep.*, 2016, vol. 6, p. 28650.
- 107 D.U. Furrer and H.-J. Fecht: *Scr. Mater.*, 1999, vol. 40, pp. 1215–20.
- 108 A.R.P. Singh, S. Nag, S. Chattopadhyay, Y. Ren, J. Tiley, G.B. Viswanathan, H.L. Fraser, and R. Banerjee: *Acta Mater.*, 2013, vol. 61, pp. 280–93.
- 109 A.R.P. Singh, S. Nag, J.Y. Hwang, G.B. Viswanathan, J. Tiley, R. Srinivasan, H.L. Fraser,

- and R. Banerjee: *Mater. Charact.*, 2011, vol. 62, pp. 878–86.
- 110 A.J. Goodfellow, E.I. Galindo-Nava, K.A. Christofidou, N.G. Jones, T. Martin, P.A.J. Bagot, C.D. Boyer, M.C. Hardy, and H.J. Stone: *Metall. Mater. Trans. A*, 2018, vol. 49, pp. 718–28.
- 111 K.M. Delargy and G.D.W. Smith: *Metall. Trans. A*, 1983, vol. 14, pp. 1771–83.
- 112 P.A.J. Bagot, O.B.W. Silk, J.O. Douglas, S. Pedrazzini, D.J. Crudden, T.L. Martin, M.C. Hardy, M.P. Moody, and R.C. Reed: *Acta Mater.*, 2017, vol. 125, pp. 156–65.
- 113 Y.Q. Chen, E. Francis, J. Robson, M. Preuss, and S.J. Haigh: *Acta Mater.*, 2015, vol. 85, pp. 199–206.
- 114 T. Wojcik, M. Rath, and E. Kozeschnik: *Mater. Sci. Technol.*, 2018, vol. 34, pp. 1558–64.
- 115 A.J. Goodfellow, E.I. Galindo-Nava, K.A. Christofidou, N.G. Jones, C.D. Boyer, T.L. Martin, P.A.J. Bagot, M.C. Hardy, and H.J. Stone: *Acta Mater.*, 2018, vol. 153, pp. 290–302.
- 116 T. Gladman: *Mater. Sci. Technol.*, 1999, vol. 15, pp. 30–6.
- 117 M.R. Ahmadi, E. Povoden-Karadeniz, K.I. Öksüz, A. Falahati, and E. Kozeschnik: *Comput. Mater. Sci.*, 2014, vol. 91, pp. 173–86.
- 118 M.K. Miller and M.G. Burke: *Atom Probe Analysis of the Compositions of Gamma. Prime and Gamma. Double Prime Intermetallic Phases in Nickel-Based Superalloy 718*, Oak Ridge National Lab., TN (USA), 1990.
- 119 V. Gerold and H. Haberkorn: *Phys. status solidi*, 1966, vol. 16, pp. 675–84.
- 120 H.Y. Wu, Z.W. Huang, N. Zhou, J.G. Chen, P. Zhou, and L. Jiang: *Mater. Sci. Eng. a-Structural Mater. Prop. Microstruct. Process.*, 2019, vol. 739, pp. 473–9.
- 121 K. Wu, G.Q. Liu, B.F. Hu, Y.W. Zhang, Y. Tao, and J.T. Liu: *Rare Met. Mater. Eng.*,

- 2012, vol. 41, pp. 1267–72.
- 122 A.S.M.H. Volume: *ASM Int.*
- 123 G.E. Totten and D.S. MacKenzie: .
- 124 G. Kumari, C. Boehlert, S. Sankaran, and M. Sundararaman: *J. Mater. Eng. Perform.*, 2020, pp. 1–11.
- 125 H.E. Boyer: 2013.
- 126 Y. Xu, C. Yang, Q. Ran, P. Hu, X. Xiao, X. Cao, and G. Jia: *Mater. Des.*, 2013, vol. 47, pp. 218–26.
- 127 D. Shahriari, M.H. Sadeghi, and A. Akbarzadeh: *Mater. Manuf. Process.*, 2009, vol. 24, pp. 559–63.
- 128 I. Dempster, W.G. Forgings, and R. Wallis: *Heat Treat. Nonferrous Alloy.*, 2016, vol. 4, pp. 399–425.
- 129 Decker: *Jom*, 2006, vol. 58, pp. 32–6.
- 130 V. Garat, J. Deleume, J.M. Cloué, and E. Andrieu: *Superalloys*, 2005, vol. 718, pp. 559–69.
- 131 G.L. Erickson: *Superalloys 1996*, 1996, pp. 35–44.
- 132 A. Soula, Y. Renollet, D. Boivin, J.L. Pouchou, D. Locq, P. Caron, and Y. Brechet: *Superalloys 2008*, 2008, pp. 387–94.
- 133 H.D. Monte Carlo simulation of electron trajectory in solids, Casino version 3.2.0.1, Casino Copyright ©, D. Drouin, A. Réal Couture, D. Joly, N. Poirier-Demers: *Univ. Sherbrooke*, 2011.
- 134 B. Gault, M.P. Moody, J.M. Cairney, and S.P. Ringer: *Atom Probe Microscopy*, vol. 160,

- Springer Science & Business Media, 2012.
- 135 Microscopy Australia: MyScope Microscopy Training, <https://myscope.training/>,  
(accessed 20 April 2021).
- 136 K. Thompson, D. Lawrence, D.J. Larson, J.D. Olson, T.F. Kelly, and B. Gorman:  
*Ultramicroscopy*, 2007, vol. 107, pp. 131–9.
- 137 S.Y. Sree Harsha Lalam H. Harada, H.K.D.H. Bhadeshia: 1999.
- 138 S. Yoshitake, V. Narayan, H. Harada, H.K.D.H. Bhadeshia, and D.J.C. Mackay: *ISIJ Int.*,  
1998, vol. 38, pp. 495–502.
- 139 D.J.C. MacKay: *Cerjak HKDH Bhadeshia, Inst. Mater. London*.
- 140 D.C.L.B.-D.O.E. Montgomery: *Design and Analysis of Experiments*, John Wiley & Sons,  
2017.
- 141 G.E.P. Box, W.G. Hunter, and J.S. Hunter: *Statistics for Experimenters*, vol. 664, John  
Wiley and Sons New York, 1978.
- 142 J. Antony: *Design of Experiments for Engineers and Scientists*, Elsevier, 2014.
- 143 R.A.S. Fisher 1890-1962. TA - TT -: 1966.
- 144 S. N. Politis, P. Colombo, G. Colombo, and D. M. Rekkas: *Drug Dev. Ind. Pharm.*, 2017,  
vol. 43, pp. 889–901.
- 145 R.A. Fisher: in *Breakthroughs in statistics*, Springer, 1992, pp. 66–70.
- 146 F. Yates: *J. Am. Stat. Assoc.*, 1951, vol. 46, pp. 19–34.
- 147 A. Dean, D. Voss, and D. Draguljić: *Design and Analysis of Experiments*, vol. 1, Springer,  
1999.
- 148 M.J. Anderson and P.J. Whitcomb: *DOE Simplified: Practical Tools for Effective  
Experimentation*, CRC Press, 2016.

- 149 D.R. Cox and N. Reid: *The Theory of the Design of Experiments*, CRC Press, 2000.
- 150 J.P. Davim and P. Aveiro: *Design of Experiments in Production Engineering*, Springer, 2016.
- 151 P.D. Berger and R.E. Maurer: *CA Wadsworth Gr. Belmont*.
- 152 K. Dunn: *Exp. Improv. Hamilton, Ontario, Canada. Creat. Commons Attrib.*, 2019, vol. 4, pp. 325–404.
- 153 M.A. Xavior, A. Duchosal, and P. Jeyapandiarajan: *Mater. Today-Proceedings*, 2018, vol. 5, pp. 13301–8.
- 154 A.M. Khorasani, I. Gibson, M. Goldberg, and G. Littlefair: *Int. J. Adv. Manuf. Technol.*, 2018, vol. 94, pp. 3765–84.
- 155 P. Sadr, A. Kolandooz, and S.A. Eftekhari: *J. Nav. Archit. Mar. Eng.*, 2017, vol. 14, pp. 47–64.
- 156 N. Khanna: in *Design of Experiments in Production Engineering*, J.P. Davim, ed., Springer Int Publishing Ag, Cham, 2016, pp. 165–82.
- 157 N. Khanna and J.P. Davim: *Measurement*, 2015, vol. 61, pp. 280–90.
- 158 G. Tosun: *Int. J. Adv. Manuf. Technol.*, 2011, vol. 55, pp. 477–85.
- 159 A. Khorasani, I. Gibson, U.S. Awan, and A. Ghaderi: *Addit. Manuf.*, 2019, vol. 25, pp. 176–86.
- 160 S. Sathish, V. Anandakrishnan, V. Dillibabu, D. Muthukannan, and N. Balamuralikrishnan: in *Advances in Manufacturing Technology*, S.S. Hiremath, N.S. Shanmugam, and B.R.R. Bapu, eds., Springer-Verlag Berlin, Berlin, 2019, pp. 371–9.
- 161 C.A. Leon-Patino, J. Garcia-Guerra, and E.A. Aguilar-Reyes: *Wear*, 2019, vol. 426, pp.

- 330–40.
- 162 G. Taguchi, S. Konishi, and S. Konishi: *Taguchi Methods: Orthogonal Arrays and Linear Graphs. Tools for Quality Engineering*, American Supplier Institute Dearborn, MI, 1987.
- 163 G. Taguchi, S. Chowdhury, and S. Taguchi: 2000.
- 164 Minitab 18 Support - Taguchi designs.
- 165 G.E.P. Box and N.R. Draper: *Empirical Model-Building and Response Surfaces*, vol. 424, Wiley New York, 1987.
- 166 P.D. Berger, R.E. Maurer, and G.B. Celli: in *Experimental Design*, Springer, 2018, pp. 533–84.
- 167 G.E.P. Box and N.R. Draper: *Response Surfaces, Mixtures, and Ridge Analyses*, vol. 649, John Wiley & Sons, 2007.
- 168 R.H. Myers, D.C. Montgomery, and C.M. Anderson-Cook: *Response Surface Methodology: Process and Product Optimization Using Designed Experiments*, John Wiley & Sons, 2016.
- 169 Surface designs, central composite designs, and Box-Behnken designs,  
<https://support.minitab.com/en-us/minitab/18/help-and-how-to/modeling-statistics/doe/supporting-topics/response-surface-designs/response-surface-central-composite-and-box-behnken-designs/>.
- 170 ASTM International: in *Annual Book of ASTM Standards*, 2012, pp. 464–506.